

ABSTRACT

Title of Dissertation: INFLUENCE OF CRYOGENIC TEMPERATURE AND MICROSTRUCTURE ON FATIGUE FAILURE OF INDIUM SOLDER JOINT

Rui Wu Chang, Doctor of Philosophy, 2008

Dissertation directed by: Associate Professor F. Patrick McCluskey
Department of Mechanical Engineering

This thesis aims to develop a fundamental understanding of the underlying mechanisms that govern indium attach degradation in applications requiring repeated excursions and extended long time dwells at temperatures below -55°C . This work was prompted by original effort of developing low temperature SiGe BiCMOS modules for Martine and Lunar exploration.

Current exploration vehicles use a “warm electronic box (WEB)” to maintain the electronics in an earth-like temperature environment. This results in increasing system complexity and weight. Warm boxes also consume power and are not practical for the ~ 330 hour lunar night. Furthermore, intelligent nodes in a distributed system must operate in an ambient environment to monitor the health and performance of a space craft or rover, to sense the environment for scientific exploration and to act on the environment, such as to use a drill to obtain a soil sample for analysis.

Nevertheless, the reliability and life span of electronic devices systems without WEB can

be significantly degraded by thermal fatigue damage as a result of wide daily temperature swings during their space exploration, when cryogenic temperatures (below -55°C) can be encountered. Attachment layer, such as die attach, solder joint and substrate attach are most inclined to fatigue damage due to the global CTE mismatch between packaging materials and their material properties at extreme cold temperatures.

With the aim of enhancing the reliability of cryogenic electronic package, indium was selected as the attachment material due to its excellent wetting capability, greater ductility and high electrical conductivity, with respect to standard PbSn solders at cryogenic temperatures. However, information on the reliability of indium attach is sparse and only concerns isothermal fatigue conditions at room temperature. No investigation has been reported on its thermal fatigue ranging from cryogenic temperature to high homologous temperatures (above room temperature), or on its isothermal fatigue behavior at cryogenic temperatures, or of the effect of microstructure evolution, in terms of intermetallics, under isothermal fatigue conditions on joint lifetime. Current lack of these fundamental understanding inhibits the assessment of the reliability of indium attach.

In this thesis, an efficient and systematic assessment was conducted to evaluate the reliability of indium attach. Constitutive properties of indium solder joint at extended low temperature were measured and the Anand constitutive model was validated for an extended temperature range, -150°C to 140°C , including extreme cold temperature. This was used to assess thermal fatigue life of indium attach. The effect of intermetallics and surface finishes on the reliability of indium attach subjected to mechanical fatigue has

also been investigated. In addition, fatigue failure site, modes and mechanisms in indium attach at low temperature were identified and correlated with microstructure evolution. A fatigue model was also calibrated for indium attach at cryogenic temperatures.

INFLUENCE OF CRYOGENIC TEMPERATURE AND MICROSTRUCTURE ON
FATIGUE FAILURE OF INDIUM SOLDER JOINT

by

Rui Wu Chang

Dissertation submitted to the faculty of the Graduate School of the
University of Maryland, College Park in partial fulfillment
of the requirements for the degree of
Doctor of Philosophy
2008

Advisory Committee:

Dr. F Patrick McCluskey, Chair and Advisor
Dr. Donald Barker
Dr. Isabel K. Lloyd
Dr. Michael Pecht
Dr. Peter Sandborn

©Copyright by
RUIWUCHANG
2008

DEDICATION

To my husband, parents and advisor

ACKNOWLEDGEMENT

First and foremost I would like to thank my advisor, Dr. Patrick McCluskey. Without his able support, advice and encouragement this research might have not been accomplished. I deeply appreciate his efforts to take time off his busy schedule to set me on the right path. I would also like to thank my other committee members, Dr. Donald Barker, Dr. Isabel Lloyd, Dr. Michael Pecht and Dr. Peter Sandborn for evaluating my work and also providing invaluable suggestions in refining the work.

I would like to thank Dr. Wayne Johnson of Auburn University very much for lively discussions and the invaluable suggestions in my work, also his grateful assistance in sample preparation and experimentation. In addition, special thank to Dr. John Cressler of Georgia Tech very much for his grateful technical assistance.

I would also like to thank NASA for supporting this work under a grant from the NASA ETDP program: Radiation Hardened Electronics for Space Environments (RHESE) Contract # NNL06AA29C, and especially Mike Watson for his technical and financial assistance.

I would also like to thank CALCE labs for their support of using equipments and daily interaction, particularly Bahnu, Anshul and Amed.

Special thanks to all my friends and colleagues, Pedro, Peter, Tim, Rupal, Leah, Adam, Lei, Jie, Shunfeng, Hongbo, Yuxun, Weiqiang, Yilin, Shenglan, Jake, Yuliang, Yan, Bo, Hui, Jian, Yan, Feng etc. etc. for all their help and support during my stay here.

Most of all I specially wish to thank my husband, Raymond, and my parents for supporting me all through these years and also giving me able support and comfort when I needed them most.

Table of Contents

DEDICATION	II
ACKNOWLEDGEMENT	III
TABLE OF CONTENTS	V
LIST OF FIGURES	VIII
CHAPTER 1 INTRODUCTION	1
1.1 SiGe Cryogenic Electronics	1
1.2 Use of Indium Attach in Cold Temperature Electronic Package	4
1.3 Problem Statement / Motivation	6
1.4 Scope of This Thesis	7
CHAPTER 2 LITERATURE REVIEW	10
2.1 Critical Factors in Solder Connection Fatigue	11
2.2 Constitutive Properties of Indium	15
2.3 Effect of Intermetallic Compound on Solder Joint Strength	25
2.3.1 Features of Au-In Intermetallics	27
2.3.2 Effect of Bonding Process on Intermetallic Formation	29
2.4 Differences in Deformation of Bulk Specimen and Solder Joint	30
2.5 Fatigue Analysis of Indium Solder Joint	31
2.5.1 Temperature Cycling on Solder Joint Fatigue	31
2.5.2 Mechanical Fatigue Failure	33
2.6 Review of Existing Fatigue Model	36
2.6.1 Strain Range-Based Model	36
2.6.2 Total Energy Criterion-Based Models	38
2.6.3 Energy Partitioning Fatigue Model (SEP)	39
CHAPTER 3 MATERIAL CHARACTERIZATION OF INDIUM TO EXTENDED COLD TEMPERATURES	41
3.1 Constitutive Properties of Indium	41
3.1.1 Motivation to Use Constitutive Anand Model	41
3.1.2 Parameter Determination	44
3.2 Measurement of Constitutive Properties at Low Temperatures	45
3.2.1 Sample Preparation	46
3.2.2 Test Equipment – RSAIII	48
3.2.3 Experimental Procedure – Determination of Strain Rate	50
3.3 Results & Discussion	52
3.3.1 Experimental Results	52
3.3.1.1 Validity of the Experimental Results	56
3.3.1.2 Effect of Temperature on Strain Rate	57
3.3.1.3 Initial Sample Length vs. Strain/Strain Rate	58
3.3.1.4 Initial Loading vs. Strain/Strain Rate	60
3.3.2 Validation of Anand Model	62

3.3.3	Correlation of Shear and Compression Loading.....	65
3.4	Conclusion	67
CHAPTER 4 THERMAL FATIGUE OF INDIUM SOLDER JOINT		69
4.1	Thermal Fatigue of Indium Solder Joint.....	69
4.2	Effect of Thermal Cycling/Shock Test on Fatigue Life Prediction	71
4.2.1	Thermal Cycling vs. Thermal Shock Test	72
4.2.2	Thermal Shock Test for Indium Solder Joint.....	73
4.3	Thermal Shock Test	74
4.3.1	Sample Preparation	75
4.4	Test Setup and Experimental Procedure.....	76
4.4.1	Thermal Shock Test Results	76
4.5	Fatigue Failure Analysis	77
4.5.1	Fatigue Cracks in Si/AlSi Packages.....	78
4.5.2	Interfacial Fracture & Fatigue Cracks in Si ₃ N ₄ /AlSi Packages	79
4.5.3	Other Failure Sites & Causes.....	81
4.6	Thermomechanical Transient Analysis.....	82
4.7	Thermal Transient Analysis.....	83
4.8	Nonlinear Structural Analysis.....	84
4.8.1	Development of FEM Structural Model	84
4.8.2	Sensitivity Study	90
4.9	Discussion and Conclusion.....	92
4.10	Fatigue Life Prediction	93
CHAPTER 5 ISOTHERMAL FATIGUE OF INDIUM SOLDER JOINT AT EXTENDED COLD TEMPERATURE		99
5.1	Evaluation of Solder Joint Fatigue at Subzero Temperatures.....	99
5.2	Identification of Intermetallic Phases @ In-Au Interfaces	101
5.3	Intermetallics Growth under Thermal Aging @ 125°C.....	103
5.4	Fatigue Bending Test at Cold Temperature	107
5.4.1	Design of Experiment (DOE)	107
5.4.2	Specimen Preparation	108
5.4.2.1	Sample Details	108
5.4.2.2	Sample Soldering.....	109
5.4.2.3	Sample Quality Examination	111
5.4.3	Test setup and Experimental Procedure.....	111
5.4.4	Experimental Results	113
5.4.4.1	Fatigue Crack Growth Measurement.....	113
5.4.4.2	Fatigue Life Data	116
5.4.4.3	Statistical Analysis – Two Sample T-Test.....	120
5.5	Fatigue Failure Analysis	126
5.5.1	Fatigue Failure Site	127
5.5.2	Fracture Modes & Root Cause.....	129
5.5.3	Effect of Intermetallics	132
5.5.4	Effect of Thermal Aging.....	137
5.5.5	Effect of Fatigue Temperature	143
5.5.6	Effect of Loading Frequency	144

5.6	Discussion and Summary.....	147
5.7	Finite Element Modeling of Bending Fatigue	149
5.8	Fatigue Life Prediction	153
CHAPTER 6 SUMMARY, CONTRIBUTIONS AND SUGGESTIONS FOR FUTURE WORK		159
6.1	Summary	159
6.2	Major Contributions.....	161
6.3	Suggestions for Future Work	163
APPENDIX A: ANSYS APDL CODE OF THERMOMECHANICAL ANALYSIS		164
APPENDIX B: ANSYS APDL CODE OF 3D NONLINEAR BENDING FATIGUE – GLOBAL MODELING		168
REFERENCES		171

List of Figures

Figure 1 WEB on current mars rover (courtesy: NASA JPL)	2
Figure 2 (a) Die attach to substrate test vehicle [76]; (b) Schematics of packaged structure.	3
Figure 3. (a) Elastic modulus, (b) thermal conductivity and (c) CTE of indium as a function of temperature.....	17
Figure 4 Schematic of strain vs. time curve for a creep test [17]	18
Figure 5. Creep rate of indium as a function of applied stress at different stress levels and different temperatures [8]	19
Figure 6. Au-In equilibrium phase diagram [39].....	27
Figure 7. (a) Au-In diffusion couple annealed 144h at 150°C; (b) kinetics of Au-In reaction at 100,125 and 150°C [40].	28
Figure 8. Creep behavior of indium bulk specimen and solder joint [53].	30
Figure 9 Normalized stress-strain rate in indium at different temperature.....	42
Figure 10 Measured length of specimen at three separate directions.	47
Figure 11 Schematic of indium specimen under the testing fixture in RSAIII	48
Figure 12. Base system of RSAIII [88]	49
Figure 13. Oven chambers with PRTs [88]	50
Figure 14. Test matrix of constitutive properties characterization	52
Figure 15 Test sets of time dependent strain at T=-50°C F=500gf.....	53
Figure 16 Experimental data post processing – statistical normal distribution	54
Figure 17. Time dependent strain under loading force 500 gf at -50°C	55
Figure 18. Strain rate from the present experiment and other publications.....	56
Figure 19 Time-dependent strain under loading force 500 gf at 0°C	57
Figure 20 Strain vs. time under loading force 1200gf at -140°C.....	58
Figure 21 Strains at various test sets at the starting point of steady state.....	59
Figure 22. Length differences and strain difference at starting point of steady state	60
Figure 23. Length differences and strain rate differences at steady state	60
Figure 24. Preloaded force and relative strain difference at starting point of steady state	61
Figure 25. Preloaded force and relative strain rate at steady state.....	61
Figure 26 Time-temperature dependent material properties of indium.....	62
Figure 27 Schematic of sample under uniaxial compression loading.....	66
Figure 28 Schematic of sample under simple shear loading.....	66
Figure 29 Temperature profile on the surface of the Moon.....	70
Figure 30 Block diagram of the work in fatigue life prediction.	70
Figure 31. Scale Factor form Weibull curves of TS and TC tests [42]	71
Figure 32. Hysteresis loops of indium solder joint at its edge corner under different thermal loadings.....	72
Figure 33. Simulation of stress relaxation of indium attachment at 398K.	74
Figure 34. Simulation of stress reduction at dwell stage in thermal shock test.....	74
Figure 35. Samples under thermal shock test with different dimensions	75
Figure 36. Schematic of metallization patterns in the package	76
Figure 37. CSAM picture of Si/AlSi package #1 (0.8 inch by 0.8 inch).....	79

Figure 38. Solder joint fatigue failure after thermal shock test.	79
Figure 39. (a) Brittle fracture through intermetallic layer at joint interface with 50 cycles in SiN/AlSi package; (b) fatigue cracking through solder joint with 150 cycles in both Si/AlSi and SiN/AlSi package (0.8 by 0.8 inch).....	80
Figure 41. EDS analysis of Si ₃ N ₄ /AlSi package (Gold: Purple; Indium: blue;).....	81
Figure 42. (a) Ni/AlSi delamination crack; (b) Vertical crack in AlSi substrate.....	82
Figure 43. Temperature profile of thermal shock test.....	83
Figure 44 Detailed FEM model in ANSYS	85
Figure 45 Critical elements used to obtain averaged inelastic strain.....	86
Figure 46 Contour plot of VonMises inelastic strain after 4 cycles of thermal shocking.	88
Figure 47 Cyclic VonMises inelastic strain of 3 critical elements at the edge corner of the solder joint.	89
Figure 48 Cyclic stress/strain curves in solder joint after thermal shocking.	89
Figure 49 Stress-strain hysteresis loops at outer corner in solder joint after thermal shocking.....	90
Figure 50. Schematic of simplified package model.....	90
Figure 51 Max. inelastic strain at the outer corner of the package in indium after thermal loading.....	91
Figure 52 Inelastic strain as the function of indium solder thickness and package sizes: strain is more sensitive to solder thickness.....	92
Figure 53. Curve fitting for Coffin-Manson empirical model.....	94
Figure 54. Schematic of die attach and substrate.....	95
Figure 55. Contour plot of VonMises inelastic strain distribution in the whole die attach type package.....	96
Figure 56. Schematic of flip chip solder bump and substrate.....	96
Figure 57. Contour plot of VonMises inelastic strain distribution in the whole flip-chip type package.....	97
Figure 58. FEM model of substrate to package.....	97
Figure 59. Predicted fatigue life of new designed electronic module based on the Coffin-Manson fatigue model.....	98
Figure 60 Intermetallics at indium solder joint interface.....	103
Figure 61 Voids enlargement after thermal aging: (a) before aging; (b) after aging.....	104
Figure 62 Measurement of IMC thickness.....	105
Figure 63 Mean values of measured IMC thickness by fitting to normal distribution. ...	106
Figure 64 IMC growth with aging time with respect to different initial Au metallization thickness.....	106
Figure 65 Flow chart of low cycle fatigue test at low temperatures.....	108
Figure 66 schematic of bonded samples for isothermal fatigue test at cold temperatures.	109
Figure 67 Measured temperature profile under reflow soldering.....	110
Figure 68 Three point bending tool with sample loaded referred to RS&AIII manual.	112
Figure 69 Schematic of positive sine wave of applied strain.....	113
Figure 70 Fatigue crack at 1600 cycles in sample #20 with Au=3μm @ -150°C.	114
Figure 71 Fatigue crack at 2000 cycles in sample #20 with Au=3μm @ -150°C.	114
Figure 72 Typical crack growth measurement and determination.....	115
Figure 73 Schematic of failure criteria in specimen.....	117

Figure 74 Corresponding peak load drop during fatigue test when crack area is 50%.	117
Figure 75 2P Weibull plot of fatigue data under bending fatigue with different failure modes.	119
Figure 76 Fatigue crack in specimens under 3 point bending test (sample#9 @Au=1 μ m, 1 Hz).	128
Figure 77 Fatigue crack through intermetallics layer in sample #9 with Au=1 μ m, 0.3 Hz.	129
Figure 78 Brittle fracture through Intermetallic layer with different fracture modes from component side edge to center (sample#13 with Au=1 μ m).	131
Figure 79 Fracture within IMC layer and dimple morphology of fracture surface subject to cyclic bending when the thickness of Intermetallic is between 5 and 12 μ m (Sample#10 with Au=1 μ m).	132
Figure 80 The evolution of dimple morphology.	132
Figure 81 Relationships of fatigue life with intermetallics content of solder joint.	135
Figure 82 Fracture surface of samples with 1 μ m Au coating and about 12 μ m thick Intermetallic: (a) dimple-like surface mixed area; (b) enlarged Intermetallic delaminating area.	137
Figure 83 Fracture surface of samples with 1 μ m Au coating and about 12 μ m thick Intermetallic:	137
Figure 84 Fatigue life of solder joint with various Intermetallic thicknesses before and after aging.	139
Figure 85 Fracture surface of samples with 1 μ m thick Au metallization.	141
Figure 86 Fracture surface of samples with 3 μ m thick Au metallization.	142
Figure 87 Thermal aging effect on crack growth rate according to different Au coating thickness.	143
Figure 88 Temperature effect on fatigue life with different amount of Intermetallic.	144
Figure 89 Loading profile in bending fatigue test with different frequencies.	145
Figure 90 Effect of loading frequency on fatigue life of indium solder joint @-150 $^{\circ}$ C (Au=0.5 μ m).	145
Figure 91 Quarter symmetry model for mechanical fatigue at -150 $^{\circ}$ C (a) overview; (b) solder joint layer.	150
Figure 92 Volume averaged elements on the top layer.	151
Figure 93 Hysteresis loop of indium solder joint after 10 loading cycle at the most outer edge of component (Au=0.5 μ m).	152
Figure 94 Averaged strain energy density at the critical site in solder joint (Au=0.5 μ m).	152
Figure 95 Crack initiation correlation.	154
Figure 96 Crack growth rate correlation.	155
Figure 97 Fatigue life deviations with different Au-In intermetallic thicknesses.	156

List of Tables

Table 1. Exponent constant of indium at different temperatures.....	19
Table. 2 Creep Mechanisms in pure metals and solder alloys.....	20
Table 3. Physical and mechanical properties of AuIn, NiSn and CuSn intermetallics....	29
Table. 4 Summary of experimental setups.....	46
Table. 5 Experimental results at different temperatures and loading forces.....	55
Table. 6 Material parameters with Anand model of Indium for steady state plastic flow	63
Table. 7 Material parameters in constitutive model under different loading state.	67
Table. 8 Left censored interval fatigue data from thermal shock test.....	76
Table. 9 Characteristic life to failure after thermal shock test.....	77
Table. 10 Elastic properties of silicon.....	86
Table. 11 Elastic properties of silicon nitride [12]	86
Table. 12 Elastic properties of AlSi housing [13].....	87
Table. 13 Material properties of indium	87
Table. 14 Measured crack growth data under different loading conditions.	116
Table. 15 Measured fatigue life initiation and total life.....	118
Table. 16 Values of Weibull parameters.....	119
Table. 17 Hypothesis t-test results in terms of different intermetallic thicknesses.	135
Table. 18 Hypothesis t-test results before and after thermal aging.....	139
Table. 19 Fatigue life increase as frequency rises from 0.3 Hz to 1Hz.	146
Table. 20 Fatigue failure sites and modes under different ambient temperature.....	149
Table. 21 Isothermal fatigue conditions for crack growth study.	153
Table. 22 Crack growth correlation constants.	155

Chapter 1 Introduction

1.1 SiGe Cryogenic Electronics

Cryogenic electronics are widely applied in a variety of cutting-edge applications, ranging from high-sensitivity cooled sensors/detectors in space exploration to cryogenically cooled computing systems [0]. One especially critical application of cryogenic electronics is in space exploration, where extended cold temperatures, far below military-use limits (-55°C), require special features in electronic systems to enable them to operate reliably. Moreover, space exploration not only provides a number of examples of extremely cold environments, but also involves wide temperature-cycling extremes. For example, in the equatorial region of the moon, the temperature ranges from -180°C (night) to 120°C (day). And the temperature on Mars ranges from -120°C to $+20^{\circ}\text{C}$. This requires space electronics to function at both extremely low temperatures and to survive under wide temperature swings.

The current mars rover uses “warm electronic boxes (WEB)” to maintain the electronics in an earth-like temperature environment as shown in Figure 1. However, this results in increasing system complexity and weight. Warm box also consume power and are not practical for the ~ 330 hour lunar night. Furthermore, intelligent nodes in a distributed system must operate in an ambient environment to monitor the health and performance of a space craft or rover, to sense the environment for scientific exploration and to act on the environment, such as to use a drill to obtain a soil sample for analysis.

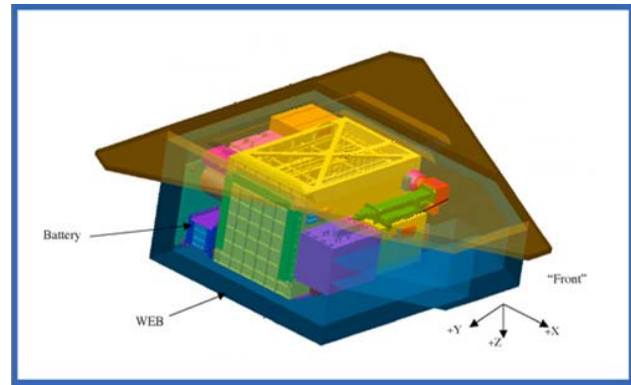
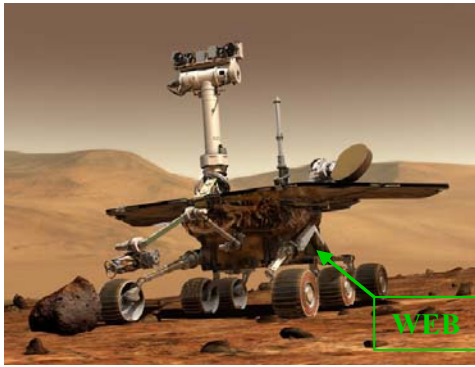


Figure 1 WEB on current mars rover (courtesy: NASA JPL).

A module based on the SiGe bipolar-junction transistor and complementary metal–oxide–semiconductor technology (BiCMOS), was demonstrated to work below -230°C . The excellent performance advantages of this integrated SiGe BiCMOS over the Si BiCMOS's at extreme low temperature as well as room temperature have been demonstrated [0]. These include higher current gain at lower temperatures than room temperature and higher speeds for unloaded ECL circuits in SiGe BiCMOS than for Si BiCMOS at low temperatures as well as at room temperature.

To leverage this device technology into space electronics and systems, packaging technology has been developed. A system-in-package approach was selected to minimize size and weight and to reduce the number of interconnection interfaces. The major concern in the product development is that the whole electronic system will be subjected to the huge temperature changes, almost 300°C temperature change on the Moon's surface or 140°C on Mars, and extended cold temperatures during lunar or Martian nights over the duration of a mission to Moon or Mars.

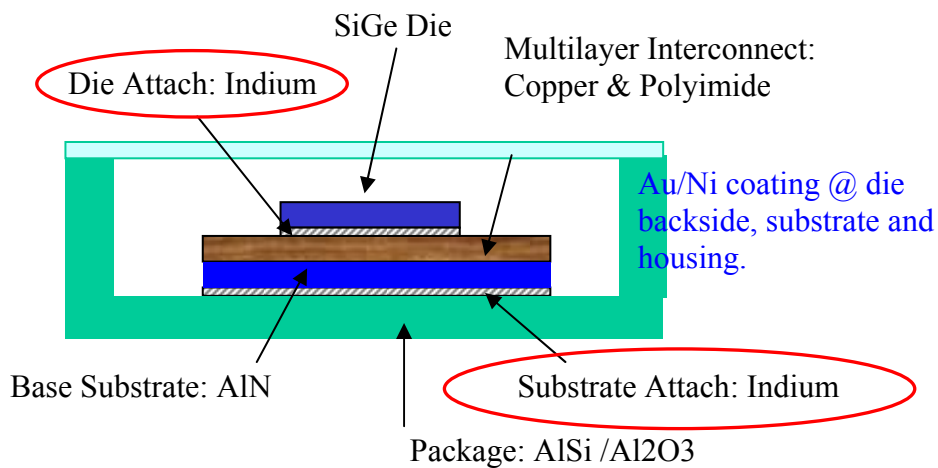
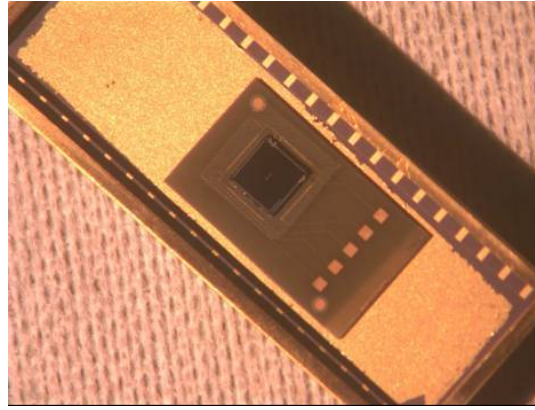


Figure 2 (a) Die attach to substrate test vehicle [76]; (b) Schematics of packaged structure.

According to these extreme temperature environment operational conditions, specific materials have been chosen for the package taking into account their low temperature performance and relative CTE as shown in the packaging structure in Figure 2. For example, the aluminum nitride was used as the base substrate because it has an excellent CTE match with Si, good thermal conductivity, and higher fracture toughness at cold temperatures compared to the most commonly used ceramic substrate, alumina. Also, AlSi was used for the housing material to take advantage of its adjustable CTE (low mismatch to substrate), high thermal conductivity at cold temperatures, high specific modulus, and light weight. Pure indium was used as the die attach, flip chip solder bumps

and substrate attachments joining the different packaging materials. The advantages of using indium as the attachment material in cold temperature packaging applications will be discussed in more detail in the next section.

Moreover, previous work indicates that the durability and reliability of electronic systems can be significantly degraded by thermal fatigue damage to the die attach and solder joint at the chip on substrate (1st level) or substrate to board (2nd level). This damage is caused by their constitutive properties and CTE mismatch between packaging materials [1,2,3,4,5]. Another source of concern is the isothermal mechanical fatigue (eg. Shock, vibration) at extreme temperatures. All of these concerns direct our research work focusing on the attachment layer's reliability.

1.2 Use of Indium Attach in Cold Temperature Electronic Package

The operational reliability of the solder joint materials that are currently used in space electronics within a “warm electronics box” (WEB) is at risk when the WEB is removed due to the extreme temperature environment to which they are exposed. This is the driving force in exploring other materials that are suitable for extremely cold temperatures.

Materials used for attachment are commonly grouped into four categories: “soft” solders, “hard” solders, organic adhesives, and inorganic adhesives. Because the whole electronic package will be exposed to low temperatures, most information found during this investigation relates to the soft solders.

Soft solders, including virtually all low-melting lead, tin- and indium-based solders, have low strength and high ductility. Compared to the hard solders, these solders have the advantage of lower assembly temperatures during die attachment. During temperature or power cycling, these solders transmit very little stress to the die. Therefore, those solders can be used to join much larger die and are also relatively inexpensive. Of these solders, behavior differs greatly among the alloys. Some general trends may be extracted: Pb-rich PbSn alloys retain a fair fraction of their ductility down to cryogenic temperatures; however, as Sn content increases, particularly for alloys of 40% percent Sn, PbSn alloys become brittle below -50°C to -150°C [2]. Thus there is a serious question whether Sn-rich PbSn solders are advisable for Moon explorations.

Hard solders are usually gold-based eutectics such as Au-3%Si, Au-12%Ge and Au-20%Sn. Those materials have high strength and do not undergo stress relaxation at ordinary electronics temperatures. Solders do not quickly degrade from fatigue damage, but as a consequence they may transmit more stress to the semiconductor die, provoking cracks in all but the smallest die ($<5\text{mm}$ by 5mm). The high temperatures required for die attachment would also aggravate stress when assemblies are cooled to low temperatures.

The toxic effects of Pb have caused it to be reduced or eliminated in many applications. In the European Union, the use of certain hazardous substances, including lead, in electrical and electronic equipment has been banned. Although the use of Pb in the electronics industry accounts for less than 7% of the total Pb consumption in the U.S., pressure is mounting to remove it from electronic manufacturing processes. Because of these concerns, efforts have been ongoing to find acceptable Pb-free solders.

Indium was selected in the present work as the attachment material with the aim to enhance the overall reliability of the electronic module (Figure 2). The advantage of indium for cryogenic joining has been acknowledged for many years [2,3,5,6,7,10,12,13]. Its greater ductility and excellent conductivity have been demonstrated with respect to standard SnPb solders at cryogenic temperatures. Some advantages of indium are that: 1) It is the softest malleable metal that is stable in air (low melting temperature $T = 156^{\circ}\text{C}$). 2) It has excellent wetting characteristics, enabling reliable joining of glass, ceramics or metals. 3) It has higher fatigue resistance as a result of its greater ductility at low temperatures. 4) It exhibits reduced intermetallic formation with gold compared to SnPb solders with gold. 5) It has superior electrical conductivity at cryogenic temperatures. 6) It is lead-free.

1.3 Problem Statement / Motivation

Indium shows promise as an attachment material due to its superior mechanical, electrical and thermal properties at cold temperatures, as discussed in the previous section. However, there is a lack of studies on indium's low temperature deformation behavior and on the reliability of indium attach under thermal fatigue with large temperature swings down to extreme low temperatures and isothermal fatigue conditions at extended cold temperatures. There is also a lack of understanding of the microstructure evolution effect on its reliability, which prevents the prediction of its fatigue life. This work is therefore intended to be a complete assessment of the reliability of indium attach on the chip- to the substrate/board-level. The study is basically divided into the following aspects.

Extensive work on the deformation properties of indium has been conducted over the past 20 years [2,3,4,5,6,7,8,9,10,11,12,13]. A review of the mechanical properties of indium-based alloys at room temperature is given by Kirschmann [2]. The tensile properties of pure indium at -269°C to 23°C are reported by Reed et al. [9]. However, the constitutive properties of indium at low temperatures (-150°C to 0°C) are not complete, especially its viscoplastic properties; these properties not only form the basis of the deformation behavior but are also central in cold-temperature fatigue-life modeling.

Moreover, fatigue data of indium attach are only available under isothermal conditions at room temperature [12,13]. There is a significant lack of reliability information on cold temperature fatigue since the fatigue temperature is far below the room temperature.

Furthermore, from the microscopic point-of-view, microstructure evolution and intermetallics play a more critical role in the overall fatigue life of the electronic package at extended cold temperatures. The intrinsic strengthening mechanisms and inherent brittleness of intermetallics, however, still have not been fully studied [11]. Furthermore, the failure sites, modes and correlation of the lifetime and reliability with the amount of intermetallics in solder joints have not been adequately addressed. The lack of all of this fundamental understanding limits the prediction or interpretation of the behavior of indium solder joints at extended cold temperatures. This thesis, therefore, addresses these problems.

1.4 Scope of This Thesis

In this work, tests, failure analysis, microstructure characterization, and modeling have been conducted to permit the evaluation of the reliability of indium solder used in SiGe

electronic packages designed for operation on the surface of the Moon or Mars. The effects of extended dwells at cold temperatures, wide temperature swings, and microstructure on the deformation behavior of indium were studied particularly.

The viscoplastic properties of indium at extended cold temperatures have been measured and implemented in an analytical constitutive model to make the study of its constitutive properties complete. Anand's analytical constitutive model was validated for indium down to -150°C . The fatigue behavior of indium solder joint was studied, including in a liquid nitrogen environment. A reliability assessment of indium solder joints was conducted on the basis of accelerated thermal shock tests from -195°C to 125°C and isothermal fatigue tests at -150°C and -55°C . The fatigue damage processes at cold temperatures, namely, cyclic deformation, fatigue crack initiation, and fatigue crack growth, and fatigue lifetimes were studied for first time. Fatigue behavior is related to cyclic strain amplitude, the number of fatigue cycles, frequency, temperature and microstructure.

To summarize, this study includes the following:

- 1) The first measurement of the rate-temperature dependent constitutive properties of indium at extended cold temperatures (-150°C to 0°C), including validation of the viscoplastic Anand model to describe indium's deformation behavior over temperature range from -150°C to 140°C .
- 2) Thermal fatigue and mechanical fatigue assessment of indium attach solder joint and fatigue life prediction by incorporating the measured viscoplastic properties of indium into a FEM model.

- 3) The first determination of the effect on solder joint deformation and fatigue behavior at extended low temperatures (-150°C and -55°C) of a) microstructure evolution, in terms of intermetallics growth, and b) loading conditions, including the fatigue damage processes at cold temperature, namely, cyclic deformation, fatigue crack initiation, and fatigue crack growth. The first identification of deformation failure mechanisms in solder joints at extended cold temperatures (-150°C to -55°C).
- 4) Correlation of the microstructure evolution and intermetallics at solder joint bonding interfaces with macroscopic fatigue behavior at extended cold temperatures.

Chapter 2 Literature Review

This chapter presents a literature review of previous research related to thermal fatigue and mechanical fatigue of indium attachment. The articles are divided into six categories that provide the basic understanding needed to develop models to evaluate the thermal fatigue and mechanical fatigue life of indium attachment, especially for the extreme environment of space exploration. Once predictive capability is established, it can be used as tool to rapidly evaluate new product designs and to correlate accelerated test conditions to real field use-conditions.

Generally, the durability of the attachment to withstand temperature and mechanical fatigue cycling is a function of many parameters, such as the package design (size of the die, thickness of the solder joint, the solder joint microstructure and mechanical properties, etc.), the fabrication process (method of soldering, metallization composition, soldering temperature, soldering atmosphere, etc.) and the cycling conditions (power input, junction temperature, cycling time, cooling methods, etc.). It is necessary to explore the critical parameters that most significantly influence attachment fatigue, which are summarized in the first category of the literature review.

The second category summarizes investigations into the constitutive properties of indium and the constitutive equations describing its deformation behavior during temperature cycling. The third explores the effect of constrained deformation on the observed behavior of indium solder joint vs. indium bulk specimen. The articles in the fourth category discuss the effect of microstructure differences and precipitation strengthening

from intermetallics of indium solder joint. The fifth category addresses the existing reliability information on indium solder joints, and the sixth focuses on prior fatigue failure models.

2.1 Critical Factors in Solder Connection Fatigue

Solder connection (die attach, solder bumps, etc.) provides both mechanical and electrical connection between and within the many levels of an electronic package. Notable examples are found in flip-chip and ball grid array packages where solder bumps or balls serve as the necessary leadless interconnections between two separate electronic components. The solder alloys used to make these interconnects are often subject to cyclic loading resulting from repeated mechanical actions or thermal cycling, leading to fatigue failures of the solder joint and the interconnect.

Thermal cycling refers to situations where the environment surrounding the electronic package undergoes cyclic thermal excursions. Generally, the cycle consists of a dwell at a high temperature, a ramp to a low temperature, a dwell at the low temperature, and a ramp to the high temperature, after which the cycle is repeated. Two common thermal cycling examples are the heating and cooling that occurs during a typical day during the morning and evening hours, and the heating and cooling of an automobile engine compartment upon a person's commute to and from his/her workplace. Electronic packages experience an isothermal temperature as they come to equilibrium with the environment during the high and low dwells. The CTE mismatch between the die or package and the substrate or PWB causes the solder joints to deform and fatigue over many cycles.

Due to the extremes of planetary climate, the solder joint in space electronic packages must withstand much larger thermal fatigue loading and extended cold temperatures, and therefore the fatigue reliability of the solder joint becomes a critical issue in determining the lifetime of a functional device. Since the fatigue of a solder alloy in an electronic package may involve multiple processes, such as atomic diffusion, dislocation motion, grain boundary sliding, and propagation of fatigue cracks, the life prediction for the solder joint, which also affects the reliability of the electronic device, remains a serious challenge.

Extensive studies have addressed PbSn solder interconnects and their fatigue reliability [1–3], including fatigue testing of real joints [4–17], constitutive modeling of stresses and deformation in the joint [18–20], and bulk property measurements on solder alloys at normal temperature range ($>-40^{\circ}\text{C}$) [21–25]. The literature on thermal cycling of electronic components containing SnPb eutectic solder is abundant, as accelerated thermal cycling (ATC) testing is one of the most common ways to test solder joint reliability. The low-cycle thermal-fatigue failure of SnPb eutectic solder joints due to the CTE mismatch is fairly well understood. As a result, these experimental and modeling efforts together have resulted in considerable success in ensuring adequate fatigue reliability of PbSn solder interconnects in many electronic packages. These studies are helpful for understanding the failure mechanisms and the critical factors that influence the fatigue life of solder joints in cryogenic environments.

Because indium solder joints are to be used in space electronics for moon exploration instead of PbSn solders, the differences in their fatigue behavior must be examined and

understood. Some of the differences are to be expected because of the inherent differences between indium solder joint and PbSn solder alloys. For example, PbSn solders, and even eutectic PbSn solders, melt at higher melting temperatures than pure indium [0]. At a given temperature, these PbSn alloys are considerably stiffer than indium. Thus, under the same strain, they will be subject to higher stresses and, therefore, prone to stress-induced failures.

Overall, it is commonly accepted that under thermal fatigue conditions the following parameters are critical in determining the fatigue life of die attach or solder joint: 1) the temperature range (ΔT) during temperature cycling, 2) the two temperature extremes, 3) the temperature loading time (ramp rate, dwell time), and 4) the thickness of the die attach. The critical effects of both ΔT and the thickness of the die attach are logical since they are both related to the level of cyclic stress/strain due to a CTE mismatch between different packaging materials, the direct cause for die-attach fatigue failure. Cracks in die attach usually initiate from the edges and propagate toward the center since cyclic stress/strain usually reaches its maximum at the edges first. This is true for indium attach as well.

However, for our present study, the very harsh operational environment, including extended low temperatures, subjects the electronic modules to greater levels of thermal and mechanical fatigue than normal commercial electronics or even electronics for military use, and making the assessment of its reliability necessary.

The literature available on mechanical fatigue of solder joints at extreme cold temperatures is limited [12], partly due to both the niche application area and the

complexity of the problem. With large-area array components, it is important to understand how the packaging material's behavior, surface finishes, low temperatures and loading conditions (strain amplitude, frequency, etc.) affect the solder joint fatigue life [10, 13]. This involves experimentally applying fatigue loading and observing failure of solder joints. Load transfer models and analytical or numerical models must be able to reproduce the essential cold temperature characteristics and incorporate solder joint behavior. The need to understand mechanically induced solder joint fatigue failure is especially important in extreme temperature environments [14].

Moreover, in contrast to at high temperature, diffusion controlled process does not make any appreciable contribution to the mechanism of fatigue fracture at extreme low temperatures. The fatigue failure site, mode and corresponding mechanisms of indium solder joints at cryogenic temperatures might be different from those at high temperatures, but they have rarely been reported.

Intermetallics at the bonding surface of the solder joint are also a critical factor affecting the fatigue life of solder joints under mechanical loading in cryogenic environments. Intermetallics often have high melting temperatures, due partly to the strong bonding between unlike atoms. The presence of these strong bonds also results in high creep resistance. Thus, intermetallics at the bonding interfaces can strengthen the solder joint [0]. However, intermetallics can also become brittle and excessive, especially at the bonding interfaces, which can result in bond failure, particularly at cryogenic temperatures.

Intermetallics are not only formed during the reflow bonding but can also gradually grow at high temperatures after the bonding process. Therefore, the growth of intermetallics at high temperatures may result in more brittle fractures at cryogenic temperatures. For example, the intermetallics at the interface of the solder joint and die/substrate can grow gradually during the daytime of the moon, due to the elevated melting temperature (125°C) for the indium solder joint. But, the growth of excessive intermetallics during the daytime might accelerate and lead to the brittle fractures at the solder joint interfaces during the isothermal-fatigued condition of the lunar night. Thus, there is a tradeoff between intermetallic strengthening and premature brittle fracture. Studies of the effect of intermetallics on fatigue failure of solder joint in cryogenic environment have been conducted for first time in this thesis.

2.2 Constitutive Properties of Indium

As discussed previously, indium attach is a dominant site for fatigue failure. A complete understanding of the deformation behavior of indium is therefore central to the evaluation of its reliability and prediction of its fatigue life.

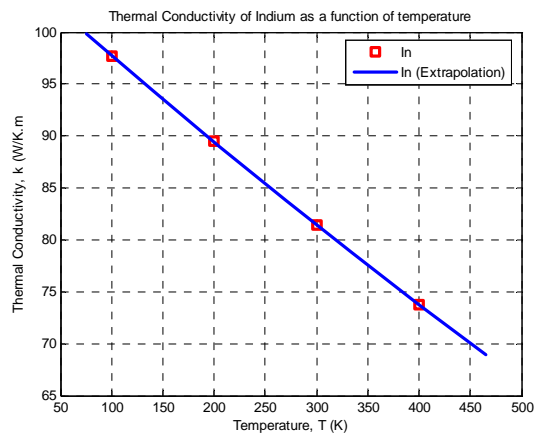
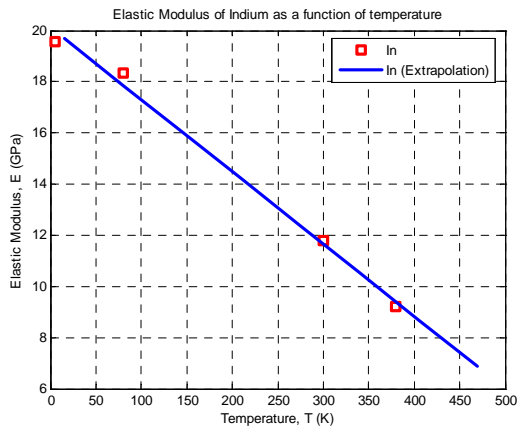
The crystal structure of indium is body-centered tetragonal, its true space group is D_{4h}^{17} , $A=2$; with nominal lattice constants of $a=3.2512\text{\AA}$, $c=4.9467\text{\AA}$, $c/a=1.5215$. However, its low temperature deformation properties have been shown [0] to be comparable in ductility to face-centered structures.

Previous researchers have discovered that the behavior of indium is strongly temperature- and time-dependent, as shown in Figure 3 [0,0,0,0]. It exhibits as creep and stress

relaxation at high homologous temperatures [0,0,0], which obeys the Weertman-power-law relationship (Figure 5). At low temperatures, it behaves viscoplastically, as do most other metals [0,0].

Elastic deformation is described with Young's modulus, E , is used to represent the linear relationship between normal stress and strain. E is a temperature-dependent material constant (Figure 3). Elastic deformation is recoverable, whereas inelastic deformation is permanent. For a solder joint material, mostly inelastic deformation occurs during temperature cycling or power cycling and it is the root cause of fatigue failure.

Thermal conductivity is utilized to represent the heat conduction capability of material. It is also a temperature-dependent material constant. The temperature dependence of these properties has previously been published in the literature [0,0,0,0].



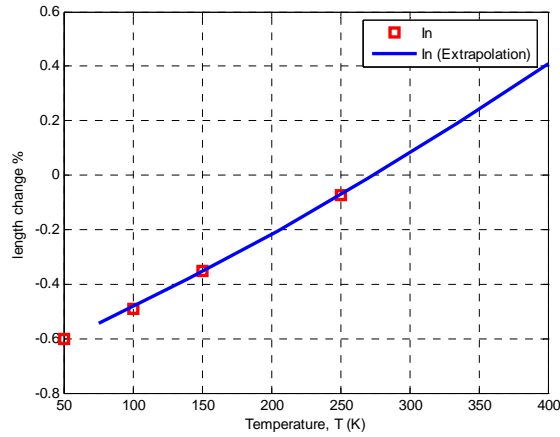


Figure 3. (a) Elastic modulus, (b) thermal conductivity and (c) CTE of indium as a function of temperature

Accurate constitutive relations for solder joint materials are central to the proper application of modeling techniques. There has already been a great deal of effort applied to determine constitutive models for SnPb-based solders, especially the eutectic and near-eutectic SnPb-based solders, e.g., 60Sn40Pb, 63Sn37Pb, and 63Sn36Pb2Ag, and some lead-free solders, e.g. SnAg solders [0,0,0].

In addition to their temperature-independent material properties, mentioned above, the behavior of soft solder joints is also time-dependent, exhibiting viscoplasticity, creep and stress relaxation. When the test specimen is subjected to a constant load, after the initial time independent response, the effects of creep occur in three stages: primary, secondary and tertiary creep (Figure 4). During primary creep, metals strain-harden. The creep strain-rate decreases over time, as hardening of the metal makes creep increasingly difficult, leading to a region of steady-rate called secondary creep. For most metals, secondary creep is the dominant deformation mode at temperatures above half the melting point (T_m). When the amount of strain is very high, creep fracture or rupture will occur. In the tertiary region the high strains will start to cause necking in the material just

as in a uni-axial tensile test. This necking will cause an increase in the local stress which further accelerates the strain in the attachment. Eventually the material will pull apart in a ductile fracture around defects in the solid. The melting point for pure indium is $156^{\circ}\text{C} = 429\text{K}$, so $1/2 T_m = 219\text{K} = -54^{\circ}\text{C}$. As most metals exhibit creep by $0.5T_m$, this indicates that indium solder readily creeps at temperatures well below room temperature. The relationship used to represent the steady state creep of solder in shear is shown in Figure 4:

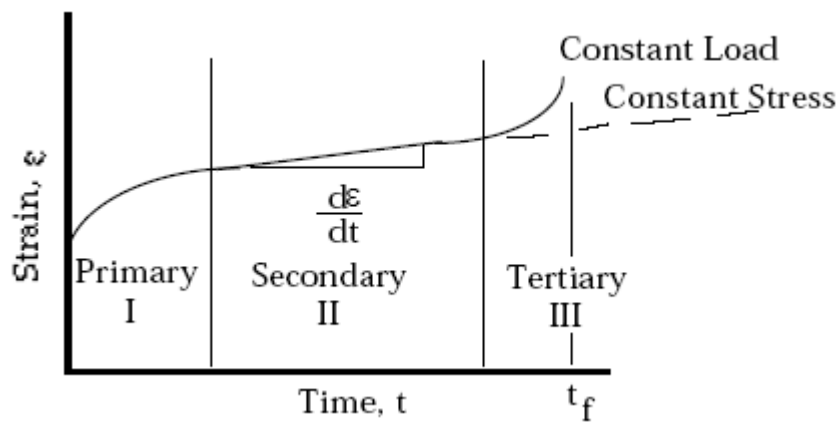


Figure 4 Schematic of strain vs. time curve for a creep test [0]

Little information exists on the time-dependent constitutive properties for pure indium and indium alloy (InBi, InSn) solder joints at subzero temperatures. The only available validated model for indium is the Weerterman-power-law relationship for temperatures above $0.5T_m$, which has the following form with exponent constants found by curve-fitting in Figure 5:

$$\dot{\epsilon}_p = A_0 e^{-\frac{Q}{RT}} \left(\frac{\sigma}{E} \right)^n \quad (\text{Power-law}) \quad (1)$$

where Q is activation energy, $Q = 77.9$ KJ/Mol; R is gas constant, $R = 8.314$ J/Mol; E is the elastic modulus, as a function of temperature; A_0 is a prefactor; and n is the exponent constant, $n \cong 5$.

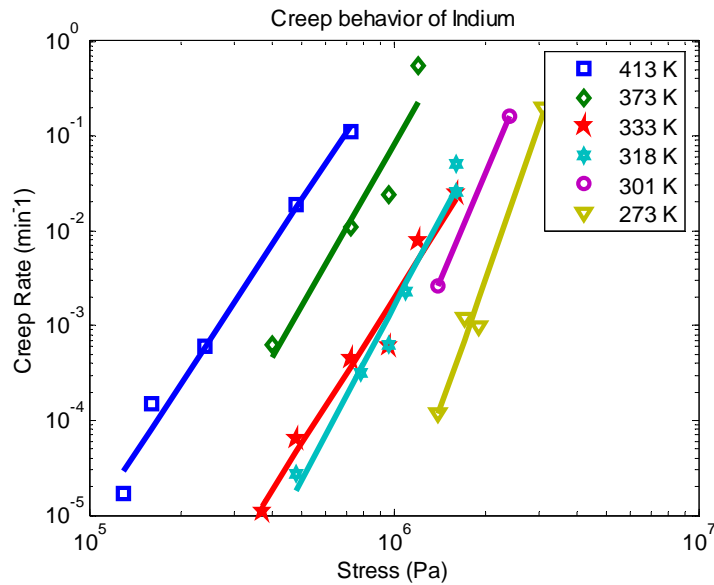


Figure 5. Creep rate of indium as a function of applied stress at different stress levels and different temperatures [0]

The exponent constant n changes with temperature, as listed in Table 1. It is higher at lower temperatures; in other words, the slope of the log-log plot is steeper. This is because the solder joint becomes much stiffer at very low temperatures than at room temperature and undergoes higher stress at low temperatures under the same strain amplitude.

Temperature (K)	413	373	333	318	301	273
n	4.8823	5.642	5.1028	6.0844	7.6432	9.1869

Table 1. Exponent constant of indium at different temperatures

Various stress regimes in the steady state creep of pure metals and solid solution alloys produce different dominant deformation mechanisms as listed in

Table. 2 with respect to different n values [0,0]. It was proven that the stress levels relevant to packaging applications for solder joints under both field operational conditions and accelerated test conditions are in the intermediate and high stress regimes [0]. Dislocation climb was indentified as the dominant deformation mechanisms in indium at its elevated temperatures by Frenkel [0] and the values of n are also consistent with those in the table. At lower temperature, the higher stress, places indium in the power law breakdown region, which is a reason for the shift to a different constitutive modeling approach.

Stress regime	n	Dominant Mechanism
Low	1	Diffusion creep
	2	Grain boundary sliding
Intermediate	3~4	Dislocation glide
	5~7	Dislocation climb
High	>10	Power law break down

Table. 2 Creep Mechanisms in pure metals and solder alloys.

A different constitutive relation for indium is central to the proper application of modeling techniques and fatigue life prediction. This power law break down region must be incorporated into the model as temperature decreasing or stress level increasing in packaging applications. Therefore, a model with n as a function of temperature, or another type of expression, is needed to describe the deformation behavior of indium over

the whole temperature range from -150°C to 120°C (for moon exploration).

Constitutive models to describe this complex time-temperature dependent deformation behavior of solder joints in electronic packaging applications can be basically divided into two categories: elastic-plastic-creep (EPC) and viscoplastic constitutive equations.

The elastic-plastic-creep analysis approach employs separate constitutive models for time-independent plastic deformation and time-dependent creep deformation [0,0,0,0,0,0]. The phenomenological modeling approach illustrates the different plastic and creep deformation behavior. The total strain can be expressed as the sum of elastic strain ($\varepsilon_{elastic}$), time-independent plastic strain ($\varepsilon_{plastic}$), time-dependent primary creep strain (ε_{pcr}), and steady-state creep strain (ε_{scr}) given in (2) ($\varepsilon_{total} = \varepsilon_{elastic} + \varepsilon_{plastic} + \varepsilon_{pcr} + \varepsilon_{scr}$) [0,0,0,0,0,0]. The partitioning of the inelastic energy is given in (3)

$$\varepsilon_{total} = \varepsilon_{elastic} + \varepsilon_{plastic} + \varepsilon_{pcr} + \varepsilon_{scr} \quad (2)$$

$$\Delta W_{inelastic} = \Delta W_{plastic} + \Delta W_{creep} \quad (3)$$

$$\text{with } \varepsilon_{plastic} = C_2 \left(\frac{\tau}{G} \right)^{m_p}; \quad \varepsilon_{scr} = \dot{\varepsilon}_{scr} \cdot t, \quad \varepsilon_{pcr} = \varepsilon_t [1 - \exp(-B \dot{\varepsilon}_{scr} t)].$$

where τ is the applied shear stress (if shear is the dominant deformation mode), G is the shear modulus, C_2 is the plastic strain coefficient, m_p is the stress sensitivity of plastic strain, ε_{scr} is the steady-state strain rate. B is the transient creep coefficient, ε_{pcr} is the primary transient creep strain, and t is the time, respectively.

The steady-state creep rate can be described by a single expression. A hyperbolic sine form from Darveaux and Baneji [0] is the most widely-used formula, which is effectively representing the steady state creep driven deformation by dislocation motion and power law breakdown creep. A hyperbolic sine dependence of the strain rate on the stress results from an assumption of forward and backward thermal activation of vacancies. That is

$$\dot{\varepsilon}_{scr} = C_1 \frac{G}{T} \exp\left(-\frac{Q}{RT}\right) \left[\sinh\left(\alpha \frac{\tau}{G}\right) \right]^{n_s} \quad (4)$$

where C_1 is a coefficient, α the multiplier of stress, and n_s is the stress sensitivity of the steady-state creep rate, respectively. To obtain the total inelastic strain, the temperature dependence of the shear modulus G must be incorporated

$$G = G_0 - G_1 \cdot T(^{\circ}C) \quad (5)$$

where G_0 is the shear modulus $0^{\circ}C$, and G_1 gives the temperature dependence.

For the elastic-plastic model, the solder is assumed to exhibit elastic and then perfectly plastic behavior after yielding. The time-independent plastic behavior, characterized by non-recoverable strain, begins when stresses exceed the solder yield stress. The yield criterion for plasticity of solder is based on the VonMises yield criteria. The equivalent VonMises stress computed in the FEA given in (6) is compared to the temperature and strain rate dependent yield stress given in (8) of 63Sn–37Pb solder as an example, to determine the yield state condition. The elastic modulus and yield stress are taken to be temperature dependent, where a strain rate value of 1E-5 is used in the solder alloy when subjected to a temperature cyclic loading condition.

$$\sigma_{\dot{\epsilon}} = \frac{1}{\sqrt{2}} \left\{ (\sigma_1 - \sigma_2)^2 + (\sigma_1 - \sigma_2)^2 + (\sigma_1 - \sigma_2)^2 \right\}^{\frac{1}{2}} \quad (6)$$

$$\begin{aligned} E(\text{GPa}) &= f(T, \dot{\epsilon}) \\ &= [(-0.006T + 4.72) \log \dot{\epsilon}] + (-0.117T + 37) \end{aligned} \quad (7)$$

$$\begin{aligned} \sigma_y(\text{MPa}) &= g(T, \dot{\epsilon}) \\ &= (-0.22T + 62) \cdot \dot{\epsilon}^{(8.27E-5T+0.00726)} \quad \text{for } \dot{\epsilon} \geq 5E-4 \text{ s}^{-1} \\ &= (0.723T + 105.22) \cdot \dot{\epsilon}^{(1.6224E-3T+0.1304)} \quad \text{for } \dot{\epsilon} < 5E-4 \text{ s}^{-1} \end{aligned} \quad (8)$$

where temperature is in Kelvin.

In viscoplastic analysis, a rate-dependent model that unifies creep and plasticity was first proposed by Anand [0] and Brown *et al.* [0]. Anand's model employs a simple set of constitutive equations for materials with large, isotropic viscoplastic deformations but small elastic deformations. There are several basic features of Anand's model: 1) No explicit yield condition and no loading/unloading criterion are needed in the model. 2) Plastic strain is assumed to take place at all nonzero stress values. 3) A single scalar (s) is used as an internal variable to represent the isotropic resistance to plastic flow. Anand's model has been validated for 60Sn40Pb and 92.5Pb5Sn2.5Ag at their high homologous temperatures.

Anand's model exactly accommodates the strain-rate dependence on the stress:

$$\dot{\epsilon}_p = A \exp\left(-\frac{Q}{RT}\right) \left[\sinh\left(\xi \frac{\sigma}{s}\right) \right]^{\frac{1}{m}} \quad (9)$$

where $\dot{\epsilon}_p$ is the inelastic strain rate; A is the pre-exponential factor; Q is the activation energy; m is the strain rate sensitivity; ξ is the coefficient of stress; R is the gas constant;

and T is the absolute temperature.

The evolution equation for the internal variable s is derived as

$$\dot{s} = \left\{ h_0 \left| 1 - \frac{s}{s^*} \right|^a \cdot \text{sign} \left(1 - \frac{s}{s^*} \right) \right\} \cdot \dot{\epsilon}_p; \quad a > 1 \quad (10)$$

where

$$s^* = s \left[\frac{\dot{\epsilon}_p}{A} \exp \left(\frac{Q}{RT} \right) \right]^n \quad (11)$$

$$\text{sign}(x) = \begin{cases} -1 & x < 0; \\ 0 & x = 0; \\ 1 & x > 0. \end{cases} \quad (12)$$

where h_0 is the hardening/softening constant; a is the strain rate sensitivity of hardening/softening; s^* is the saturation value of s ; \hat{s} is the coefficient; sign is the sign function, and n is the strain rate sensitivity for the saturation value of deformation resistance. There are nine material parameters in the above viscoplastic Anand model: A , Q , ζ , m , h_0 , \hat{s} , n , a and s_0 , the last being the initial value of the deformation resistance.

The traditional EPC constitutive relations for solder alloys range from elasto-plastic models derived from fitting empirical stress-strain curves to phenomenological models, in which the time-dependent and time-independent deformations are separated. However, from the viewpoint of continuum mechanics, the time-dependent and time-independent inelastic strains are assumed to arise from similar mechanisms due to dislocation motion. Moreover, no yield criterion needs to be defined. So, a unified framework for creep and plasticity of solder materials is inherent and desired [0]. Wang et al. [0] have demonstrated the procedures in parameter determination of the Anand model, using the

material parameters of elastic, plastic and creep deformation behavior by Darveaux and Banerji [0].

Once a constitutive equation is chosen, in this case, Anand model, it can be implemented into an FEA code. The FEA models are utilized to determine the stress-strain relationship, which allows fatigue models to be constructed.

2.3 Effect of Intermetallic Compound on Solder Joint Strength

An intermetallic compound is defined as a mixture of specific proportions of two metallic elements that form a periodic crystalline structure different from those of the original elements [0]. In the electronic packaging industry, intermetallic compounds are often discovered to exist at the bonding interfaces between different components. In every solder joint, between the solder and the substrate, a layer is present containing one or more intermetallic compounds [0,0,0]. This layer is formed at the moment the joint is made and is responsible for the resulting strong bond. However, it may also be responsible for problems in solderability [0,0] and may compromise the future reliability of the joint [0,0,0]. Initial intermetallic bonding layers are usually 1 to 5 micrometers thick and, depending upon conditions, may thicken with time [0]. As solder joints are made ever smaller, the intermetallic occupies an ever greater proportion of the joint, now approaching 10-20%.

Intermetallics have the same high temperature advantages in material behavior as high strength ceramics. Therefore, intermetallics strengthen the solder joint [0], are can improve creep resistance, especially when small and well distributed in the bulk solder.

In addition, the rate of work hardening increases with the volume fraction of intermetallics in the solder joint.

However, one major disadvantage of intermetallics is their limited ductility and toughness, especially at low temperatures. Moreover, during intermetallic growth, voids can develop in one or more of the phases, weakening the bond, and leading to mechanical and/or electrical failure. Void formation during intermetallic growth is often cited as being caused by faster diffusion of In atoms compared to the slower-moving Au atoms (the so-called “Kirkendall effect”). Excessive intermetallics often in combination with those voiding, can cause bond failure, which is differentiated from creep fracture because failure often occurs through the intermetallics layer at a joint interface, due to the porosity and brittleness of the intermetallics themselves [0]. Therefore, there is a tradeoff between strengthening and brittle fracture. Intermetallics are one of the critical factors in determining the life time of the solder joint.

Several intermetallic compounds (Cu_6Sn_5 , Cu_3Sn , and Ni_3Sn_4) are commonly found in the PbSn- and Sn-based lead-free solder joints used extensively in the packaging industry. Physical and mechanical properties relevant to the performance of the joints have been measured in the literature for these materials recently [0]. Generally, within these intermetallics systems, the phase evolution, decomposition, redistribution of intermetallics, and even the solder-joint grain distribution are factors in determining solder-joint fatigue behavior. However, the intermetallic compound in the current work is AuIn since Au is used as the metallization layer. The studies on AuIn intermetallic compounds are more limited, partially due to the high prices and niche application areas

even at room temperature. If enough gold exists, AuIn forms next. If the temperature is raised above the melting point of In (156°C), AuIn₂ will form within seconds, almost immediately upon bonding, and remain stable. The kinetics of the Au-In reaction in bulk materials at different temperatures is shown in Figure 7 [0]. 14-year aging of Au-In alloys showed no decomposition of the intermetallic compounds originally formed [0,0,0]. Additionally, the gold layer and subsequently-formed AuIn₂ prevent indium oxidation, which would otherwise impede the bonding with the substrate [0].

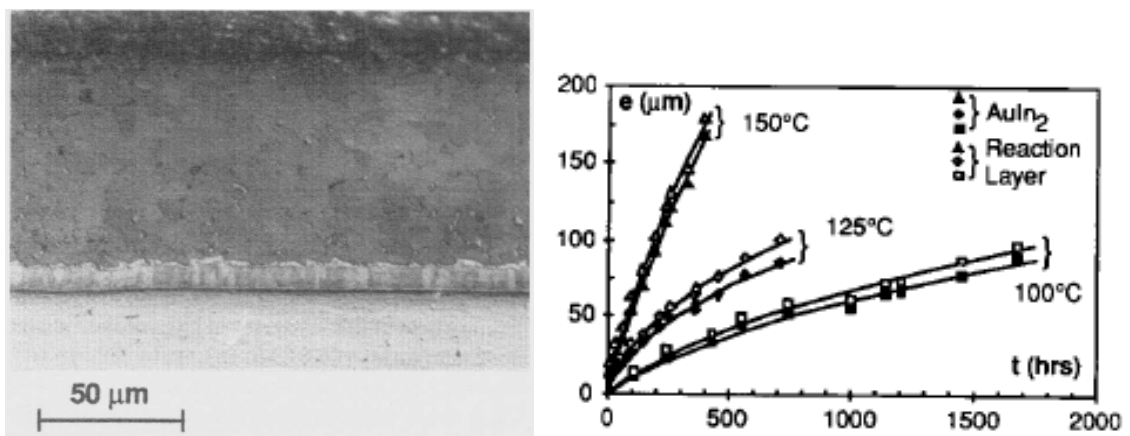


Figure 7. (a) Au-In diffusion couple annealed 144h at 150°C ; (b) kinetics of Au-In reaction at 100,125 and 150°C [0].

In the current work, the Au metallization (less than $3\mu\text{m}$) was always much thinner than indium solder preform (50 to $100\mu\text{m}$). Interdiffusion constants in the solder joint are different from those in the bulk since the amount of Au was limited. Therefore, the diffusion in indium solder joints with different Au coating thicknesses needs to be investigated.

Current available physical and mechanical properties of AuIn₂, Ni-Sn and Cu-Sn intermetallics are listed in the following table as a comparison. AuIn₂ intermetallics have

a relatively lower melting temperature, which may result in a higher ductility than other common intermetallics in the solder joint interface. But still, AuIn₂ intermetallics exhibit the brittleness on the order of other IMCs.

Table 3. Physical and mechanical properties of AuIn, NiSn and CuSn intermetallics.

IMC	Young's Modulus (GPa)	CTE (ppm/°C)	Melting Temperature (°C)
Au [0]	78	14.1	1064.4
In [0]	11	24.8	156.6
AuIn ₂ [0]	N/A	16.3	540.7
Cu ₆ Sn ₅ [0]	86	13.7	415
Ni ₃ Sn ₄ [0]	133.3	11.41	1174

2.3.2 Effect of Bonding Process on Intermetallic Formation

The soldering process plays a critical role in determining the microstructure of the bulk solder, especially the extent and type of intermetallic formation. For indium solder, the effect of the soldering process is much greater than the effect of any subsequent temperature aging. There are several important parameters involved in the soldering profile: heating rate, peak temperature, time above the liquidus point, and cooling rate. Cooling rate is critical in determining the microstructure (grain size and shape, etc.) of the soldering joint. A faster cooling rate commonly results in smaller grain size. And, it is important to put both the mechanical properties and the fatigue data in perspective with deliberate characterization of the microstructure.

The influence of the bonding process on intermetallics has also been studied. No significant variation was observed in the grain size of AuIn₂ as a function of annealing

time and temperature [0]. The shear strength is insensitive to the hot pressing duration as well as the type of bonding process. These features of AuIn₂ can guarantee the relatively uniform and stable bonding quality of the specimen [16].

2.4 Differences in Deformation of Bulk Specimen and Solder Joint

Darveaux [0,0] studied indium solder joint deformation behavior under conditions of shear loading and stress relaxation at room temperature. It was revealed that indium solder joints are more creep-resistant than bulk specimens, as shown in Figure 8. This effect becomes prominent when the solder joint height is reduced to the same order of size as its microstructural features.

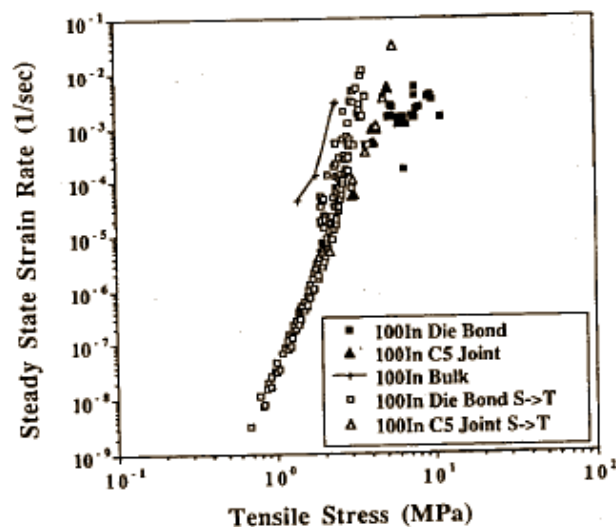


Figure 8. Creep behavior of indium bulk specimen and solder joint [0].

The deformation discrepancy between bulk specimens and solder joints has also been found in other solder joint materials, such as Sn3.0Ag0.7Cu, Sn3.8Ag0.7Cu. The results show that all solder joints have much lower absolute creep rates than the bulk specimen.

The impact of constrained behavior metallurgically increased as the height/radius aspect ratio decreased, resulting in a 2-3x greater tensile strength for die bond joints. This increase is very likely the result of three effects: 1) greater precipitation strengthening from dispersed intermetallics, which serve as potential obstacles for dislocation movements and increase the creep resistance 2) grain/specimen size ratio, and 3) the constraining effect of the solder/substrate interfaces. These effects should be considered when studying the solder joint behavior and even in modeling the solder joint or die attach reliability, especially for die attach applications where the thickness is less than 100 μ m.

In addition, this size effect on deformation behavior is the reason why in this study the low temperature deformation behavior of indium was characterized with the scale of 2mm by 2mm, which is comparable to the size of the die in a real package.

2.5 Fatigue Analysis of Indium Solder Joint

Electronic packages for space applications are subjected to a variety of harmful conditions/environments, two of which are considered in this thesis: (1) thermal cycling and (2) cyclic mechanical loading. Other harmful conditions/environments such as power cycling, moisture absorption and electromigration are not considered in this thesis.

2.5.1 Temperature Cycling on Solder Joint Fatigue

The reliability and life span of cryogenic electronic systems can be significantly degraded by thermal fatigue damage of the die attach and solder joint. This thermal fatigue is induced by the cryogenic constitutive properties of the packaging materials and the large

CTE mismatch between them. The need to model the fatigue behavior of the solder joints has been extensively recognized. The literature on thermal cycling of electronic components containing lead tin eutectic solder is abundant, as accelerated thermal cycling (ATC) testing is one of the most common ways to test solder joint reliability. However, the assumptions and applicability of these models vary, including the manner in which the physical and metallurgical aspects of fatigue are taken into account.

Space exploration not only provides a number of examples of extreme cold environments but also involves wide temperature cycling extremes. For example, in the equatorial region of the moon, the temperature ranges from -180°C (night) to 120°C (day). The temperature environment on Mars is -120°C to $+20^{\circ}\text{C}$. This means space electronics must be able to survive under wide temperature swings, which means higher thermal-fatigue loading.

To develop a fatigue model, one must follow four steps: 1) develop a constitutive equation, which forms the input to the modeling; 2) develop a load transformation model (often FEA) to calculate the predicted stress-strain values; 3) obtain fatigue experimental data from thermal accelerated cycling tests (i.e. thermal shock, temperature cycling and power cycling tests); 4) develop a damage model, used to predict the number of cycles to failure; 5) test and verify results using thermal cycling data.

The complexity of the electronic device structure, the nonlinearity of the packaging material properties, and the transient temperature loading profile make analytical models less applicable than FEM-based models. First, the nonlinear properties for the solder are easily incorporated in an FEM model to capture die attach deformation. Second, using

thermal transient FEM analysis, the temperature profile for the whole module is easy to capture: 3D thermal analysis is first conducted to obtain the temperature profile under temperature/power cycling. Then, the temperature profile is transferred to the 2D diagonal nonlinear stress analysis.

Extensive studies have developed a series of different analytical die attach fatigue model based on fatigue experiments under temperature cycling and power cycling. Those available fatigue models will be reviewed in detail in the next section.

In addition to validating the predicted life against experimental mean fatigue life, analytical/numerical models can be validated using other experiments as well. It is best to validate that the analytical/numerical models are capturing the correct mechanical behavior and that the modeling material properties are correct. This can best be done through failure analysis of failed solder joints in ATC tests to validate predicted failure locations and mechanisms.

2.5.2 Mechanical Fatigue Failure

Besides thermal fatigue induced by lunar daily temperature cycles, the mechanical fatigue at extreme cold temperatures, such as the lunar night with temperature of -180°C , is another concern in the reliability evaluation of the whole electronic package. Only limited published data are available on the deformation of indium and indium-based solders (InBi, InSn) at cryogenic temperatures [0,0,0,0,0]. The information of the fatigue failure site, mode, and corresponding mechanisms in the indium solder joint at cryogenic temperatures has rarely been reported.

Three-point bending and four-point bending experiments are commonly used as the experimental methodology to quantitatively estimate the reliability of the component on boards. The three-point bending methods allows for several packages to be tested at multiple load levels on single test. Four-point bending tests can enable multiple samples to be tested under the same amount of bending moment, which means multiple samples under the same test condition.

In a study by Darveaux [13], grain boundary migration, transgranular cracking, and intergranular cracking were all observed in fatigued specimens at 25°C under strain control. In addition, indium solder joints were found to harden rapidly, reaching a stable hysteresis loop in 2-5 cycles. The load drop was also observed for indium solder joint under the fatigue cyclic loading at room temperature. However, no premature brittle fracture at intermetallic layers was reported in his study.

Transgranular cracking was seen at the surface of a solder joint subjected to 2412 cycles at a strain range of 0.047 in Figure 6. These cracks are located near the silicon interfaces at the leading edge of the joint in the loading direction. An analytical analysis by Suhir indicates that tensile stresses concentrate at the joint edges during shear loading, which would most likely increase the amount of transgranular cracking.

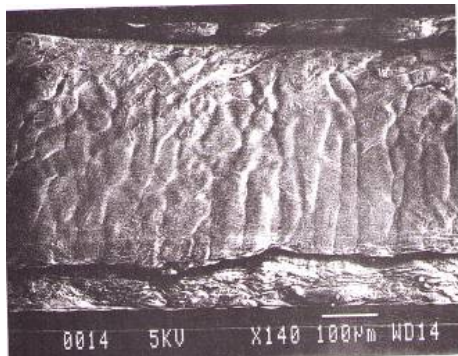


Figure 6. Cross-section showing transgranular cracking under shear loading [13]: 531 micron joint thickness, 297K, 2412 cycles at 0.047 inelastic strain.

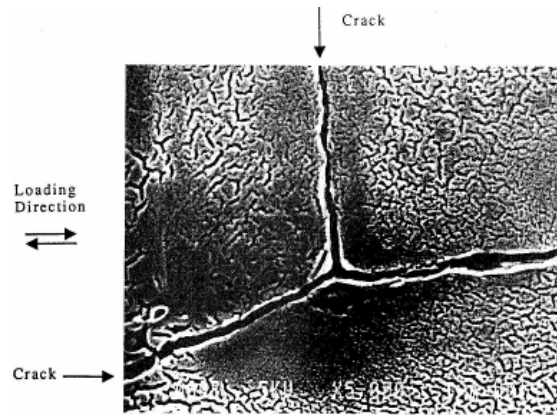


Figure 7. Cross-section showing intergranular cracking [13]: 780 micron joint thickness, 297K, 1134 cycles at 0.028 inelastic strain.

Intergranular cracking is shown in a solder joint cross-section in Figure 7. The sample had been subjected to 1134 cycles at a strain range of 0.028. Grain distortion and cracking were generally less evident in the joint interior than at the joint surfaces. However, no conclusion has been drawn about the relationship of fatigue cracking mode to fatigue conditions and temperatures.

Moreover, indium is known to be very ductile, even down to extremely low temperatures. It has been observed that the fracture surfaces of indium show ductile fracture by dimples at $-196\text{ }^{\circ}\text{C}$ as well as at room temperature [9]. In contrast, PbSn solders have lower ductility, especially the eutectic ones, which makes them unable to compensate for thermal mismatch in low temperature applications. As the temperature goes down, there are two potential failure sites in indium solder joints: 1) brittle fracture in the metallization layer at bonding interfaces and 2) ductile fracture through the solder joint. The occurrence of these failures is affected not only by intermetallic content but also by

temperature loading conditions. Insight into fatigue cracking, such as its sites and its modes in solder joint at cryogenic temperatures, is severely needed.

2.6 Review of Existing Fatigue Model

Some important solder joint fatigue model formats are reviewed in this section, with emphasis on their features and applications. It will also be determined which fatigue model best applies in this case. Successful prediction of solder joint fatigue failure will depend on the ability to accurately model the solder joint. The fatigue models are basically classified into five categories: strain range-based, strain range partitioning (SRP), total energy criterion-based, energy partitioning (SEP), and damage accumulation-based [29-34].

It should be noted that the strain range partitioning model (SRP) and the energy partitioning model (SEP) are only applicable to strain-partitioned constitutive models, where elastic, plastic and creep energies can be distinguished. In the case of a unified viscoplastic model, difficulties are encountered because creep and plasticity can't be separated inside the inelastic strain.

2.6.1 Strain Range-Based Model

Traditional approaches for predicting solder joint fatigue use a fatigue equation with a physics-based damage parameter, such as inelastic strain or total work. A Coffin-Manson type equation [0, 0] is the most popular equation in the literature for predicting solder joint fatigue:

$$N_f = C_1 (Y)^{C_2} \quad (5)$$

where N_f is the fatigue life, in cycles, $C1$ and $C2$ are constants found through least-squares regression, and Y is a damage parameter.

In order to predict the fatigue life, the constants $C1$ and $C2$ must be determined through least-squares regression relating the fatigue life N_f and the damage parameter. The fatigue life N_f is obtained by performing experiments and is given as some percentage of failed samples, typically the mean life of 50% or characteristic life of 63%. At least two experiments need to be performed to determine the two constants. Ideally, more than two experiments would be run in which the design parameters and the loading environment are changed, so as to ensure that the fatigue life is accurately predicted as a function of design parameters and loading environment.

The damage parameter Y is a scalar quantity representing the damage that causes the fatigue failure. Common damage parameters relevant for solder joint fatigue are the inelastic strain range per cycle [0], total strain range per cycle [0], accumulated creep strain per cycle [0], accumulated inelastic work per cycle, the VonMises stress range per cycle, inelastic work per cycle [0], and total work per cycle [0].

The choice of damage parameter will depend upon the loading environment and preference of the researcher. Inelastic strain range per cycle is the most common damage parameter for low cycle fatigue ($<10^4$ cycles) common in thermal-mechanical and power cycling environments. Total strain range per cycle and the VonMises stress range per cycle are the most common for high cycle fatigue ($>10^5$ cycles) where inelastic strains do not play a major role. Lee et al. [0] provides a good review of the choice of damage parameters and fatigue models.

Experiments are required to determine the constants, and are typically collected by application of strain gauges. Actual fatigue tests are often time consuming, and the results are usually applicable only to the specific geometry of the solder joint. FEA modeling is often used to determine the plastic strains, which are then used with the empirically derived constants to predict the fatigue life. This is applicable only for low cycle fatigue. Although with these limitations, FEA modeling is still used as a good initial approach to estimate the time to fatigue failure.

2.6.2 Total Energy Criterion-Based Models

Energy-based fatigue models form the largest group of models [0]. These models are used to predict fatigue failure based on a hysteresis energy term or type of volume-weighted average stress-strain history. Energy criteria are intrinsically multiaxial. The general expression of an energy based model is

$$N_f = C \cdot \Delta W^n \quad (6)$$

where ΔW = energy density per cycle; N_f = cycles to failure; C = fatigue coefficient; n = fatigue coefficient exponent.

In Darveaux's approach [0], which is actually an energy-based approach instead of a damage accumulation-based approach, the expression has two terms, the first for crack initiation (about 10% of the cyclic fatigue life), the second for crack propagation:

$$N_f(63.2\%) = N_o + \frac{a}{\left(\frac{da}{dN}\right)} \quad (7)$$

Thermal cycles to crack initiation: $N_o = K_1 \Delta W_{ave}^{K_2}$

Fatigue crack propagation / thermal cycle: $da/dN = K_3 \Delta W_{ave}^{K_4}$

ΔW_{ave} = averaged viscoplastic energy density dissipated/cycle; a is the equivalent solder diameter or final crack size. N_0 is the cycles to crack initiation, da/dN is the crack growth rate, and $K1$, $K2$, $K3$, and $K4$ are material constants. Anand's model is used so the definition of "plastic" in this case refers to inelastic.

2.6.3 Energy Partitioning Fatigue Model (SEP)

A. Dasgupta, C. Oyan [1992] proposed an energy-partitioning model for creep fatigue analysis. It is applicable to strain-partitioned constitutive models, where elastic, plastic and creep energies can be distinguished. In the case of a unified visco-plastic model, difficulties encounter because creep and plasticity cannot be separated inside the inelastic strain.

In this energy approach, the stress-strain history is used to formulate the elastic strain energy stored and inelastic work dissipated during each cycle. The basic assumption is that damage is caused independently by elastic strain, by plastic energy dissipation and by creep energy dissipation. The inelastic work is further partitioned into plastic energy dissipation W_p and creep energy dissipation W_c per cycle. As shown in following equation, the Coffin-Manson power-law relationship between strain range and life also implies a power-law relationship between energy dissipated per cycle and fatigue life:

$$Energy = U_e + W_p + W_c = U_0 N_f^{b'} + W_{p0} N_f^{c'} + W_{c0} N_f^{d'} \quad (8)$$

$$U_e = U_0 N_f^{b'} = \frac{1}{2} G \gamma_e^2, W_p = W_{p0} N_f^{c'} = \int \tau d\gamma_p, W_c = W_{c0} N_f^{d'} = \int \tau d\gamma_c \quad (9)$$

where G is the modulus of rigidity, b' , c' , d' are the slopes, and U_0 , W_{p0} , W_{c0} are the intercepts of the plots of U_e , W_p and W_c versus cycles-to-failure on a log-log scale. Then the model constants U_0 , W_{p0} , W_{c0} and b' , c' , d' in Equations (8) and (9) can be derived from strain-life fatigue constants. The transformation relations between the strain-life and the energy-life fatigue constants can be derived by starting with a power-law elastic-plastic constitutive model and generic power-law fatigue models.

Chapter 3 Material Characterization of Indium to Extended Cold Temperatures

3.1 Constitutive Properties of Indium

3.1.1 Motivation to Use Constitutive Anand Model

Extensive works have already proposed constitutive models of tin-lead (SnPb) based solder joints, especially near-eutectic SnPb solders (e.g. 60Sn40Pb, 63Sn37Pb) and Sn-based lead-free solders (e.g. SnAg, SnZn and SnSb eutectic solders) at high homologous temperatures. Most of these models were developed by fitting empirical stress-strain curves to a phenomenological model in which the strain rate-dependent and strain rate-independent deformations were separated. Some creep models, such as the power-law creep model [0,0] and the Harper Dorn creep model [0], have been applied to the strain rate-dependent creep data. It is known that the time and temperature-dependent behavior of indium at its high homologous temperature obeys the power-law relationship [0]. However, this relationship breaks down when the temperature is below $0.6T_m$ (-15°C)[11] where the exponential constant (n) in the power-law model ceases to be constant anymore, but rather increases at lower temperature and at higher stress level. This has also been discussed in Section 2.2.

Figure 9 shows the relationship of the strain rate of indium normalized to temperature vs. stress in log-log scale (data referred to [0]). The figure illustrates that all available strain rate data converge into one curve, which is a function of material constants, stress and

temperature. It can be observed that this stress-strain rate relationship is not a power-law relationship anymore, the curvature of which should be a straight line in log-log scale. Moreover, the stress-strain rate relationship tends to curve upwards when stress is rising.

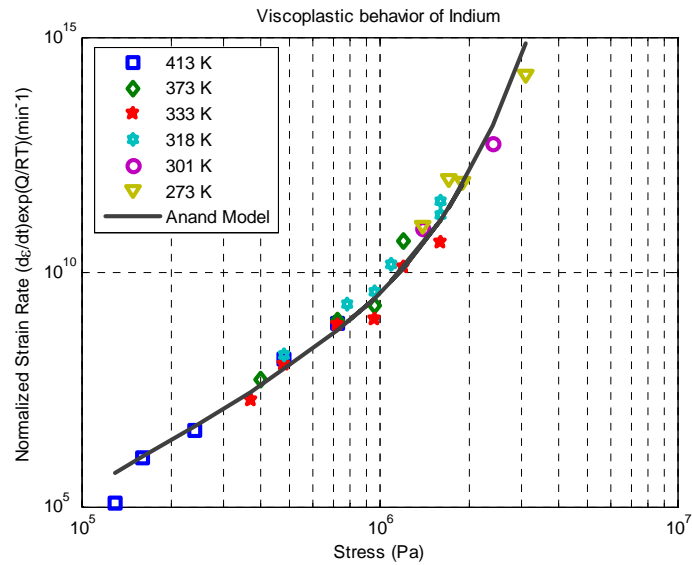


Figure 9 Normalized stress-strain rate in indium at different temperature.

This is because the solder joint becomes much stiffer at very low temperatures than at room temperature, and undergoes higher stress at low temperatures under the same strain amplitude. However, the temperature range for space exploration typically includes extended cold temperatures. For example, temperatures range from -180°C to 120°C for the future Moon rover, which includes the range at which the power law breaks down. An accurate constitutive relation for indium is central to the proper application of modeling techniques and fatigue life prediction. Therefore, a new power law model with n as a function of temperature or another type of expression is needed to characterize the behavior of indium over the entire temperature range.

This phenomenon can also be explained by the physical fundamentals of deformation. It is known that creep and stress relaxation are thermally activated. Since the deformation of indium occurs over a large temperature range, the contribution of thermal energy to the deformation is varied. Therefore, in the temperature range from -180°C to 120°C , the dominant deformation mechanisms vary from those that are active at low temperatures to those that are active at high temperatures, with overlap at some intermediate temperature stages. Traditionally, the plastic deformation of solder alloys has been separated into strain rate-independent plasticity and strain rate-dependent creep. As temperature goes down, the creep becomes less prominent and, other deformation mechanisms have been reported. In fact, twinning has been shown to be one important mechanism at very low temperatures [9]. This overlap and interaction of competing mechanisms at low temperatures makes it difficult to identify the precise role played by each mechanism and to create individual models for each mechanism's contribution in the overall constitutive behavior.

Moreover, from the viewpoint of continuum mechanics, a unified viscoplastic term is more relevant to fundamental deformation physics, since the artificially separated rate-independent plasticity and rate-dependent creep occur concurrently and can both arise from dislocation motion. Furthermore, the parameters in a unified model can be determined directly by combining both rate-dependent and rate-independent inelastic strains into a viscoplastic strain term. Therefore, a model with a unified inelastic form, to represent all low temperature and high temperature deformation behavior, is preferred.

As an alternative to the traditional constitutive model, a unified viscoplastic constitutive model, first proposed by Anand and Brown et al. [0,0], has been commonly used and validated to represent the inelastic deformation behavior of many solder alloys (e.g. 60Sn40Pb, 96.5Sn3.5Ag, 92.5Pb5Sn2.5Ag) at high homologous temperatures. This model was selected for the present work since it can satisfy all the requirements discussed previously about low-temperature deformation modeling. Moreover, the model has simple expressions and is widely available in commercial software (ABAQUS, ANSYS) in contrast to other unified models [0,0], which involve complex calculations of the stress-strain responses, and produce predictions that do not closely correlate with experimental results.

3.1.2 Parameter Determination

In electronic packaging applications, the steady-state plastic and creep deformation processes dominate the deformation kinetics of solder alloys due to their low melting points (Frost and Ashby [0]). As a result, the inelastic response of solders is often treated as steady-state plastic flow. This is the case for Indium, where work hardening occurs only within the first few cycles for larger strains and shorter dwell times. In these cases, the Anand model is simplified to a hyperbolic sine form, where the deformation resistance s equals the saturation value s^* . Then, the evolution equation can be skipped and there will be no hardening and softening effects, that is $h_0=0$ and strain rate sensitivity $a=1$. The strain rate sensitivity for saturation s^* is also set to zero, (i.e., $n=0$). The material model for inelastic response of solders can thus be derived as:

$$\dot{\varepsilon}_p = \dot{\varepsilon} = A \exp\left(-\frac{Q}{RT}\right) \left[\sinh\left(\xi \frac{\sigma^*}{s^*}\right) \right]^{1/m} \quad (10)$$

where $\dot{\varepsilon}$ is the applied strain rate in the constant strain-rate test at a given temperature.

From the above equation, the material coefficients A , Q/R , ξ/s^* , m can be determined by applying a nonlinear curve fitting method. After the determination of these coefficients, the constitutive model can be incorporated into an FEM model that can be used to conduct a thermo-mechanical analysis to simulate the deformation behavior of the indium solder joint under temperature cycling and determine the stress/strain distribution in the electronic module.

3.2 Measurement of Constitutive Properties at Low Temperatures

Accurate constitutive relations for solder joint materials across the application temperature range are essential for reliability modeling. The time-dependent, viscoplastic deformation behavior of indium at subzero temperatures is not available in literatures. Therefore, experiments were designed and conducted to measure constitutive properties of indium solder joints at subzero temperatures. These measurements were then used to validate and calibrate an analytical constitutive model.

The role of compression tests in the study of large deformation of metals is well established (e.g. ASTM-E9 (2000), ASTM-E209 (2005)). As compared to the tension test, one can achieve large strains in a compression test due to the absence of necking. Also, a compression test is easier to perform relative to a torsion test since it permits simpler and more common experimental apparatus and requires less complicated alignment of loading fixtures. Compression testing is particularly appropriate for large deformation testing,

where temperature uniformity is difficult to maintain in tension and torsion specimens, and strain measurement in tension requires complex extensometry [0]. In the specific case, indium is very soft and easily deformed and would therefore have undergone significant damage at the clamping sites in a tension test. This is not a concern in unclamped compressive tests. Last but not least, Anand's constitutive model was validated originally by compression testing. It should be noted that samples must be carefully loaded into the fixture to prevent stressing the material before the test. The compression test was conducted by following the standard: ASTM-E9 (2000) and ASTM-E209 (2005).

Test Standard	ASTM-E9 (2000) and ASTM-E209 (2005)
Test Sample	Solid circular cylinder: Height/Diameter = 1:1
Sample Flatness and Parallelism	0.001 mm/mm and perpendicular to the lateral surfaces to within 0.6 of arc.
Cleaning	Acetone
Lubrication	Mineral oil

Table. 4 Summary of experimental setups.

3.2.1 Sample Preparation

It is recommended by ASTM standard that, where feasible, compression test specimens be in the form of solid circular cylinders. Therefore, indium wires (99.99% pure) with a diameter of 2 mm were cut into 2 mm-long cylinders by following the standard's recommendation and test limits of TA Instruments Rheometric Series (RSAIII) testing machine.

Because of the softness of the indium, it is necessary in sample preparation to address

several concerns, such as the following: 1) Pressure and heat generation must be kept at a minimum to avoid deformation and smeared layers or ghost structures. Problems have been encountered when samples have been cut by machine, since indium wire can melt during the cutting process, which is believed to be due to the low melting temperature of indium and the heat generated by the high speed of the cutting blade.

2) The two end surfaces of the cylindrical sample need to be parallel to make the loading direction perpendicular to the top and bottom surfaces for the test to be pure compression. A customized cutting and sanding fixture was designed to solve this problem. Samples were prepared by hand instead of machine and polished by sand paper to make sure the two cutting end surfaces were parallel, which is critical to the experiment. From the test samples prepared, those maintaining a length uniformity of $\pm 0.1\text{mm}$ and two parallel end surfaces were selected for actual testing. The length of each sample was measured with a digital caliper at three separate locations, as shown in Figure 10. These measured lengths would have the same value if the two end surfaces were parallel. The cylinder end surfaces were assumed to be parallel if the measurements agreed to within 0.01mm , which is within 0.6 of arc.

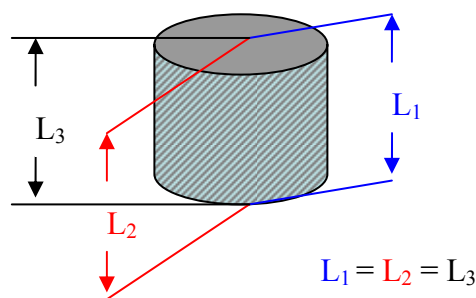


Figure 10 Measured length of specimen at three separate directions.

After the machining, all samples were aged at room temperature for 3 or 4 weeks before testing to ensure complete stress relaxation, since indium is highly rate and temperature dependent. The sample configuration of the loading fixture is shown schematically in

Figure 11.

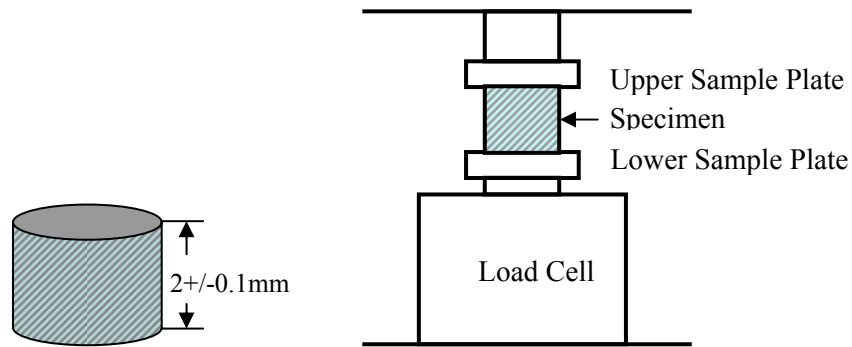


Figure 11 Schematic of indium specimen under the testing fixture in RSAIII

3.2.2 Test Equipment – RSAIII

The TA Instruments Rheometric Series RSA III is a uniaxial tester for miniature specimens that test the dynamic and transient mechanical properties of solid materials by using a servo-drive linear actuator to mechanically impose an oscillatory deformation, or strain, upon the material being tested. The sample is coupled between the motor and a transducer, which measures the resultant force generated by sample deformation. Strain amplitude and test frequency are set by the operator, and the actual sample deformation is determined by the measured actuator and transducer displacement.

The RSAIII system consists of the following three subsystems, as shown in Figure 12:

- Control computer
- RSA test station (motor and transducer)

➤ Environmental control.

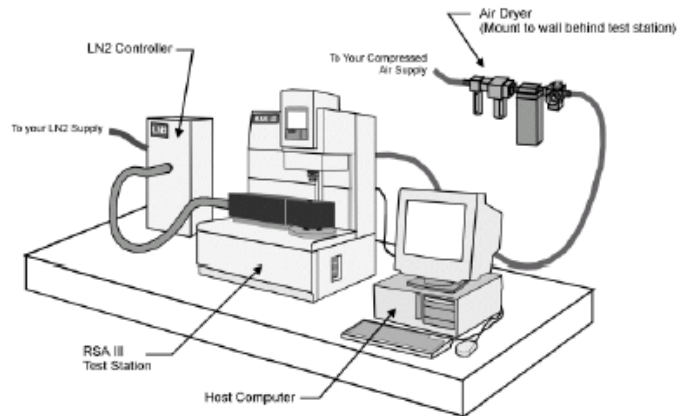


Figure 12. Base system of RSAIII [0]

The main hardware components of the test station are the transducer and the motor. The motor is configured as a position servo. The motor controller uses the command signal to drive the motor, applying deformation to the sample. A feedback displacement signal is derived from a sensor on the motor shaft. The feedback signal is conditioned and set to the A/D input as the strain deformation signal. The motor is capable of loading frequency ranging from 1×10^{-6} Hz to 80 Hz. The response time ranges from less than five milliseconds up to 90% of the target value. It has a load capacity of 35 N (3500 gf) and a load resolution of 0.0002 g. A strain resolution of 0.00005 mm can be achieved during the test.

A forced air convection oven is used to enclose the sample. Two resistive heater guns, mounted on the left side of the oven, are used to control the sample test temperature. A liquid nitrogen controller and mechanical chiller systems allow low-temperature sample testing. The thermal electronics are directed and monitored by the environmental controller that receives its commands from the temperature controller, located within the

control computer. The temperature operating range is from -150°C to 600°C with ramp rates ranging from $6^{\circ}\text{C}/\text{min}$ to $50^{\circ}\text{C}/\text{min}$. The oven has a temperature stability of 0.5°C at thermal equilibrium.

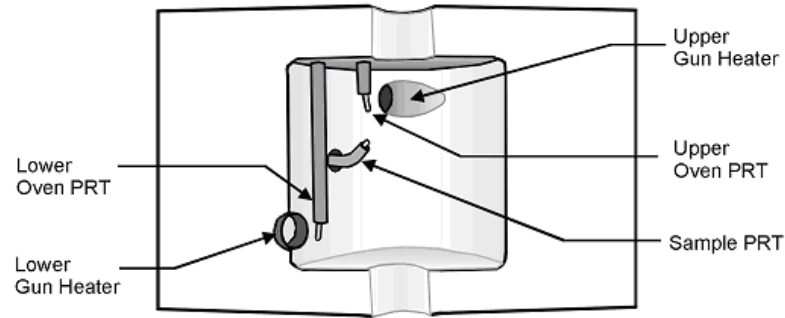


Figure 13. Oven chambers with PRTs [0]

The environmental oven with liquid nitrogen backfill was used to conduct the test at the desired subzero temperatures in this study. There are three temperature sensors in the oven to monitor the temperature on the top of the oven, the bottom of the oven and the top of the sample in the oven, as shown in Figure 13. The experiment was conducted only when the temperature of the sample achieved the target.

3.2.3 Experimental Procedure – Determination of Strain Rate

The specimen was subjected to a constant load level, and increases in strain were recorded with time elapsed. The test procedure was as follows:

Step 1: Selecting sample size using sample testing limits.

The samples were prepared so as to have dimensions in the recommended range of sample geometry as limited by the size of the test fixture. The samples used in this test were solid cylinders having a length of 2mm and a diameter of 2mm.

Step 2: Sample loading:

Samples were loaded according to the instructions below.

Figure 11 shows a sample that has been properly loaded.

- 1) Place the sample on the lower compression parallel plate. Ensure that the sample is centered on the tool.
- 2) Adjust the sample gap until the upper plate almost contacts the specimen.
- 3) Close oven and wait until the required temperature is achieved.
- 4) Offset force to zero after the required temperature is achieved.
- 5) Continue lowering the upper plate until only a slight force is generated.
- 6) Allow the sample to attain thermal equilibrium before beginning testing by monitoring force.
- 7) Enter the sample dimensions on the Orchestrator Test Geometry screen. Note that if the tools were correctly zeroed, the actual sample gap can either be read from the gap real-time parameter, or measured automatically at the start of the test by selecting the “Read Test Fixture Gap” check box on the Geometry screen.

Step 3: Strain-controlled transient compression test:

A series of compressive tests was run at four different ambient temperatures (-145, -100, -50 and 0°C). At each temperature, the specimens were tested under different load levels, and the time dependent inelastic strains were recorded to obtain the strain rate. For the detailed operational procedure of the transient strain-controlled compressive test, please refer to Appendix A.

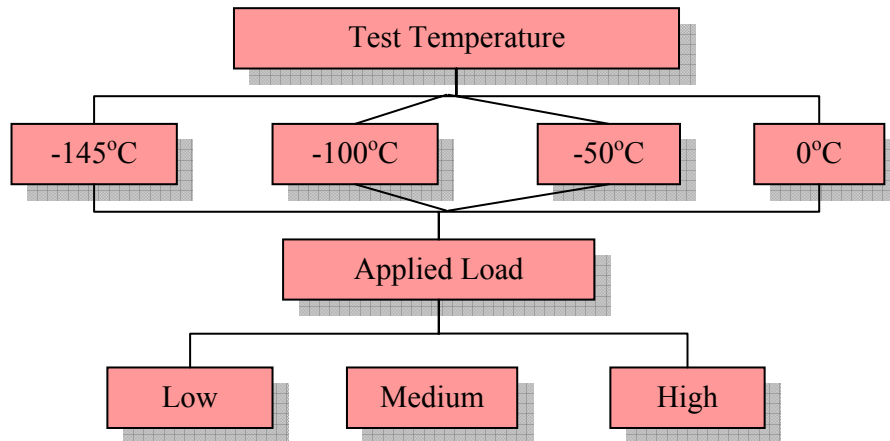


Figure 14. Test matrix of constitutive properties characterization

Then the relationship of applied stress to strain rate was obtained. The test matrix of the experiment is shown in Figure 14 for all conditions. Eight to twelve samples were tested for each condition in terms of temperature and load with a length uniformity of $\pm 0.1\text{mm}$ and temperature uniformity of $\pm 0.5^\circ\text{C}$. The specimens were deformed up to some preset strain, when the crosshead motion was stopped. Then the relaxation time was varied until the thermal equilibrium of samples was attained. At each temperature, the specimens were tested under different load levels, and time dependent inelastic strains were recorded to obtain the strain rate. Then the relationship of applied stress with strain rate was obtained by implementing the viscoplastic Anand model.

3.3 Results & Discussion

3.3.1 Experimental Results

A series of compressive tests at 0,-50,-100,-150°C under different loading force levels (from 100 gf to 3000 gf) was completed. The inelastic strain was recorded as a function of time. Eight to twelve tests were conducted under each condition to study the

consistency, repeatability, and uncertainty of the experiment results. A statistical analysis of test data was completed in order to mitigate the effect of experimental errors on the test results. The data was fitted to a normal distribution and the mean value was used as the characteristic value with a 95% confidence interval.

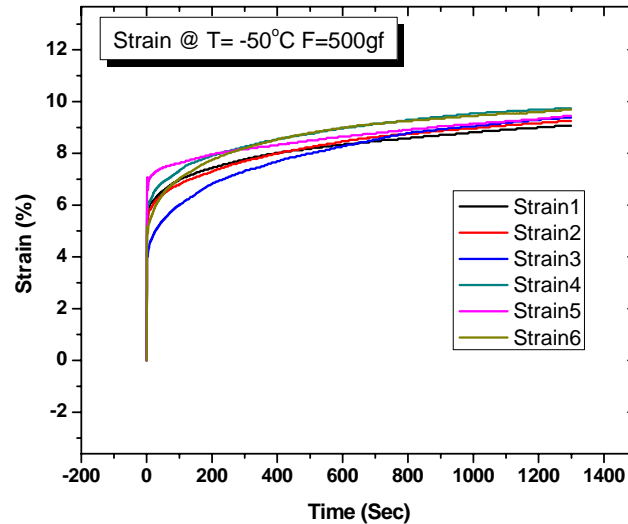


Figure 15 Test sets of time dependent strain at T=-50°C F=500gf

Experimental results from eight test sets with a loading level of 500 gf at -50°C have been plotted as an example in Figure 15, demonstrating the repeatability and consistency of the tests. Each dot represents one test point at one particular time. The histogram plots of these data were also drawn for each data set. A normal distribution was fitted to the test data at each second, as shown in Figure 16. The height of the histogram represents the probability (counts) of a test value at some particular strain value. The mean of the data at each time has been used in linear curve fitting to determine the steady-state strain rate.

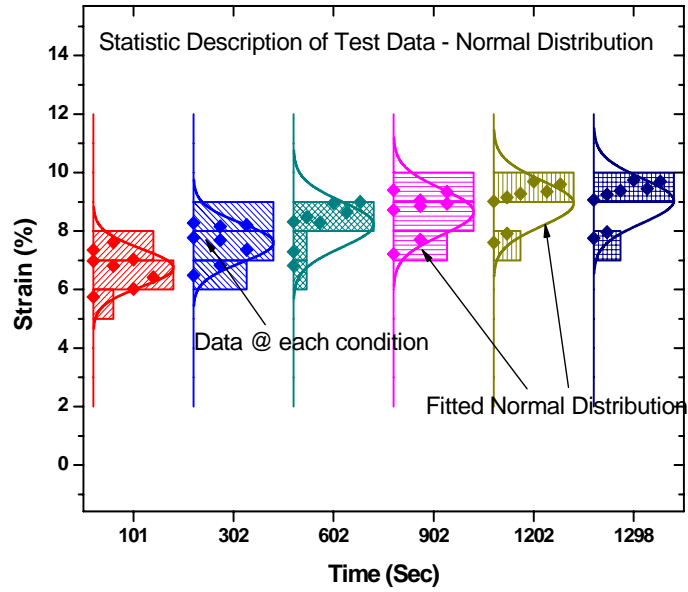


Figure 16 Experimental data post processing – statistical normal distribution

After the mean strain value at each time was obtained, the curvature of strain as a function of time at $F = 500\text{gf}$, $T = -50^\circ\text{C}$, was determined, as plotted in Figure 17. The slope of a linear fit to the data in the steady state regime was used to obtain the strain rate at each stress level at each temperature..

Experimental results for all conditions studied are listed in the following table, which were then used to calibrate the analytical model in Section 3.4.

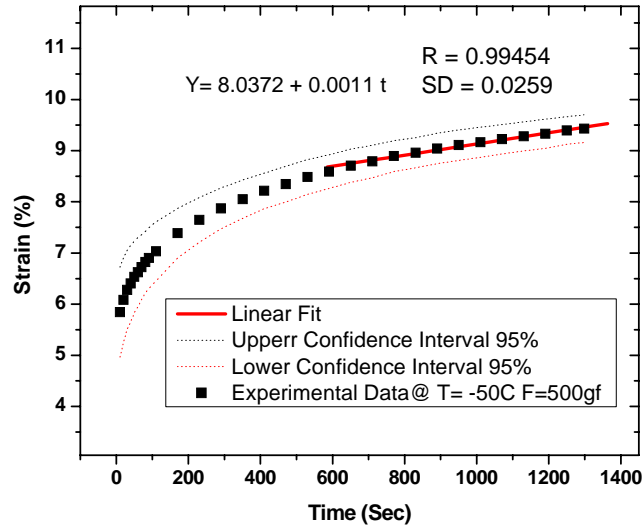


Figure 17. Time dependent strain under loading force 500 gf at -50°C

Table. 5 Experimental results at different temperatures and loading forces

Temperature (°C)	Loading Force (gf)	Normal Stress (Pa)	Strain Rate (sec ⁻¹)
T = 0°C	F = 100	$\sigma = 0.312E6$	$\dot{\epsilon} = 0.132E-5$
	F = 300	$\sigma = 0.939E6$	$\dot{\epsilon} = 0.448E-5$
	F = 500	$\sigma = 1.56E6$	$\dot{\epsilon} = 2.92E-5$
T = -50°C	F = 500	$\sigma = 1.56E6$	$\dot{\epsilon} = 1.10E-5$
	F = 700	$\sigma = 2.19E6$	$\dot{\epsilon} = 2.06E-5$
	F = 900	$\sigma = 2.81E6$	$\dot{\epsilon} = 3.53E-5$
T = -100°C	F = 1200	$\sigma = 3.75E6$	$\dot{\epsilon} = 1.47E-5$
	F = 1500	$\sigma = 4.68E6$	$\dot{\epsilon} = 2.40E-5$
	F = 1700	$\sigma = 5.31E6$	$\dot{\epsilon} = 3.24E-5$
T = -150°C	F = 2600	$\sigma = 8.12E6$	$\dot{\epsilon} = 7.98E-6$
	F = 2800	$\sigma = 8.75E6$	$\dot{\epsilon} = 1.70E-5$
	F = 3000	$\sigma = 9.37E6$	$\dot{\epsilon} = 2.21E-5$

Factors that may affect the experimental results will be discussed in the following sections to make the study systematic and complete, after the strain rates under various stress levels and temperatures have been obtained.

3.3.1.1 Validity of the Experimental Results

One of the methods to check the validity of the experimental results is to compare them with results done by other researchers. As mentioned in Section 3.1, Weertman [0] also conducted experiments on pure indium to measure its steady-state strain rate at 0°C. Therefore, the steady-state strain rate of indium at 0°C was measured in our experiment first to check the consistency and accuracy of the experimental data to those in Weertman [0]. Figure 18 shows the experimental data in our study and those from Weertman [0].

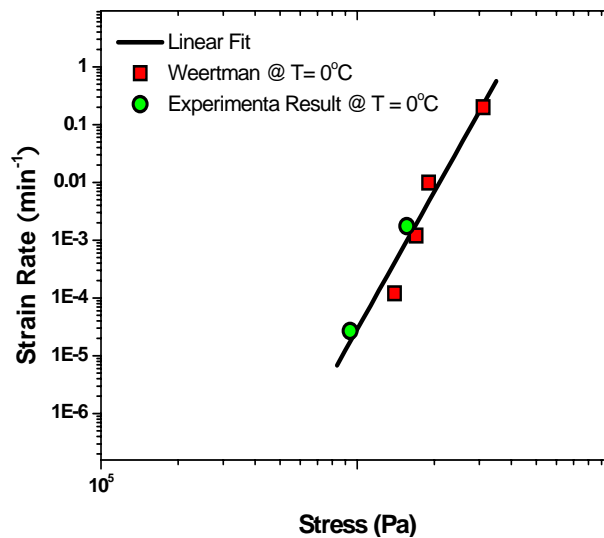


Figure 18. Strain rate from the present experiment and other publications

All stress and steady-state strain rates obey the power-law relationship under isothermal conditions at 0°C, which is a straight line in log-log scale. Moreover, extended lower loading stress levels were measured in our study, and the stress vs. strain rate relationship

at 0°C was extended to an even wider stress range. Experimental results in the present work have very good agreement with those from Weertman [0].

3.3.1.2 Effect of Temperature on Strain Rate

The effect of temperature on deformation behavior, in terms of strain rate, is studied and discussed in this section. The same loading force was applied on samples at different temperatures during the experiment. Figure 19 shows the strain curve at $F = 500\text{gf}$, $T = 0^\circ\text{C}$ with linear fit at steady-state strain. Compared to the plot in Figure 17, the strain rate is bigger at 0°C than at a lower temperature, -50°C, under the same stress levels, which is consistent with theory.

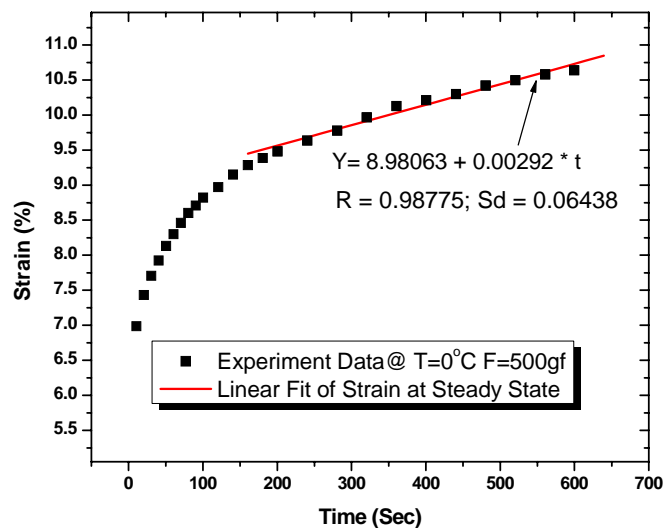


Figure 19 Time-dependent strain under loading force 500 gf at 0°C

When the temperature is decreased to -140°C, the required loading pressure level for inelastic deformation is much higher than it is at higher temperature. For example, the time-dependent, inelastic deformation behavior can barely be observed when 1200gf compressive loading force was applied on the sample at -140°C, as shown in Figure 20. From this point, more loading force was needed for the same amount of deformation and

deformation rate, which is a result of more activation energy needed. It can also be demonstrated that indium is harder and its deformations are more time-independent and plastic at lower temperatures under same loading force level.

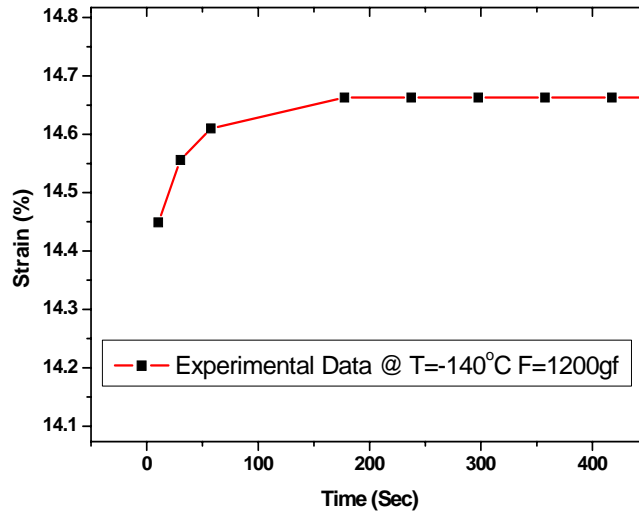


Figure 20 Strain vs. time under loading force 1200gf at -140°C.

3.3.1.3 Initial Sample Length vs. Strain/Strain Rate

The sample used in this study was 2 mm in length, and prepared with a length uniformity of +/- 0.1mm. The sensitivity of strain and strain rate to small variations in initial sample length is discussed in this section, taking the case of a loading force level of 500 gf at a temperature of -50°C.

The effect of initial length on the strain curve has been addressed by studying the differences in the strain at the starting point of the steady state and in the steady-state strain rate. The starting point of the steady state was chosen (Figure 21) since the steady state is what we are interested in our study. Each data point plotted is actually the mean of several test data at this condition, as shown in Figure 21.

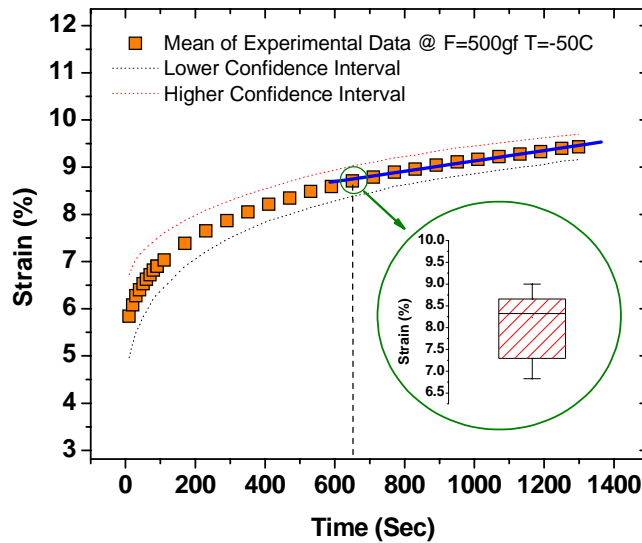


Figure 21 Strains at various test sets at the starting point of steady state

The length difference from the designed value 2 mm and the strain value difference from the normal mean 8.70% of these data are plotted in Figure 22 . The length difference is on the order of 0.01mm and relative strain change is on the order of 0.001. Therefore, the strain is relatively insensitive to small variations in the initial length of the sample.

The strain rate difference from normal mean value at steady state has also been plotted in Figure 23. The length differences are on the order of 0.01mm and the relative strain rate difference is on the order of $0.000001 \text{ sec}^{-1}$. The strain rate is even less affected by small variations in the length of the specimen.

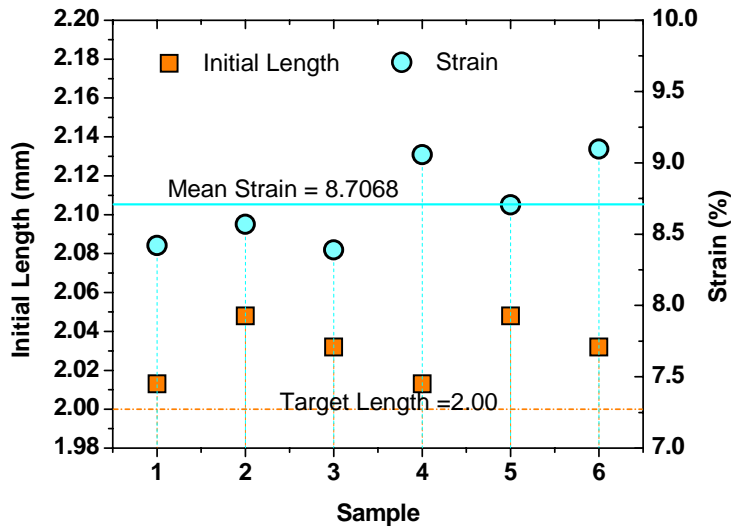


Figure 22. Length differences and strain difference at starting point of steady state

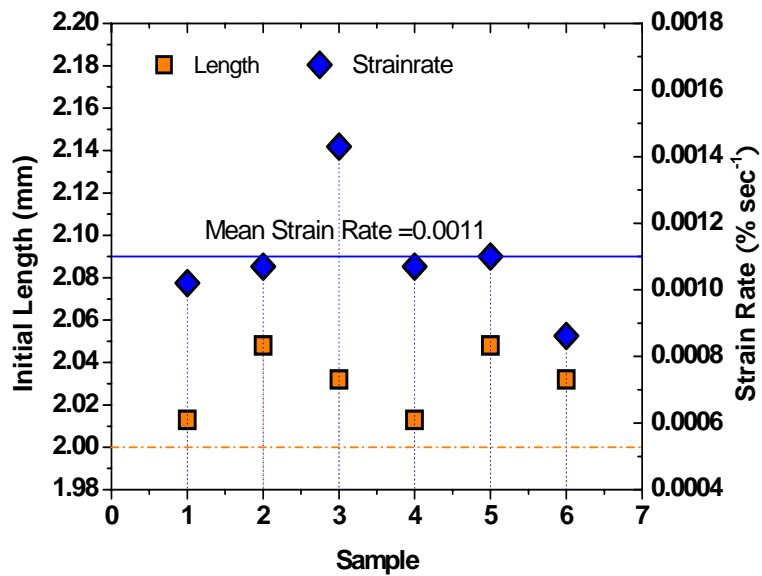


Figure 23. Length differences and strain rate differences at steady state

3.3.1.4 Initial Loading vs. Strain/Strain Rate

As mentioned in the experimental procedure section, a small amount of compressive loading force was exerted at the beginning of the experiment, before the desired constant loading force was applied. The effect of the preload the on strain curve is studied in this

section. The preloading force ranged from a low of 0.79 gf to a high of 7.24 gf at -50°C before the constant loading force of 500 gf was applied. The largest strain deviation from the normal mean was 0.00391.

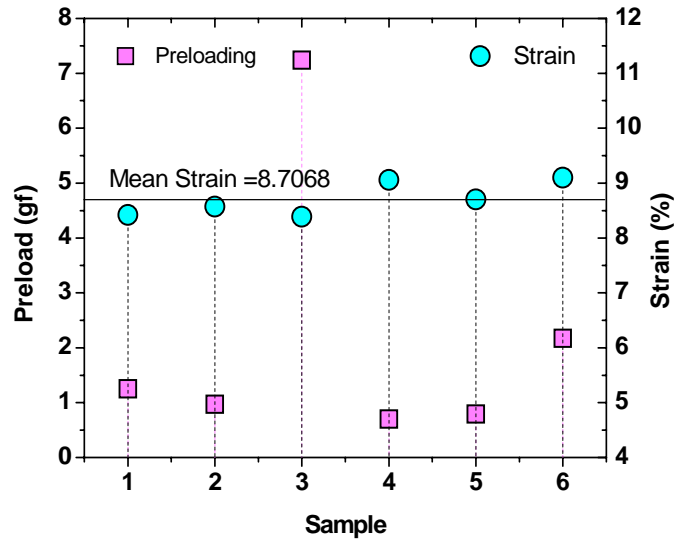


Figure 24. Preloaded force and relative strain difference at starting point of steady state

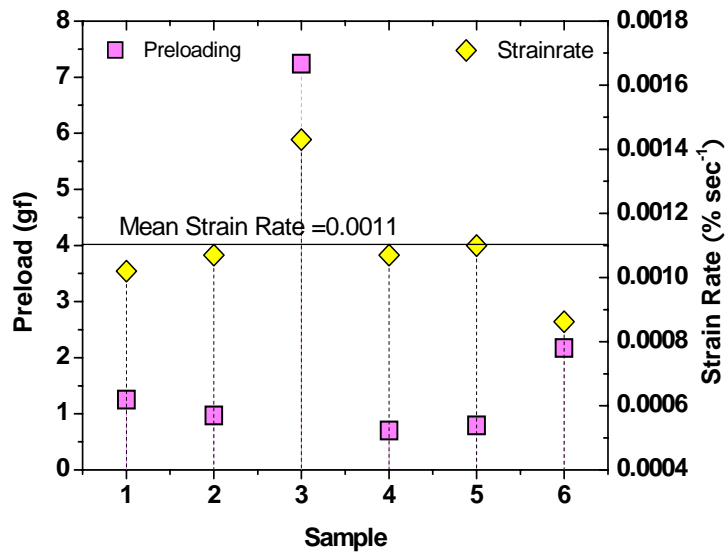


Figure 25. Preloaded force and relative strain rate at steady state

From Figure 24, the strain differences are not correlated to or affected by preloading. The conclusion can be drawn that the strain is not sensitive to the preloading force. The strain

rate is also poorly correlated and relatively insensitive to preloading force as shown in Figure 25.

3.3.2 Validation of Anand Model

The goal of the measurement of material properties of indium at subzero temperatures was to characterize its low temperature deformation behavior, leading either to the development of a new analytical model or to calibration and validation of the existing analytical constitutive model. This material could then be incorporated into an FEM model to predict its fatigue life when subjected to wide range thermal cycling including extended cold temperatures. The motivation of the use of Anand model to describe the deformation behavior of indium at low temperatures has been discussed in Section 3.1. The calibration and validation of the Anand viscoplastic model is discussed in this section.

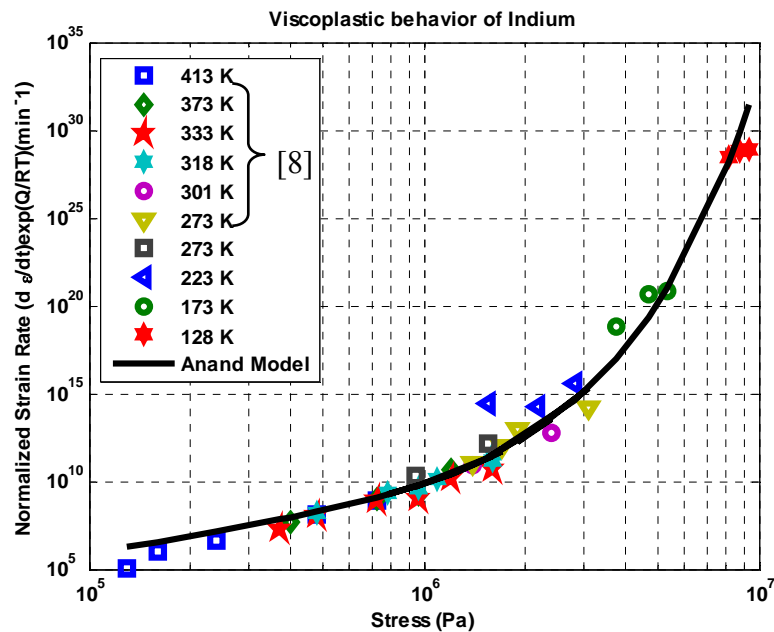


Figure 26 Time-temperature dependent material properties of indium

The time-temperature dependent material properties of indium, measured in the experiment, were input into the Anand analytical viscoplastic constitutive model to determine the Anand material coefficients. The measured low temperature data in our study and those in other references [8] were all plotted in Figure 26. It is easily seen from Figure 26 that all of these data converged into one curvature. The nonlinear curve fitting tool was used to determine the coefficients as listed in Table. 6. Therefore the Anand viscoplastic model has been validated to describe the low temperature deformation behavior of pure indium even down to -150°C.

Solder alloy	Material Parameters								
	A	Q/R	ζ	m	s	n	H_0	A	s_0
In	2.33E8	9369.7	49.97	0.30	2.83E7	0	0	1	2.83E7

Table. 6 Material parameters with Anand model of Indium for steady state plastic flow

Present work showed that a unified Anand model can represent the steady-state inelastic deformation behavior of indium over a temperature range from -150°C to 140°C. Within this large temperature range, the dominant deformation mechanisms in indium vary from low to high temperatures and even occur concurrently at some intermediate temperature stages. It was proven that self diffusion plays a major role in high temperature creep deformation; one possible deformation mechanism is dislocation climb [0].

Indium remains ductile to -196°C [0]. However, in contrast to the high-temperature dominant deformation mechanism of creep, plastic deformation mechanisms are more important at very low temperatures, where thermal energy makes little contribution to the deformation. Slip and twinning are plastic deformation processes that happen without thermal activation. Moreover, twinning tends to be favored over slip at lower

temperatures, for materials with bigger grain sizes and faster strain rates [0,0]. The occurrence of twinning in pure indium specimens has been reported at both -196°C and at room temperature [0]. As temperature is decreased, these deformation mechanisms may occur concurrently and at the lower temperatures, twinning is more favored. Twinning was also observed as the dominant deformation mechanism at -269°C by Reed e.g.[0]. Therefore, dislocation climb, slip and twinning are the possible deformation mechanisms in indium within the temperature range from -150°C to 140°C .

The Anand model was originally proposed for metal deformation behavior at high homologous temperatures and the model was based on the following two physical ideas [0]: 1) plastic deformation due to dislocation motion; 2) a single scalar internal variable to represent the isotropic resistance to plastic flow offered by the internal state of the material. It has already been demonstrated that the model can be effectively used to model the following behavior of metals at high homologous temperatures:

- strain rate sensitivity
- temperature sensitivity
- strain rate and temperature history effects
- strain hardening or softening characteristic
- internal damage and its evolution
- crystalline texture and its evolution

Therefore, the Anand model should also be capable of representing the low temperature deformation behavior of metals. In addition, even if the favored mode of plastic deformation at low temperatures is twinning, the internal state variable formations of

plasticity theory, the simplest and most widely used models, should still be valid. They assume isotropic plasticity and represent the deformation resistance of a material by a single scalar internal state variable, and have already been adopted in the modeling of deformation behavior driven by twinning in polycrystalline FCC metals [0,0]. Moreover, the experiment in the present work has validated that the Anand model can be used to fit the strain rate data obtained. As such, the model has been calibrated and the material parameters have been determined to represent the deformation behavior of indium from a low of -150°C to a high of 140°C.

3.3.3 Correlation of Shear and Compression Loading

Tensile, compression or shear testing are all often-used methods to obtain constitutive properties of solder joints (e.g. 60Sn40Pb, 62Sn36Pb2Ag, 92.5Pb5Sn2.5Ag [0], 97.5Pb2.5Sn [0]). In the present work, compression testing was used to measure the viscoplastic deformation behavior of indium solder joint.

The specimen volume was assumed to remain constant during inelastic deformation as the height decreases and the area increases. Under uniaxial compression loading, the true stress and strain are given by

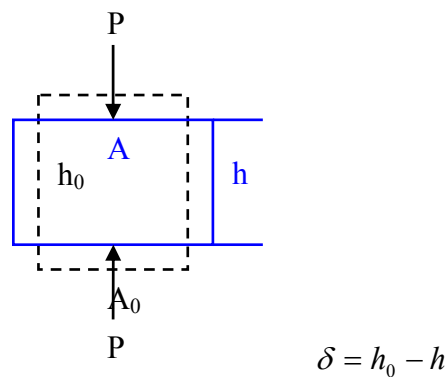


Figure 27 Schematic of sample under uniaxial compression loading.

$$\sigma = \frac{P}{A_0} \left(1 - \frac{\delta}{h_0} \right); \quad \varepsilon = \ln \left(1 - \frac{\delta}{h_0} \right) \quad (13)$$

where σ is the true stress, ε is the true strain, A_0 is the initial loading area, and h_0 is the initial height.

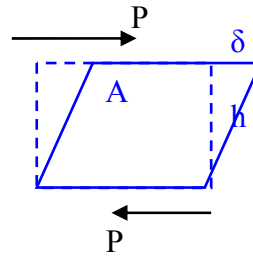


Figure 28 Schematic of sample under simple shear loading.

When the specimen is subjected to pure shear, the shear stress and shear strain can be defined by the following relations:

$$\tau = \frac{P}{A}; \quad \gamma = \frac{\delta}{h} \quad (14)$$

The relationship between the experimental data from each of these tests is needed to convert data to the same loading conditions, which, in the case of solder joints in most electronic packaging applications, represent neither pure shear nor pure tensile/compressive loading. A relationship between shear and tensile/compression deformation is also needed to account for multi-axial stress states. VonMises yield criteria was assumed to apply when the solder joint was subjected to complex loading condition by Darveaux [0], who derived the following relations:

$$\sigma = \tau\sqrt{3}; \quad \varepsilon = \frac{1}{\sqrt{3}}\gamma \quad (15)$$

It was also proven in [0], the material parameters in the constitutive model determined by compression loading test can be correlated with those by shear test from the relationships obtained above. It should be mentioned that the material parameter, s , represents the internal resistance to the plastic flow of one material. Assuming it is independent of the loading state and not changing with respect to compression or shear load [0], the material parameters can be derived for both compression and shear load as listed in the following table.

Material Parameter	Compression	Shear
A (1/sec)	2.33E8	4.04E8
Q/R (1/K)	9369.7	9369.7
ζ	49.97	86.45
m	0.30	0.30
s (N/m ²)	2.83E7	2.83E7
n	0	0
h_0 (N/m ²)	0	0
a	1	1
s_0 (N/m ²)	2.83E7	2.83E7

Table. 7 Material parameters in constitutive model under different loading state.

3.4 Conclusion

In this chapter, the Anand viscoplastic constitutive model was calibrated and validated for indium over the temperature range from -150°C to 140°C, based on fundamental understanding of deformation mechanisms as well as empirical deformation data. The time-dependent deformation behavior of indium at low temperatures has been measured

by constant load compression tests under isothermal conditions at different temperatures. The material parameters of Anand model were determined to simulate the steady-state viscoplastic behavior and stress/strain responses of solder joints in electronic packaging under thermal cyclic loading.

Chapter 4 Thermal Fatigue of Indium Solder Joint

The primary goal of reliability modeling is to develop the capability to assess the time to failure for a structure under all relevant loading conditions. Once predictive capability is established, the model can be used as tool to rapidly evaluate new product designs, and to correlate accelerated test conditions to real field-use conditions. This chapter focuses on the calibration and validation of a physics-of-failure model for indium attach fatigue in cold temperature electronic devices under lunar diurnal temperature cycling.

4.1 Thermal Fatigue of Indium Solder Joint

One major concern in the development of electronic packaging for space exploration is assessing the reliability of the whole electronic system when subjected to numerous diurnal temperature cycles that contain dwells at extended cold temperatures. For example, extreme temperatures on the Moon range from a low of -180°C to a high of 120°C , as recorded by Apollo 17 (see Figure 29). As discussed in Chapter 2, soft solders have been considered for the design due to the operational requirements that the package remain reliable at very cold temperatures during the lunar night. However, this environment also subjects attach materials to temperatures during the lunar day that are near their melting points and well above a homologous temperature of 0.5 (i.e. -58°C for indium). As such, the reliability and life span of the electronic systems can be significantly degraded by thermal fatigue of the die attach and solder joints, induced by their constitutive properties and the CTE mismatch between packaging materials [0,0] (see Figure 2). As a soft solder, indium is subject to thermal fatigue. However, its fatigue resistance is better than PbSn solders.

Tests have been designed and conducted in this chapter to evaluate the thermal fatigue behavior of electronic modules used in the lunar environment. The fatigue life has been predicted based on fatigue data gathered from a thermal shock test. Figure 30 shows the block diagram of the work for fatigue life prediction. The accomplished work will be presented in detail in this section.

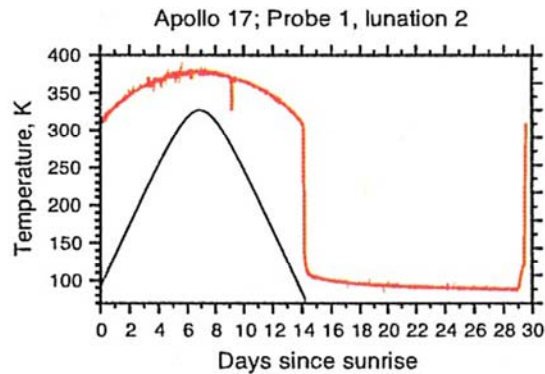


Figure 29 Temperature profile on the surface of the Moon

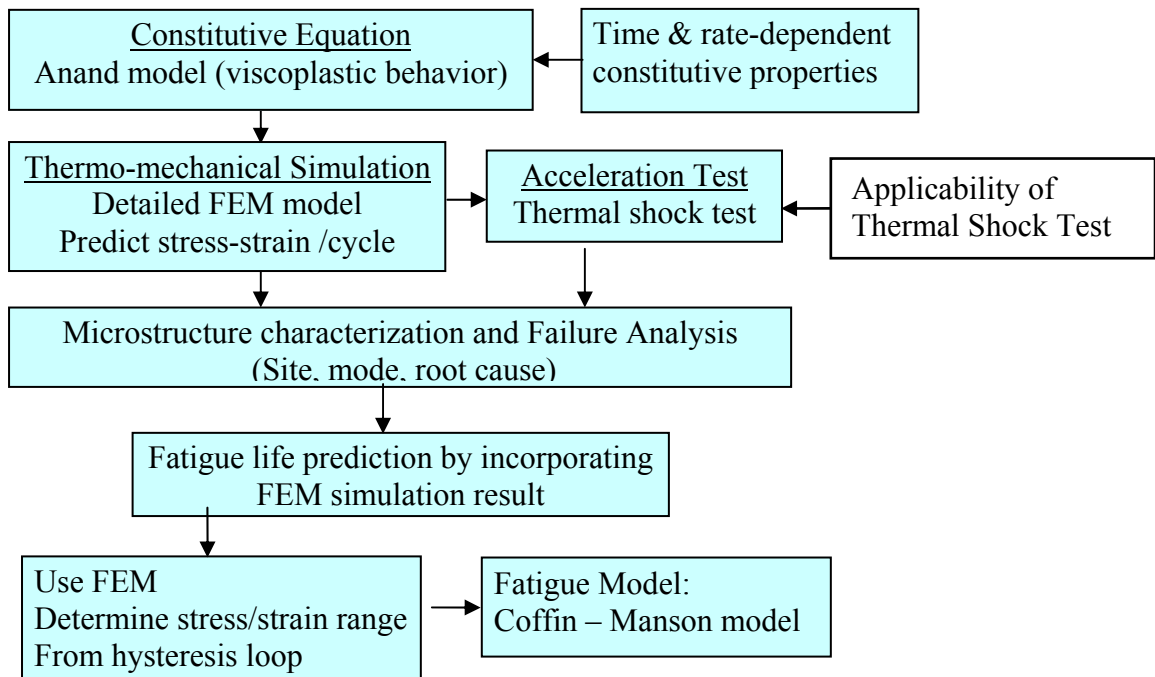


Figure 30 Block diagram of the work in fatigue life prediction.

4.2 Effect of Thermal Cycling/Shock Test on Fatigue Life Prediction

The effect of the experimental evaluation method on fatigue life prediction was considered before the thermal fatigue test was conducted to check the applicability of accelerated thermal shock test to the evaluation of the fatigue behavior of the indium attachment layer in an electronic module.

Thermal cycling (TC) and thermal shock (TS) tests are commonly used for reliability assessment. The advantage of thermal shock tests over thermal cycling tests is that thermal shock can significantly compress the testing time, typically by 5X, reducing the qualification time and cost. Usually, experimental tests (TC and TS tests) on the material can be conducted to obtain the characteristic life using the Weibull failure distribution curve, and a scale factor can be calculated by using $\theta(TS)/\theta(TC)$, as shown in Figure 31. However, the thermal fatigue behavior of the attach material will often be quite different for the different ramp rates and dwell times employed in thermal shock and thermal cycling tests. The fatigue failure site, mode, and failure mechanism may be changed from what occurs under the actual operational conditions [0,0].

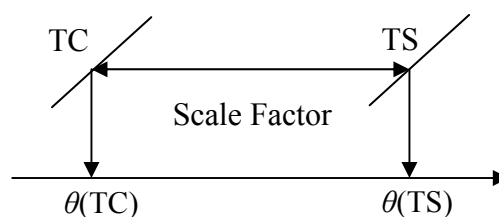


Figure 31. Scale Factor from Weibull curves of TS and TC tests [42]

For this reason, it is necessary to check the effect of thermal cycling vs. thermal shock testing on fatigue life prediction.

4.2.1 Thermal Cycling vs. Thermal Shock Test

The effect of thermal cycling vs. thermal shock testing on fatigue life prediction for eutectic PbSn solder has been reported by Agarwal, et al. As an example, the characteristic life (63.2% of the sample size failed) of flip-chip solder joints was 5229 cycles for the thermal shock test and 2945 cycles for the thermal cycling test for the same temperature range of -50°C to 150°C . The thermal shock and thermal cycling test results show that Pb37Sn solder joints undergoing TC testing have shorter failure life cycles as compared to the TS test [0]. This is there is more damage induced per cycle in thermal cycling than in thermal shock. This difference was also observed in indium solder joints under different loading frequencies over a temperature range from -180°C to 125°C , as shown in Figure 32.

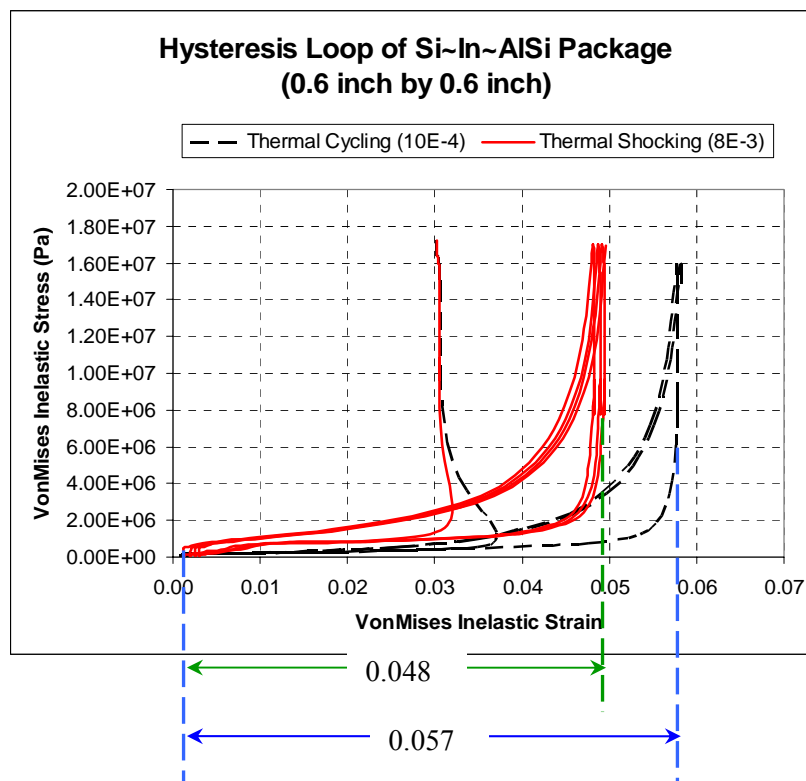


Figure 32. Hysteresis loops of indium solder join at its edge corner under different thermal loadings

4.2.2 Thermal Shock Test for Indium Solder Joint

In real field operation conditions, the temperature cycling during the lunar day and night has a very long period of 28 days. But the accelerated thermal shock test was used in this work to evaluate the fatigue behavior of indium attachment since the currently available temperature cycling chambers can not achieve such low temperature extremes. However, thermal shock test has only 130 second-long period. Therefore, there was a concern whether the thermal shock test could capture the full damage to the indium as would occur under real field conditions.

It is already known that most thermal fatigue damage is induced in the dwell stage in temperature cycling by stress relaxation or creep. Therefore, first, whether the dwell time in thermal shock test is sufficient for complete stress relaxation and creep damage was checked. The stress relaxation at a high-temperature extreme (125°C) in a thermal shock test was simulated. It was found that stress relaxation in the dwell stage is very fast (Figure 33).

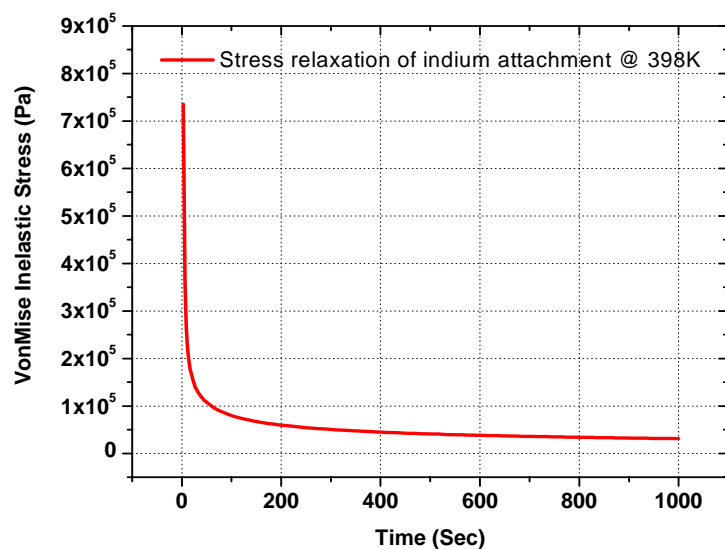


Figure 33. Simulation of stress relaxation of indium attachment at 398K.

Within the 60sec dwell time, the stress was reduced about 71%, as shown in Figure 34. So the dwell time in the thermal shock test is considered long enough for complete stress relaxation and is applicable to evaluate the thermal fatigue damage of indium solder joint in temperature cycling under real field operational conditions.

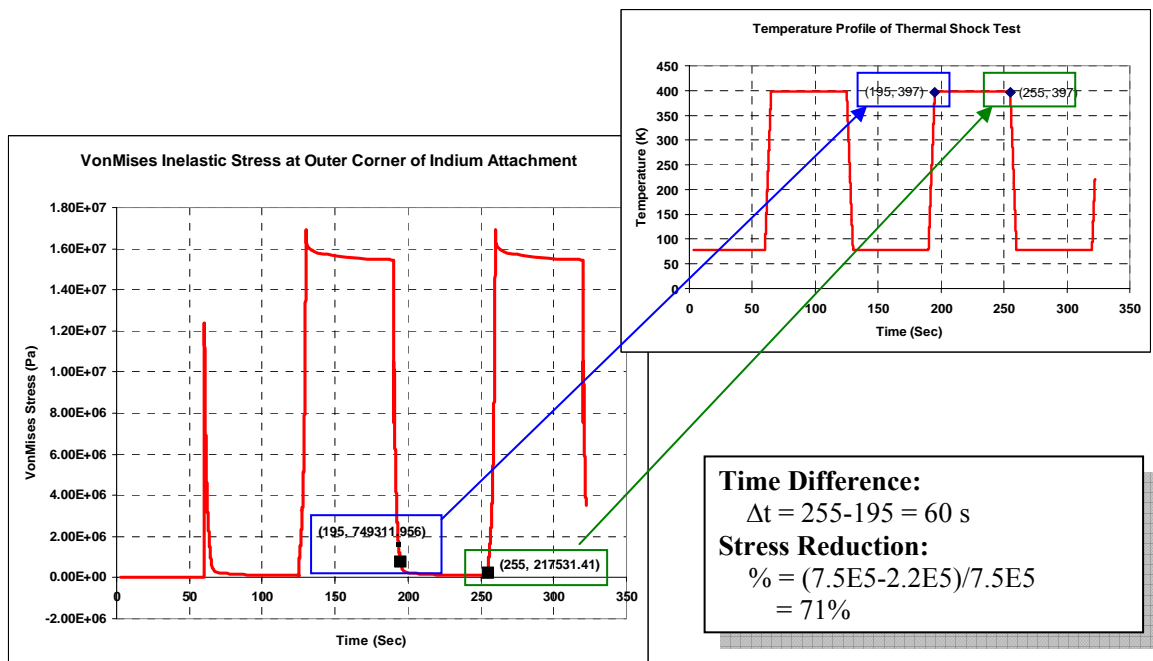


Figure 34. Simulation of stress reduction at dwell stage in thermal shock test

4.3 Thermal Shock Test

Now that the effect of evaluation methods (thermal cycling & thermal shock) on fatigue life prediction has been discussed and the applicability of thermal shock test has been confirmed, the accelerated thermal shock test design and implementation are discussed in this section. The simplified packages with various sizes of die and base substrates were fabricated and tested under thermal shock. Thermal fatigue data were collected and the

physics of failure approach was performed to find the failure sites, modes and mechanisms and to model its fatigue life. Next, the actual package was designed and fabricated based on the prediction from the fatigue model. The whole test vehicle was tested under the same thermal fatigue condition to validate the fatigue model.

4.3.1 Sample Preparation

Samples for the thermal shock test were prepared with various dimensions and material combinations the same as in the simulation. An aluminum-silicon (AlSi) alloy or silicon nitride was used as the base substrate material and silicon (Si) or silicon nitride (Si_3N_4) as the die material. The size of the die was either 0.4, 0.6 or 0.8 inches in length, as shown in Figure 35, taking Si/AlSi specimens as an example. All substrates and dies were coated with Ti/Ni/Au metallization layers to make the silicon and silicon nitride wettable in the bonding process. Then they were bonded together by indium foil, as shown in Figure 36. In each size and material combination, there were at least five samples.

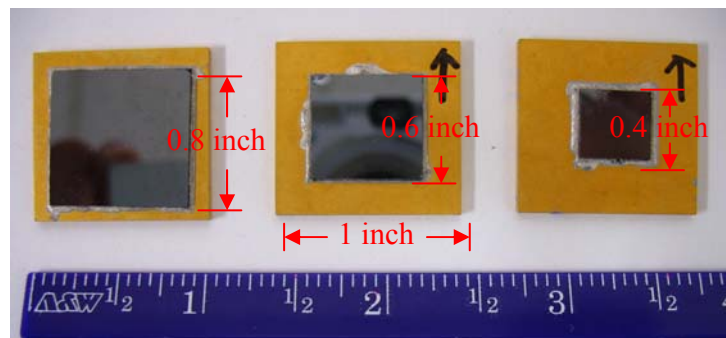


Figure 35. Samples under thermal shock test with different dimensions

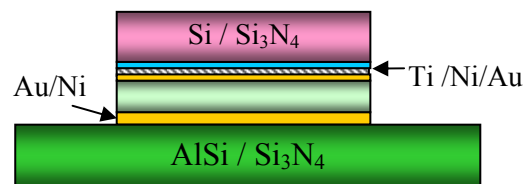


Figure 36. Schematic of metallization patterns in the package

4.4 Test Setup and Experimental Procedure

Thermal shock testing was conducted on these samples. The temperature loading in the thermal shock test was from -196°C to 125°C with ramp time of 5 sec and dwell time of 60 sec at two temperature extremes. After every 50 cycles, the fatigued samples were scanned to obtain C-SAM pictures. Crack-initiation time was based on visual inspection of C-SAM pictures.

4.4.1 Thermal Shock Test Results

Thermal shock testing for packages with various material combinations and sizes was conducted. Since the crack-initiation time was based on visual inspection of C-SAM pictures after every 50 cycles of thermal shock, the test data is considered left censored intervals. So the characteristic life-to-failure was obtained by incorporating the fatigue data into two parameter Weibull failure distribution curve (Weibull 6++) as listed in Table. 8.

Table. 8 Left censored interval fatigue data from thermal shock test.

Number in State	Last inspected	State	State End Time
0.8 x 0.8 (inch x inch)			
1	0	F	50
1	100	F	150
1	150	F	200
1	200	F	250
0.6 x 0.6 (inch x inch)			
1	0	F	200
1	200	F	250
0.4 x 0.4 (inch x inch)			
4	0	F	400

Table. 9 lists the mean-time-to-failure of the different packages from the Weibull plot.

Table. 9 Characteristic life to failure after thermal shock test.

Dimensions	Median Life to Failure	
	Si/In/AlSi	Si ₃ N ₄ /In/AlSi
0.8 by 0.8	160	45
0.6 by 0.6	170	75
0.4 by 0.4	400	110
No failure observed in Si~In~Si ₃ N ₄ packages even after 500 cycles		

From the sensitivity study in Section 4.3, the thermal fatigue life of the Si₃N₄/AlSi package is presumed to be almost the same as the Si/AlSi package under thermal cycling due to their similar CTE mismatches with AlSi. The differences between the Si/AlSi and Si₃N₄/AlSi packages in thermal fatigue life are profound after the thermal shock test, which was the result of different root causes of package failure. This will be discussed in more detail in the next section.

4.5 Fatigue Failure Analysis

With the aim of finding out the root causes of package failure in different packaging materials, failure analysis was conducted based on cross-sectioned samples. The sample preparation was very difficult since indium itself is very soft. Pressure and heat generation were therefore be kept at a minimum to avoid deformation and smeared layers or ghost structures. The following procedure was followed:

- 1) Mounting: cold-setting mounting
- 2) Polishing:
 - a) Wet grinding on SiC papers down to 1200 grit

- b) Fine grinding on diamond wheel (1 μm) to remove SiC particles embedded into indium during wet grinding
- c) With alumina slurry (1 μm), using rotating wheel with a soft cloth and some soap addition, intermittent etching with the etchant (DI water 40ml + HCl (40%) 10 ml +H₂O₂ (30%)10ml)
- d) Ultrasonic cleaning with a solution of DI water and acetone to remove alumina powder on sample surface
- e) Rinsing in DI water and blow-drying by air

Several Si₃N₄/AlSi and Si/AlSi (0.8 by 0.8 inch²) packages were cross-sectioned to analyze the failure sites and their modes. Optical imaging was performed, and root causes of specimen failures were basically divided into three categories:

- 1) Fatigue failure of indium solder joint in Si/AlSi packages
- 2) Interfacial fracture at bonding surface in Si₃N₄/AlSi packages
- 3) Others: metallization delamination, interior AlSi cracking.

4.5.1 Fatigue Cracks in Si/AlSi Packages

Figure 37 shows the growth of a fatigue crack as observed from C-SAM pictures every 50 cycles in a Si/AlSi package. After cross sectioning, only indium solder joint fatigue fracture was seen in Figure 38. The horizontal cracks propagated from the edge throughout the indium die attach layer in the Si/AlSi packages, due to the shearing stress imposed by the CTE mismatch of the die and substrate during thermal loading.

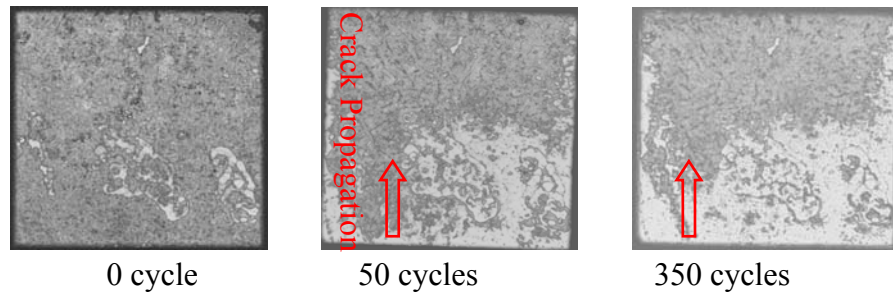


Figure 37. CSAM picture of Si/AlSi package #1 (0.8 inch by 0.8 inch)



Figure 38. Solder joint fatigue failure after thermal shock test.

4.5.2 Interfacial Fracture & Fatigue Cracks in Si₃N₄/AlSi Packages

In contrast to the Si/AlSi packages, fatigue cracks through the indium solder joint and interfacial delamination at the Si₃N₄/In interfaces were both observed in the Si₃N₄/AlSi packages. 1) Cracks propagating through the indium layer were found in the Si₃N₄/AlSi packages as well as in the Si/AlSi packages, as shown in Figure 39(b). 2) Delamination at the Si₃N₄/In solder joint interfaces, as observed in the specimen with shorter fatigue life in Figure 39(a).

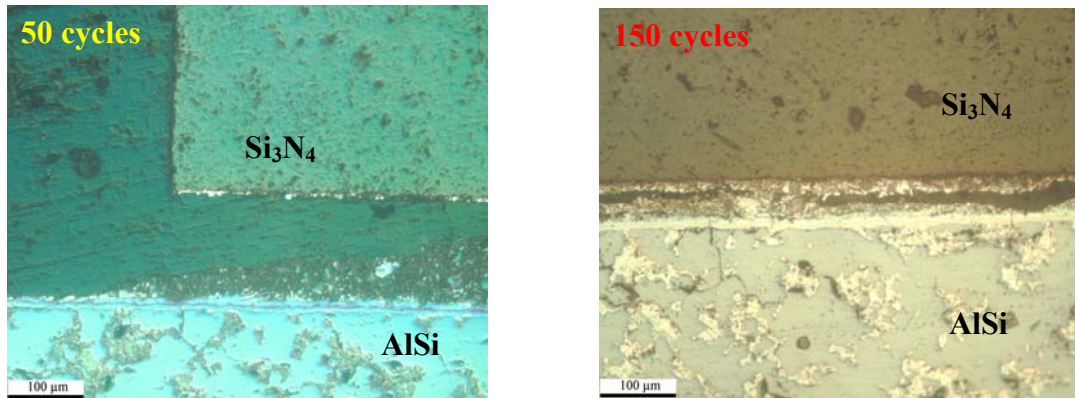


Figure 39. (a) Brittle fracture through intermetallic layer at joint interface with 50 cycles in SiN/AlSi package; (b) fatigue cracking through solder joint with 150 cycles in both Si/AlSi and SiN/AlSi package (0.8 by 0.8 inch)

The attach appeared to be of good quality in these silicon nitride samples. Voids and unbonded areas in the attach layer were not seen in the C-SAM picture before the thermal shock test in Figure 40. Moreover, the fatigue crack in some samples was observed propagating through the indium solder joint instead of as an interfacial fracture at the metallization layer, where the Si_3N_4 was still bonded with the indium solder joint, as in Figure 39 (b). This at least demonstrates that Si_3N_4 and indium could be bonded together before thermal fatigue.

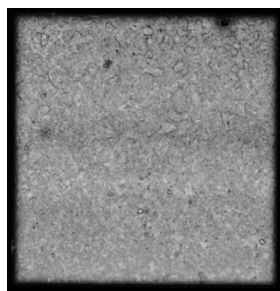


Figure 40. CSAM picture of $\text{Si}_3\text{N}_4/\text{AlSi}$ package (#4) (0.6 by 0.6 inch) before thermal shock test

EDX analysis was performed on the $\text{Si}_3\text{N}_4/\text{AlSi}$ package with interfacial fracture to analyze the fracture surfaces between silicon nitride and indium. Silicon nitride was coated with a Ti/Ni/Au metallization pattern. Au reacted with the indium to form an Au-

In intermetallic compound during the bonding process. EDS mapping on the interface area was performed, and elements in this area are plotted by the location vs. amount in Figure 41. The mapping of Au is shown in Figure 41, and the elemental ratio of Au to In provided by EDS is about $\frac{1}{2}$, which indicates the intermetallic compound is AuIn₂. The interfacial delamination might be the result of intermetallic fracture at interfaces due to its brittleness. This means that in some cases for this package, the thermal shock may have been fast enough to suppress the creep dominated fatigue failure and substitute a brittle failure.

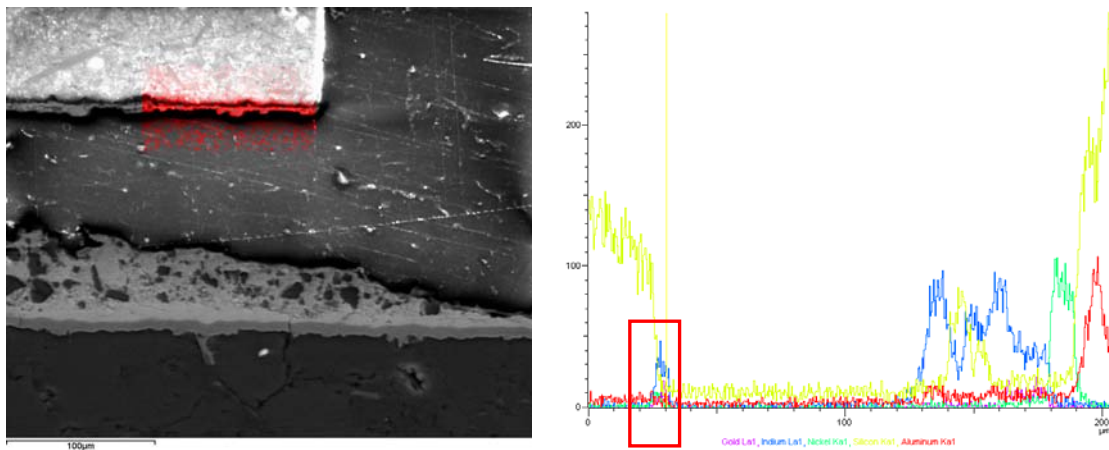


Figure 41. EDS analysis of Si₃N₄/AlSi package (Gold: Purple; Indium: blue;)

4.5.3 Other Failure Sites & Causes

Moreover, vertical cracks were seen at the upper indium attach layer, as shown in Figure 42. (a) Ni/AlSi delamination crack; (b) Vertical crack in AlSi substrate. These cracks inside the indium were much smaller than those cracks at the edge of the indium layer. Metallization delamination at the Ni/AlSi interfaces and vertical cracking in the AlSi housing were also observed. The reason for this might be the condition of the coating process and thermal shock test, which impose higher stress and less stress relaxation due

to a very short ramping rate and dwell time other than thermal cycling. Substrate cracking might also become a reliability concern if it is observed under thermal cycling.

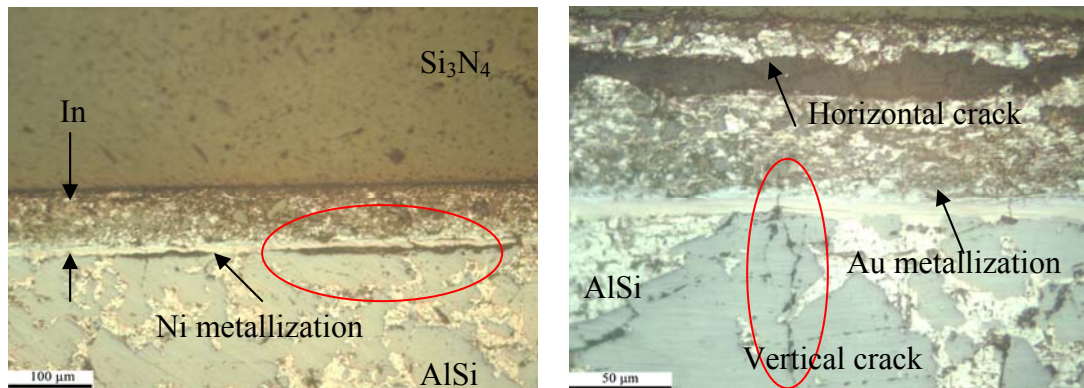


Figure 42. (a) Ni/AlSi delamination crack; (b) Vertical crack in AlSi substrate

4.6 Thermomechanical Transient Analysis

Thermo-mechanical analysis (analytical model/computational model) is involved in fatigue life prediction to calculate the predicted stress-strain values. However, the complexity of the electronic device's structure, the nonlinearity of the packaging materials, and the transient temperature loading profile make analytical models less applicable than the FEM based model. The nonlinear properties for the solder are easily incorporated in the FEM model to capture die attach or solder joint deformation. FEM based modeling is extensively used into other types of packages, such as ball grid array (BGA) packages.

Computational modeling of the temperature and stress distribution of electronic modules during temperature cycling was conducted. First, thermal transient analysis was applied to determine the temperature profile through the whole module during temperature cycling. Second, temperature profile was transferred to a 2D diagonal structural model to

determine the cyclic stress and strain relationship in the whole module, especially in the indium attachment, which is most inclined to fatigue failure.

4.7 Thermal Transient Analysis

Thermal analysis calculates the temperature distribution and related thermal quantities in a system or component. Generally, thermal analysis is divided into two types: *steady state thermal analysis* and *transient thermal analysis*. Transient thermal analysis determines the temperature distribution and other thermal quantities under conditions that vary over a period of time. Thermal transient analysis is used here to determine the temperature distribution in the electronic package under thermal shock conditions. The temperature distribution was then used in nonlinear structural analysis later.

The temperature loading in the thermal shock test was from -196°C to 125°C with a ramp time of 5 sec and a dwell time of 60 sec at two temperature extremes, which was simulated to conform to a test conducted simultaneously (Figure 43).

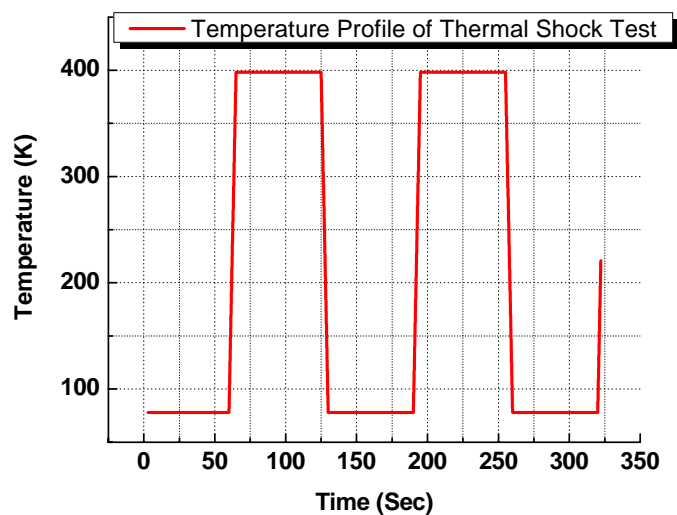


Figure 43. Temperature profile of thermal shock test

4.8 Nonlinear Structural Analysis

Nonlinear structural analysis was then conducted to determine the stress/strain distribution in the whole package during thermal loading, which was simulated in thermal transient analysis at first. Since the deformation behavior of the packaging materials is time and temperature dependent, especially the indium attachment, the large deformation in nonlinear structure analysis is preferred. The impact of critical design parameters on the stress/strain distribution in the electronic module, such as geometry and packaging materials, is also addressed in this section.

4.8.1 Development of FEM Structural Model

The fully parametric input FEM model was created in ANSYS, as shown in Figure 44. For the detailed program code in ANSYS, please refer to Appendix B. Due to the symmetrical geometry, only half of the specimen was meshed with 2D plane strain elements in order to save computing time. In the simulation with the use of Anand model, the material parameters were defined in ANSYS, and a viscous element type (VISCO108) was selected for the indium attach. The multiphysics simulation environment in ANSYS was adopted to simulate the thermal and structural loading environment.

The stress/strain is always concentrated and takes the maximum value at the outer corner of the attachment layer due to the singularity at the free edge and the dissimilar material interfaces. The attachment layer is the indium layer in our electronic module. In order to obtain the precise result of stress/strain distribution and to overcome the singularity at the corner point, a finer mesh was generated at the outer corner of the package, occupying 10% of the side length of the die, as shown in Figure 44.

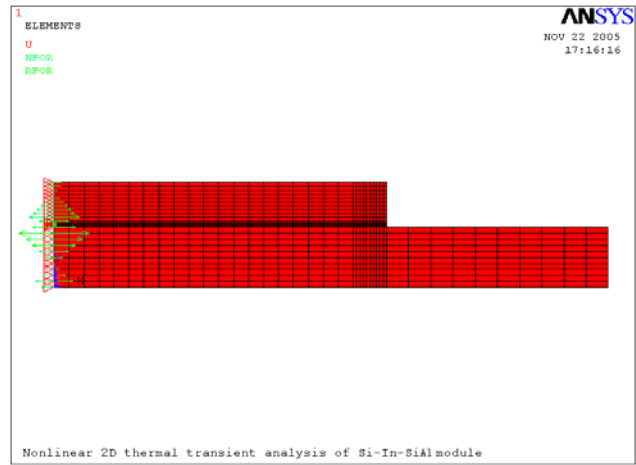


Figure 44 Detailed FEM model in ANSYS

The way to obtain the value of the damage indicator is critical to the fatigue life prediction since the singularity at the edge of the package at different material bonding interfaces causes locally highly concentrated stress/strain. The size of the meshed elements in FEM model and averaged area to obtain the value of damage indicator, here the inelastic strain, are two key factors. An element layer of $10\mu\text{m}$ thickness at the indium solder interface was recommended in [0,0] and is being used as a standard criterion to average the inelastic strain or strain energy density to be used in fatigue models. The VonMises inelastic strain are averaged over 10 % of the area near the worst stress concentration over this $10\mu\text{m}$ element layer in the critical solder joint section as shown Figure 45.

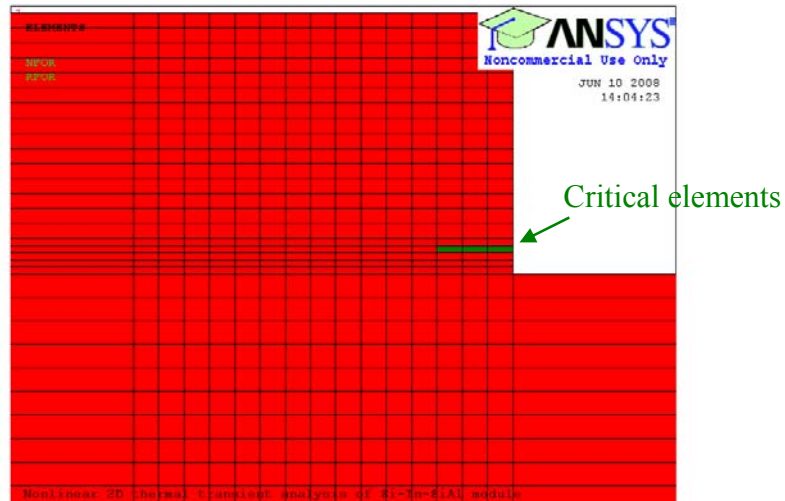


Figure 45 Critical elements used to obtain averaged inelastic strain.

Homogeneous properties were assumed for all packaging materials. Elastic properties were assigned to the Si die, Si₃N₄ substrate and AlSi housing. Elastic and viscoplastic properties were assigned to the indium attachment based on the test data as well as other published references. Some of these references indicate that indium properties are strongly temperature-time dependent, and nonlinear curve-fitting was applied based on available experimental data to determine the material properties at various temperatures (See Table. 10, Table. 11, Table. 12, and Table. 13).

Table. 10 Elastic properties of silicon

Temperature (K)	RT	RT
Young's Modulus (GPa) [0]	179	Silicon<100> single crystal, undoped.
Poisson's Ratio [0]	0.22	
CTE (ppm/°C)	3.0	
Thermal Conductivity(W/K.m)	148	

Note: material properties of bulk silicon were used.

Table. 11 Elastic properties of silicon nitride [0]

Temperature (K)	RT
Young's Modulus (GPa)	314
Poisson's Ratio	0.3

CTE (ppm/°C)	3.2
Thermal Conductivity (W/K.m)	70

Table. 12 Elastic properties of AlSi housing [0]

Temperature (K)	75	140	205	270	335	400
Young's Modulus (GPa)	121.4					
Poisson's Ratio	0.25					
CTE (ppm/°C)	10.08	8.03	7.81	8.67	10.00	11.35
Thermal conductivity (W/K.m)	196.50	180.24	165.57	152.49	140.99	131.07

Table. 13 Material properties of indium

Temperature(K)	75	140	205	270	335	400
Poisson's Ratio	0.3					
Young's Modulus (GPa) [0,0]	19.11	17.00	14.89	12.78	10.66	8.55
CTE (ppm/°C) [0,0]	23.9	26.9	28.27	30.46	32.65	34.83
Thermal Conductivity (W/K.m) [0]	99.83	94.37	89.03	83.82	78.74	73.78

After the materials properties were incorporated into the FEM model, thermo-mechanical analysis of packages with different sizes and material combinations were all performed in ANSYS. One Si /In /AlSi package is discussed in detail here as an example, where the indium solder joint is sandwiched between the Si substrate and AlSi housing, as shown in Figure 35.

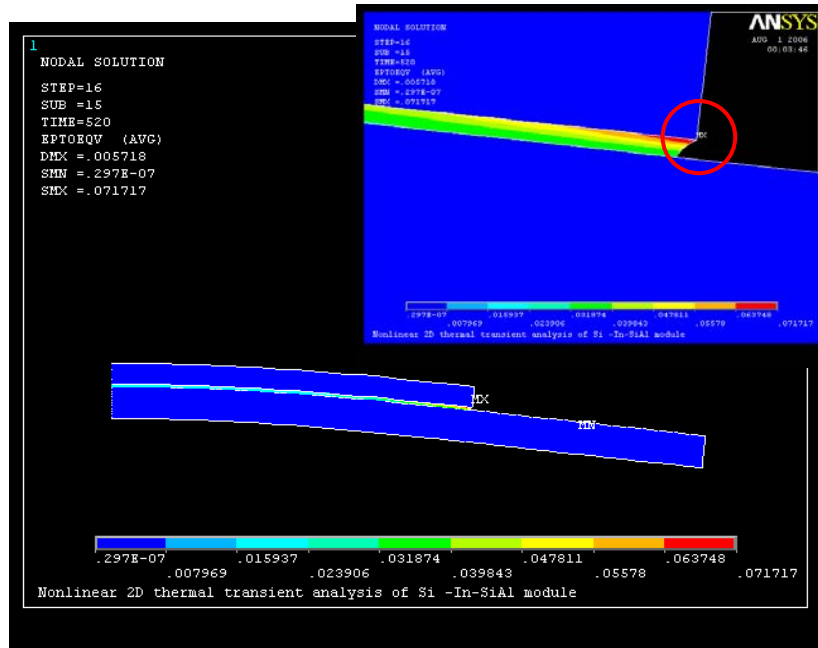


Figure 46 Contour plot of VonMises inelastic strain after 4 cycles of thermal shocking.

Figure 46 shows the contour plot of simulated VonMises inelastic strain in the whole package after 4 cycles of thermal shock. The results indicate that the outer upper corner near the Si/solder interface is the place with the highest localized strain concentration and is a likely failure initiation site. Thermal shock testing and cross sectioning revealed cracks at this site.

The prediction of the thermal fatigue life of the indium attach is based on the estimation of failure indicators such as the cyclic inelastic strain range in the Coffin-Manson empirical equation and strain energy density per cycle in energy-based fatigue models. These indicators can be obtained from the hysteresis loops. VonMises inelastic strain obtained from the 3 critical elements as shown in Figure 45 was plotted in Figure 47.

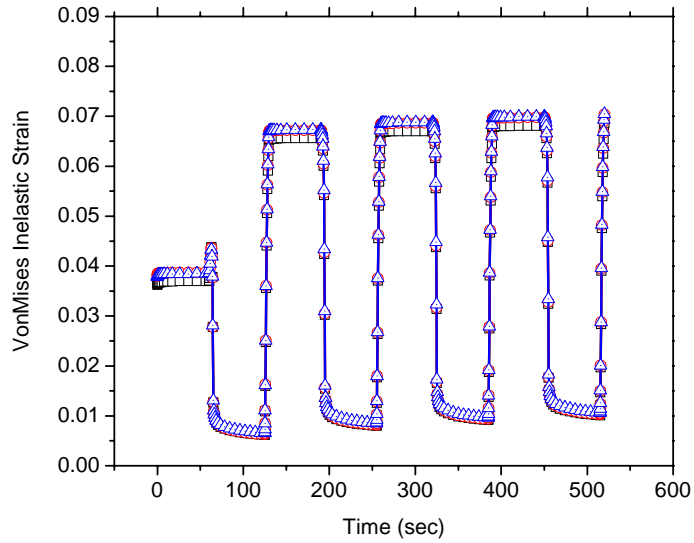


Figure 47 Cyclic VonMises inelastic strain of 3 critical elements at the edge corner of the solder joint.

The area averaged cyclic stress/strain curve and hysteresis loop of the critical elements at the outer corner in the indium solder joint is shown in Figure 48 and Figure 49. It is seen that the hysteresis loops follow the same cyclic pattern and converge very well after four whole cycles.

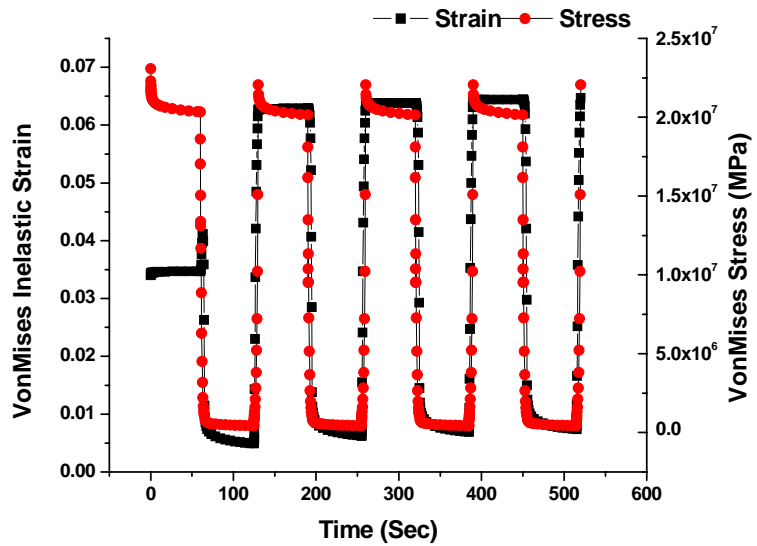


Figure 48 Cyclic stress/strain curves in solder joint after thermal shocking.

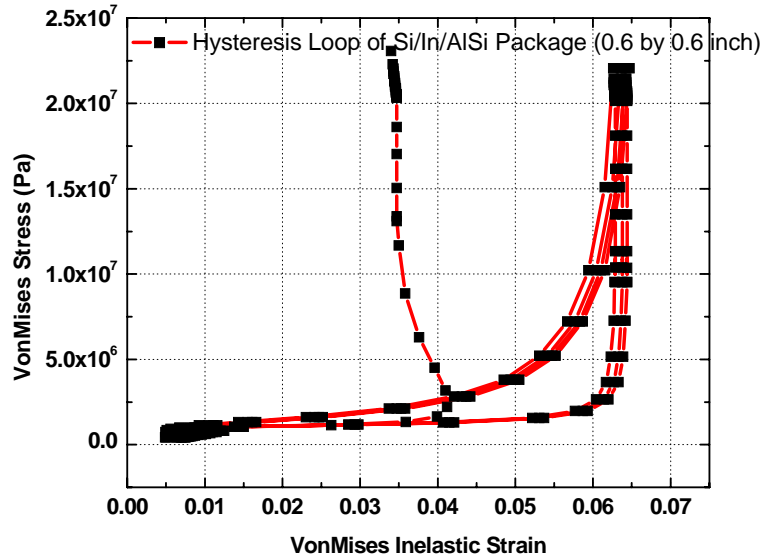


Figure 49 Stress-strain hysteresis loops at outer corner in solder joint after thermal shocking

4.8.2 Sensitivity Study

Sensitivity studies were performed to find the effect of critical design parameters on the thermo-mechanical behavior of the indium solder joint. The indium was used to attach silicon die to a silicon nitride substrate and silicon nitride substrates to an aluminum-silicon alloy housing (Figure 50). These materials were modeled as isotropic elastic with limited temperature dependency.

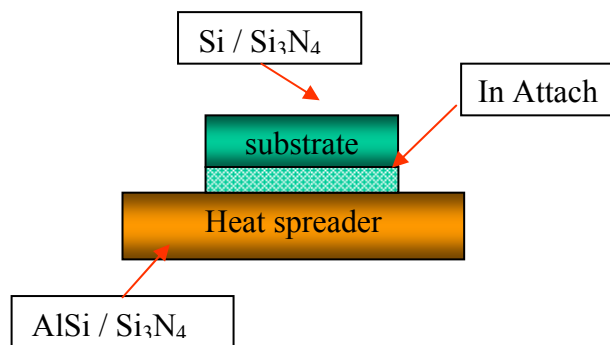


Figure 50. Schematic of simplified package model

In each material combination, three packages with various substrate sizes were

modeled in ANSYS as well as tested under thermal shock. After running thermo-mechanical analysis, two conclusions have been drawn, which are consistent with what can be derived from the simplified classic analytical models.

First, the amplitude of the inelastic strain in the indium attachment layer for the different packages with the same substrate dimensions follows the order, Si/In/AlSi > Si₃N₄/In/AlSi > Si/In/Si₃N₄. Moreover, indium attach in the Si/Si₃N₄ packages has a much smaller strain amplitude (about 0.018) than those in Si₃N₄/AlSi and Si/AlSi packages (0.06~0.082), which can be explained by the almost negligible CTE mismatch between Si and Si₃N₄ and results in longer thermal-fatigue life of Si/Si₃N₄ packages (Figure 51). Furthermore, the difference of strain amplitude in indium attach for the different packages increases with package size. In other words, the strain amplitude difference of indium attachment in larger die packages is bigger among different material packages.

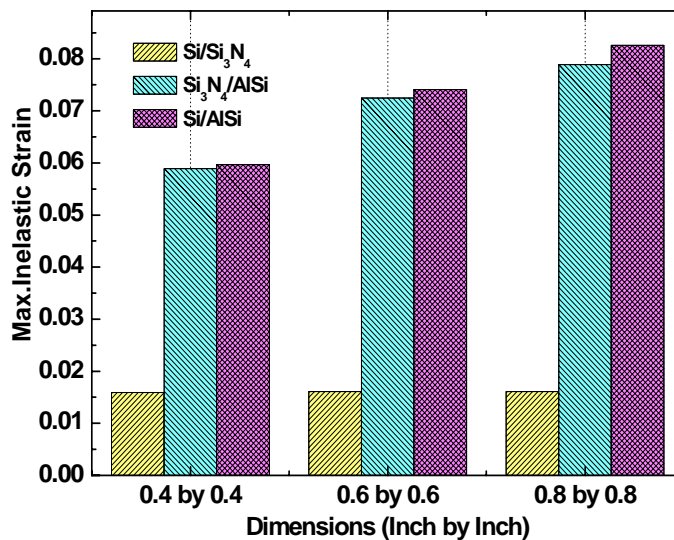


Figure 51 Max. inelastic strain at the outer corner of the package in indium after thermal loading

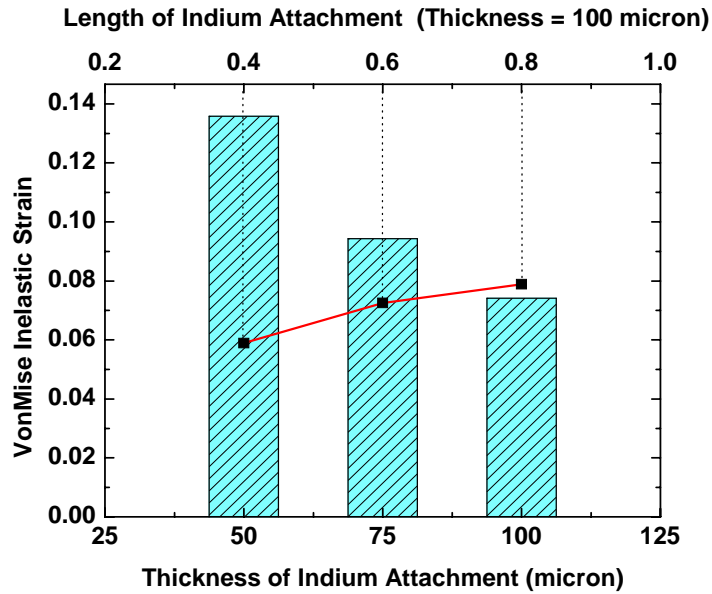


Figure 52 Inelastic strain as the function of indium solder thickness and package sizes: strain is more sensitive to solder thickness.

Second, inelastic strain in the indium solder joint is highly sensitive to its thickness rather than its length, as shown in Figure 52. This can also be proved from the analytical models, such as the C. Nelson [0] and Suhir [27] models.

4.9 Discussion and Conclusion

The FEM simulation results indicate that the outer upper corner near the Si/Indium interface is the place with the highest localized strain concentration and is the likely failure initiation site. The accelerated thermal shock test and cross sectioning have revealed cracks at this site, which means the computational modeling accurately simulated the actual package fatigue deformation behavior.

Assumptions have been made in FEM simulation, such as homogenous material properties, and some effects have not been considered in the simulation, such as

manufacturing process defects and microstructure effects. However, these factors are significant to the deformation behavior and damage of the package in some cases. They are discussed in the following sections.

4.10 Fatigue Life Prediction

The fatigue life of conventional solder joints has long been related to the induced cyclic shear strain via the Coffin-Manson relation. The inelastic VonMises strain is used as a replacement here to account for the 3D multi-axial loading effect. The cyclic VonMises inelastic strain range vs.the number of cycles-to-failure is plotted in the following figure. Curve-fitting is adopted to obtain the value of fatigue coefficients c and $2\varepsilon_f$. The form of the relation used in the present analysis is

$$N_f = \frac{1}{2} \left(\frac{\Delta\gamma}{2\varepsilon_f} \right)^{\frac{1}{c}}$$

where N_f = median cycle to failure; c = fatigue ductility exponent; $2\varepsilon_f$ = fatigue ductility coefficient; $\Delta\gamma$ = total average cyclic VonMises inelastic strain range.

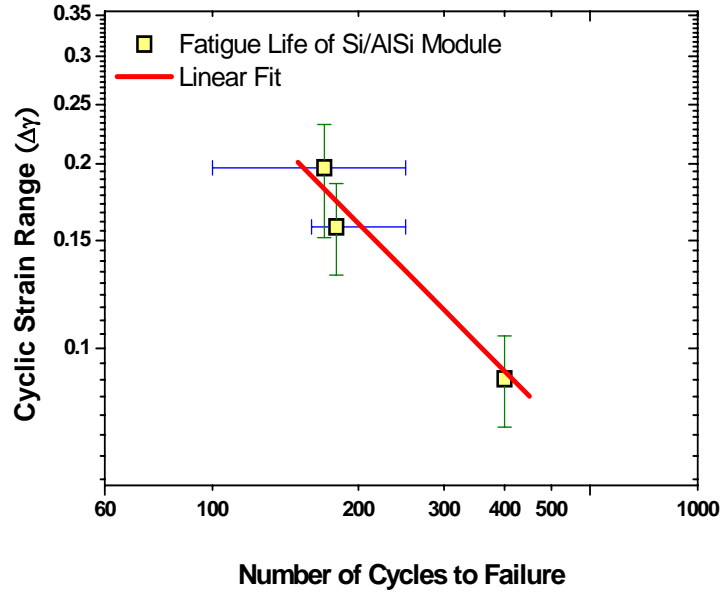


Figure 53. Curve fitting for Coffin-Manson empirical model

The Coffin-Manson model for indium thermal fatigue based on the data collected for a Si/In/AlSi package in the thermal shock test is as follows:

$$N_f = \left(\frac{\Delta\gamma}{11.18} \right)^{\frac{1}{0.8016}}$$

With the calibration of this thermal fatigue model for indium attach, FEM modeling of newly designed structures, even with different packaging materials, was conducted to provide a guideline for the second- and third-generation package design. Level 1 (die-to-substrate) and Level 2 (substrate-to-package) packaging structures were designed and developed in the present work. Three types of interconnection technology were adopted for Level 1 packaging, including die attach (In), flip chip solder bump (In50Pb) and wire bond (Au) to interconnect the die to different base substrate materials, as shown in the following schematics (Figure 54 and Figure 56). For the substrate-to-package joint, an indium preform was used for substrate attachment.

(1) Die-to-Substrate:

A. Die Attach (In)

Indium die attach (0.05 mm thick) was used to join a 5 mm x 5 mm die onto an AlN substrate (48mm x 13.5mm) coated with multilayer Cu/polyimide (3 um/6 um). The AlN substrate was then bonded to an Al₂O₃ package (53mm x 14.5mm) by the same 0.05 mm thick indium foil, as shown in Figure 51.

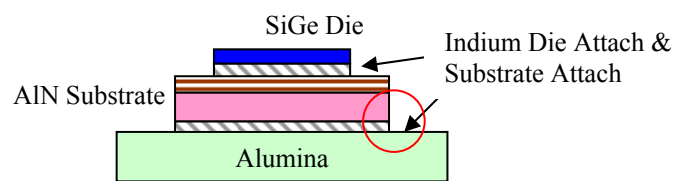


Figure 54. Schematic of die attach and substrate.

A half diagonal finite element model of the die/die attach/Cu-polyimide/substrate/substrate attach/package with the actual package size was built up, as shown in Figure 55. Thermomechanical transient analysis was utilized to simulate temperature and stress/strain distribution in the package.

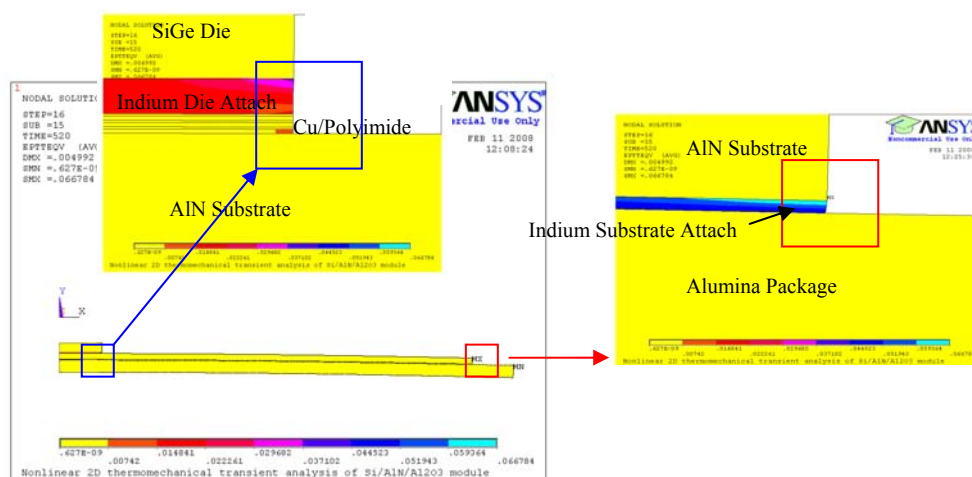


Figure 55. Contour plot of VonMises inelastic strain distribution in the whole die attach type package.

From simulation results, it was found that the maximum inelastic stress/strain occurred at the far corner of the substrate in the substrate to package housing layer attachment since Si has a better global CTE match to multilayer Cu/polyimide and AlN than AlN has to Al₂O₃ substrate. Therefore, substrate-to-package interconnection is the main concern in reliability. The inelastic strain at the critical site was utilized to predict the fatigue life under lunar thermal fatigue conditions, and the results will be discussed in section (2) below.

B. Flip-Chip Solder Bump

The structure of the flip-chip package is the same as the die attach package except the solder bump (In50Pb) was used to replace the die attach (In). Si and Si₃N₄ CTE match the Si (SiGe) die and were used as the base substrate for flip-chip assemblies (Figure 56).

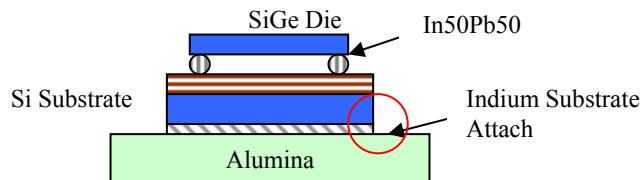


Figure 56. Schematic of flip chip solder bump and substrate

Since the CTE mismatch between die and base substrate, Si or Si₃N₄, under temperature cycling is almost negligible in this kind of structure, the maximum stress would be concentrated again at the substrate to package interconnection. Moreover, this construction has the largest CTE mismatch for the base substrate (Si) and the package (Al₂O₃) as compared to the AlN substrate and Al₂O₃ package (Figure 57).

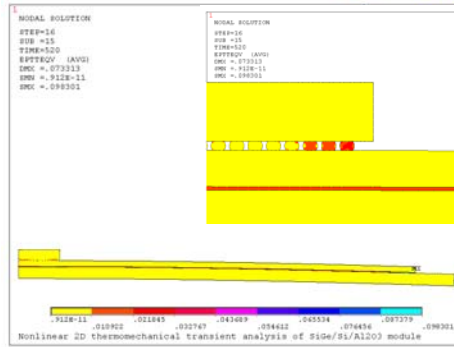


Figure 57. Contour plot of VonMises inelastic strain distribution in the whole flip-chip type package

(2) Substrate-to-Package

As discussed in the previous section, the substrate attach undergoes higher stress than all die interconnections during temperature cycling. The substrate attach would therefore be the dominant failure site and the one of most concern in packaging reliability.

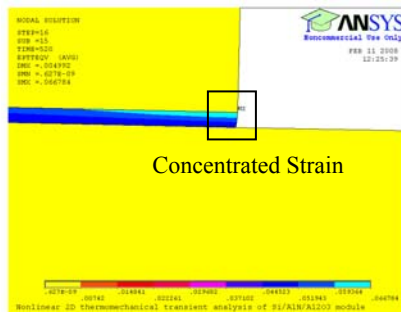


Figure 58. FEM model of substrate to package

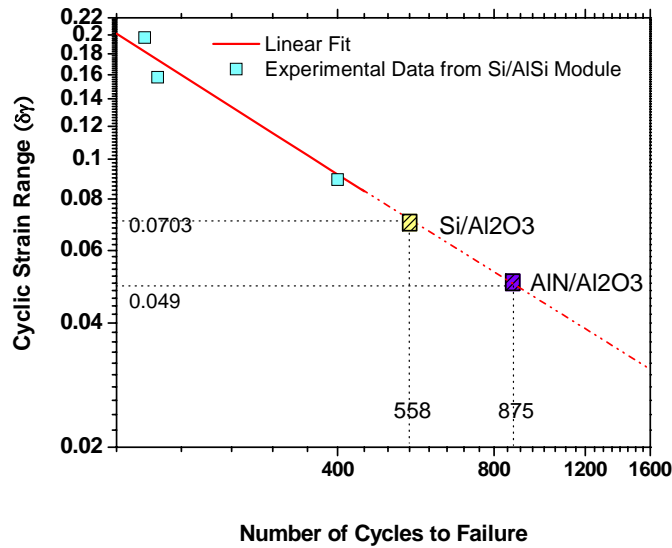


Figure 59. Predicted fatigue life of new designed electronic module based on the Coffin-Manson fatigue model

The FEM modeling of different substrate materials was conducted (Figure 58). The strain is concentrated at the outer-upper corner of the indium substrate attach between the AlN/Si substrate and the alumina housing. The inelastic VonMises strain was used as the replacement of shear strain to account for the 3D multi-axial loading effect. Then, fatigue life was predicted based on the calibrated empirical Coffin-Manson model, as shown in Figure 59 with notation of AlN/Al₂O₃ or Si/Al₂O₃. The predicted life for both substrates exceeds the design life requirement (13 lunar cycles per year x 10 years x 3x safety factor = 390 cycles) and would be safe.

Chapter 5 Isothermal Fatigue of Indium Solder Joint at Extended Cold Temperature

5.1 Evaluation of Solder Joint Fatigue at Subzero Temperatures

Electronic modules for lunar exploration and colonization as well as for other cryogenic applications are required to operate reliably across a wide temperature range including extended dwells at very low temperatures ($T < -55^{\circ}\text{C}$). In addition to the thermal fatigue resulting from daily temperature cycles, as discussed in the previous chapter, the electronic module is also subjected to isothermal mechanical fatigue. For example, a module to be used for lunar sensing and actuation may undergo mechanical cyclic loading, including shock and vibration loading, when moving around on the surface of the moon to acquire scientific data. Cyclic bending fatigue was conducted as an effective evaluation method for mechanical damage since it provides a simpler and easier loading profile than vibrational loading, but still enables an accurate investigation of the effect of the factors resulting in mechanical fatigue failure.

Previous studies have revealed that the indium attach layer is one of the dominant sites for fatigue failure [0,0]. In order to evaluate the fatigue performance of chip on board (first level) and substrate on package (second level) interconnections and improve the reliability of the complete electronic system, isothermal fatigue of indium solder joint must be considered. In fact, the isothermal fatigue at extended cold temperature during the lunar night can be even more of a concern than thermal fatigue, if the indium solder interacts with gold coatings on the substrate and die to produce brittle intermetallics

prone to cracking under mechanical stress at cryogenic temperatures.

The formation of intermetallics at the interface between the substrate or die and the attach layer improve adhesion and bonding, and small, well distributed intermetallic particles strengthen the bulk attach. However, as the intermetallic reaction continues, it can lead to the formation of thick, voided, brittle intermetallic layers at the interface between the substrate or die and the attach material that can weaken the bond by serving as initiation sites for cracking. The lower is the temperature, the more the bond is prone to fail by intermetallic cracking. Moreover, intermetallic compound is not only formed during the initial bonding of the interconnection, but continues during operation of the device. This additional intermetallic formation is dependent both on the initial metallization layer thickness and the operating temperature. For example, intermetallics at the interface between the attach and the die or substrate can grow during the lunar day because of the elevated temperature (125°C). Therefore, the growth of excessive intermetallics in the lunar day could accelerate and lead to brittle failure at the attach interfaces under isothermal fatigue conditions during the lunar night.

Little data has been reported on the isothermal mechanical fatigue properties of indium attaches at cold temperatures. In this study, an isothermal three-point bending fatigue test was designed and conducted to evaluate the cold temperature mechanical fatigue performance of indium attach as well as to identify the fatigue deformation mechanism(s) at extended cold temperatures, where diffusion controlled mechanisms such as creep, which occur at higher temperatures (i.e. above $0.5T_m$), do not dominate. The goal of this work is to establish the following:

- 1) The relationship between intermetallic growth and aging time for various initial Au metallization thicknesses.
- 2) The relationship of intermetallic thickness and solder joint reliability.
- 3) The influence of temperature and fatigue loading frequency on solder joint reliability at cold temperature for different amounts of Au-In intermetallics.
- 4) A fatigue life model based on a fundamental understanding of the failure modes, mechanism and microstructures.

In this chapter, the steps in achieving these goals will be detailed. First, the thermal aging test was conducted to obtain the relationship between intermetallic growth and aging time @ 125°C, which was used as the reference for intermetallic thickness later in cold temperature fatigue test. Then the mechanical reliability was evaluated through low cycle, three-point bend fatigue tests at -150°C and -55°C and examined with respect to the amount and microstructure of intermetallics before and after thermal aging. The amount of intermetallic compound in the bond was controlled by (1) the growth at different thermal aging time and (2) the initial Au metallization layer thickness for a fixed indium thickness. Lastly, fractography was performed on each failed specimen to assess the effect of intermetallics on the fatigue crack initiation sites, propagation mechanisms, and fatigue life.

5.2 Identification of Intermetallic Phases @ In-Au Interfaces

The freshly bonded specimens were metallographically analyzed to examine the microstructure of the joint, especially the intermetallic phases at the bond line interfaces. The standard procedures for metallographic preparation are specimen sectioning,

mounting, grinding and polishing, chemical etching, microscope examination, and measurement/image analysis. An optical microscope and scanning electron microscope (SEM) by Oxford were employed to observe the microstructure of Au-In intermetallic phases. During the specimen inspection by SEM, energy dispersive x-ray spectrometry (EDX) was also carried out to identify the chemical compositions of the intermetallic compounds.

Seven intermediate phases have been reported in the Au-In system (viz. AuIn_2 , AuIn , Au_7In_3 , Au_3In and Au_4In [0]. However, AuIn_2 was the only intermetallic observed in the reaction zone in this work, and it plays the dominant role in the fatigue failure of the indium joint. It is also the phase that forms first in the reaction and is the stable phase for indium rich systems. The following picture shows AuIn_2 intermetallic compound at the interface of the indium joint after chemical etching. AuIn_2 compound has two very different types of grain: bigger grains with rough morphology at reaction interface of indium solder, and fine condensed grains with relative uniform distribution in the interfacial intermetallic layer.

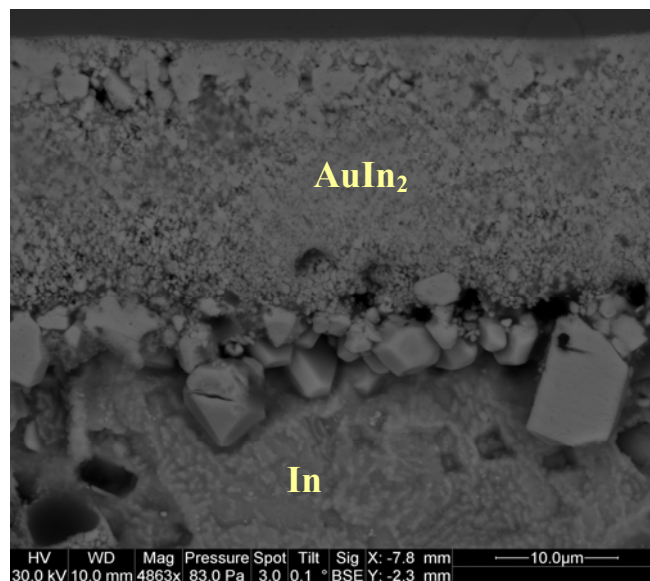


Figure 60 Intermetallics at indium solder joint interface.

The formation of AuIn_2 grains with two different sizes and shapes can be attributed to both the thermal gradients inside the solder joint during reflow bonding and the interdiffusion from the indium solder to the Au coating interface. Initially, AuIn_2 intermetallics were formed by the reflow bonding process. The rapid dissolution of Au into the liquid indium solder followed by cooling forms an irregular structure of interfacial intermetallics. During this process, the attach interfaces, being closer to the surface, undergo a faster cooling rate than is present deeper in the indium attach, resulting in the smaller grain size close to the interface and larger grain size in the interior. . Furthermore, this intermetallic layer was rough and scalloped.

As Au and In continue to diffuse and react during thermal aging, after solidification of the joint, more intermetallic will be formed near the interfaces. The study of Au-In thin film reactions by previous researchers [0] showed that the AuIn_2 was formed by In atoms diffusing through the preformed intermetallic layer to react with Au atoms, and from a kinetic point of view, the parabolic law was obeyed, as the existing layer will act as a diffusion barrier. This further growth at the interface creates small intermetallic grains,.

5.3 Intermetallics Growth under Thermal Aging @ 125°C

The growth of intermetallics is known to be a function of time and temperature. The aging temperature 125°C was selected because it is the environmental temperature on the surface of the moon during the lunar day. It should be noted that the aging temperature 125°C is one of the standard high temperatures in both JEDEC and MIL-STD standards (i.e. MIL-STD-750C).

The thermal aging test was designed to study the growth of intermetallic at the indium to die or substrate interface during the lunar day for different representative initial Au metallization thicknesses. Specimens with Au coatings of 0.5 μm , 1 μm and 3 μm were characterized after 1,3,5,7, 24, 48, 100 and 144 hours of aging at 125°C.

The microstructural evolution during thermal aging was studied under SEM after mounting, cross sectioning, and etching the specimen. Consistent with the observations from previous researchers, intermetallic decomposition, phase and shape change are not observed in thermal aging. The intermetallics grow gradually as aging time increased. The enlargement of the initial voids and an increase in the number of the voids as aging time increased were observed as shown in Figure 61, indicate the formation of voids with intermetallic growth that could accelerate failure. The evolution and growth of intermetallic stabilized after 48 hours.

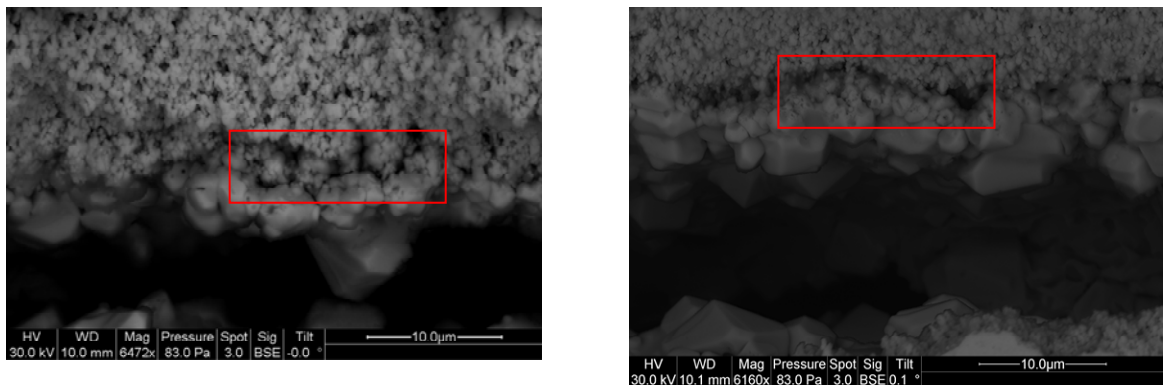


Figure 61 Voids enlargement after thermal aging: (a) before aging; (b) after aging.

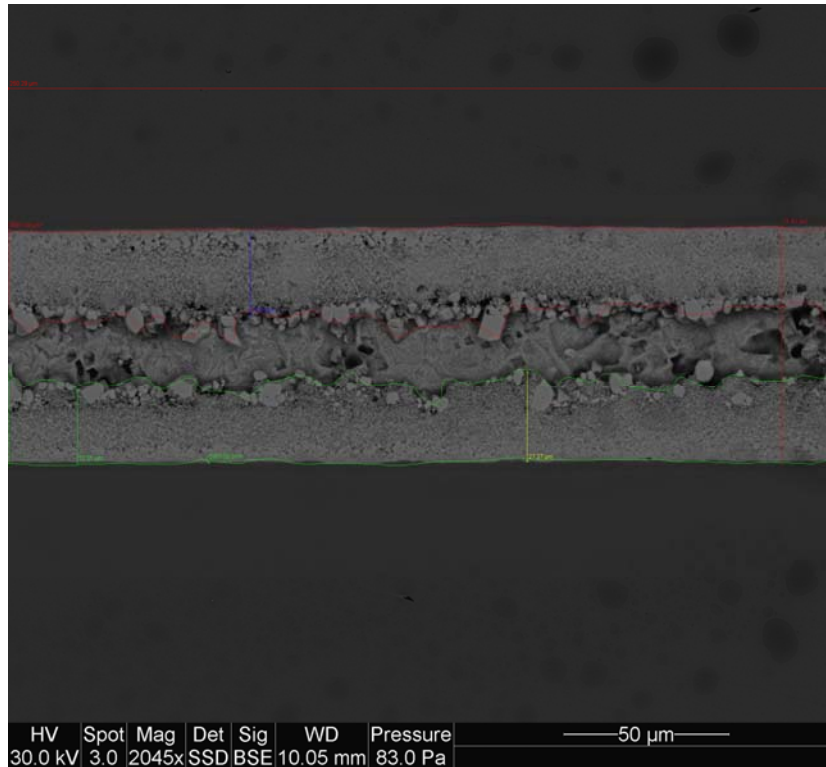


Figure 62 Measurement of IMC thickness.

The thicknesses of AuIn_2 intermetallics after thermal aging were then measured. The maximum, minimum, and area weighted average values were measured, as in the sample with $3 \mu\text{m}$ initial Au thickness shown in Figure 62 as an example. At least 16 measurements have been done for each case. Data were analyzed statistically and shown to follow a normal distribution. So the normal mean was used as the characteristic thickness value. Figure 63 shows how the thickness of intermetallic was obtained statistically with a $3 \mu\text{m}$ initial Au metallization sample as an example.

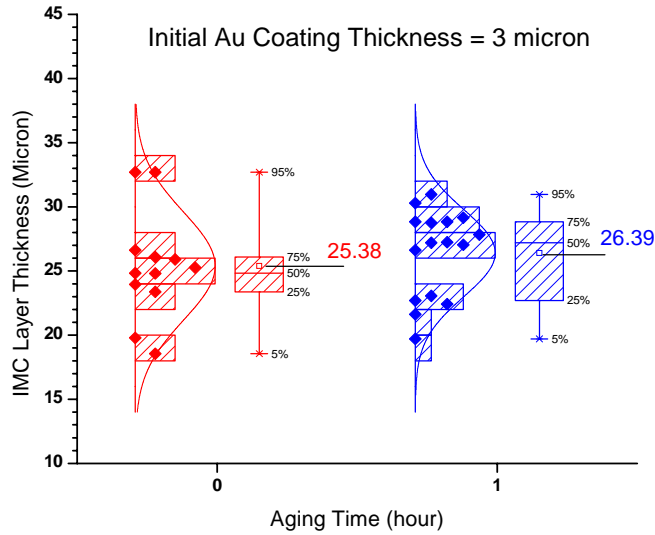


Figure 63 Mean values of measured IMC thickness by fitting to normal distribution.

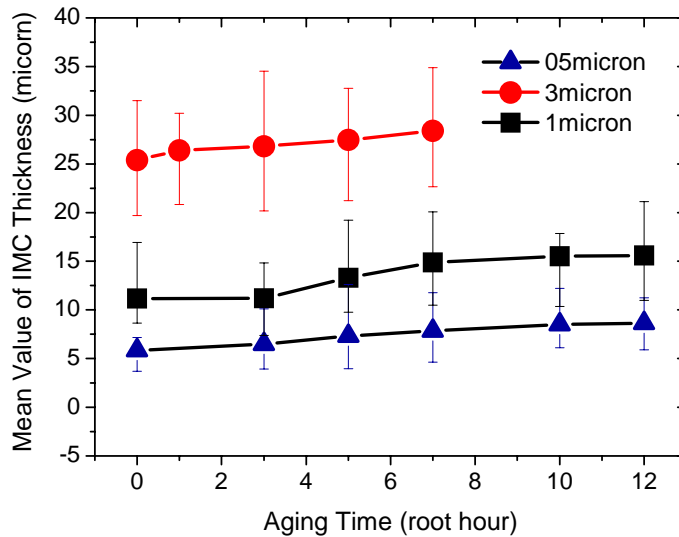


Figure 64 IMC growth with aging time with respect to different initial Au metallization thickness.

The intermetallic thickness as a function of time with respect to various initial Au metallization layer thicknesses is shown in Figure 64. The intermetallics grew very fast for the 3 um initial Au layer and consumed all indium solder joint after 48 hours aging. For Au metallization with initial thicknesses of 0.5 um and 1 um, the growth is slower and was saturated before all the indium was consumed. The thermal aging resulted in

voids growth and enlargement after the saturation has been achieved. These findings on the growth of intermetallics were crucial in understanding the effect of thermal aging on fatigue failure of the solder joint at cold temperature which was also studied in the present work and will be addressed in detail in the next sections.

5.4 Fatigue Bending Test at Cold Temperature

5.4.1 Design of Experiment (DOE)

The fatigue tests were designed to study the effect of the following four factors on the fatigue life of bonded indium samples at cold temperatures: temperature, aging time, loading frequency and intermetallics content. Effects of all those factors were studied at -150°C as the baseline since the cold temperature -150°C is the normally required low operational temperature for the most space exploration missions on Moon and Mars.

The effect of thermal aging on intermetallics growth, and its subsequent effect on the indium attach joint fatigue life, was studied since the device is exposed to thermal aging at 125°C for one lunar day, which lasts for 14 earth days, within each temperature cycle during its mission on the Moon. It was discovered that the evolution and growth of Au-In intermetallics stabilized after 48 hours (for details see previous section). After the study of this effect, all samples used in our test to investigate the effect of other factors were thermally aged. The effect of low temperature on indium attach reliability was studied at -55°C for military use and -150°C for space exploration for a number of different intermetallic layer thicknesses. The loading frequency effect was studied at three levels (low, medium and high) all at -150°C. The test matrix is shown in the following figure.

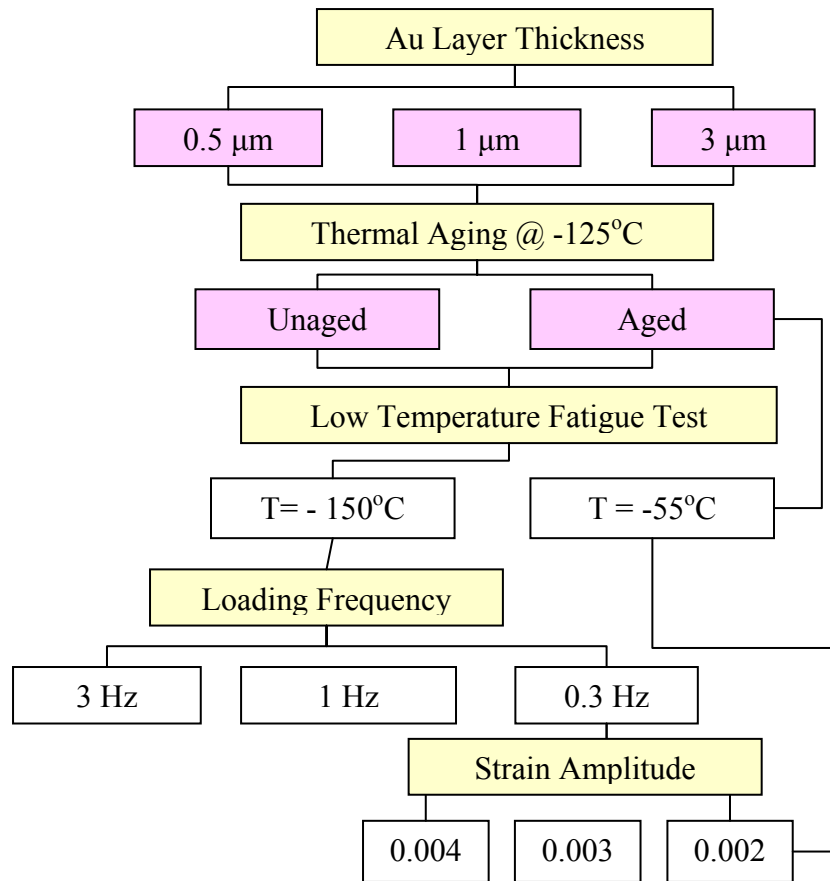


Figure 65 Flow chart of low cycle fatigue test at low temperatures

5.4.2 Specimen Preparation

5.4.2.1 Sample Details

A drawing of the specimen for the fatigue bending test is shown in Figure 66. Copper strips were used for both the base and as dummy components so as to eliminate the confounding effects of any thermal expansion mismatch stresses on the results. The strips were electroplated with Au over Ni at various thicknesses ranging from 0.5 μm to 3 μm . The copper strip size was designed to 45 mm by 6 mm, with a thickness of 0.5mm due to the limits of the instrument. Dummy component strips of size 6 mm by 6 mm and a

thickness of 0.5 mm were attached at the center of the copper strips. The component and base strips were bonded by indium foil of thickness 50 μ m, as shown in Figure 66. The detailed bonding process is presented in the following section.

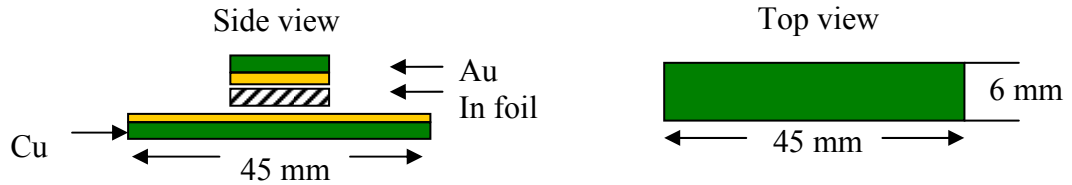


Figure 66 schematic of bonded samples for isothermal fatigue test at cold temperatures.

5.4.2.2 Sample Soldering

Component strips were assembled on the copper strip base by means of infrared reflow using indium foil with Indalloy Flux (#5 RMA) as shown schematically above, and the fabrication process was as follows:

1) Presoldering Clean:

The gold coated copper strip base and component were cleaned by rinsing in the following series of solutions and solvents to remove the tarnish on their surfaces: (a) ultrasonically degreased in acetone, (b) rinsed in methanol, and (c) blown dry in nitrogen gas.

The 99.99% indium with 50 μ m thickness was cut to the same size as the Au-deposited Cu component strip. Then it was cleaned with the following series of solutions and solvents: (a) ultrasonically degreased in acetone, (b) soak into 10% HCl for 1min (This will remove the 8-10 nm of oxide that forms on the surface because indium is self-passivating. The oxide, once removed, will quickly reform

to a thickness of 3-4 nm, and, after a few days, the indium oxide thickness will be back to 8-10 nm; (c) flushed in DI water twice; (d) rinsed again in acetone; (e) rinsed in methyl alcohol and (f) blown dry in nitrogen.

2) Reflow Soldering

After cleaning, indium foil was dipped into RMA flux and inserted between two Au-deposited copper parts. The sandwiched sample was heated in an IR furnace in the air. Care was taken to keep the sample aligned properly. The furnace temperature was raised to 200°C within 10min and then cooled down to room temperature in 5 min by forced air convection. The time-resolved temperature profile on the sample surface during reflow was monitored by a thermal profiler as shown in Figure 67.

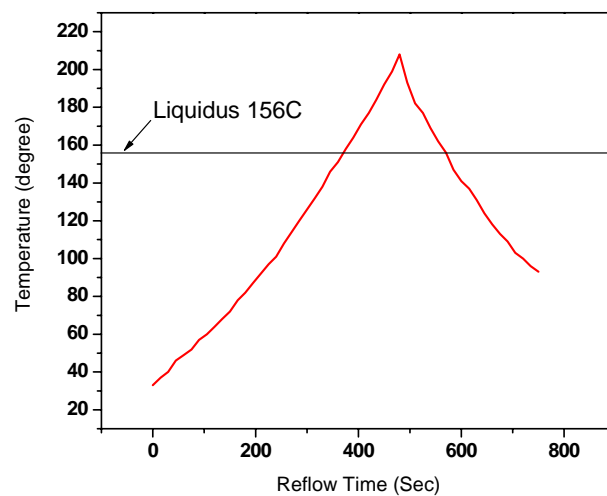


Figure 67 Measured temperature profile under reflow soldering.

3) Mechanically remove excess indium around edges. Store at room temperature for 5-15 days to allow for nearly complete residual stress relaxation before testing.

- 4) The two side surfaces along the bond line of the specimen were polished smooth right before the fatigue test in order to have a clear view of the bond line and to permit measurement of the fatigue crack growth during test. SiC paper (600grit) was used since it results in a satisfactory polished surface under the microscope. Finer grit SiC papers and alumina powder left small particles embedded in the indium solder joint because of its softness, which would affect the fatigue behavior of the solder joint.

5.4.2.3 Sample Quality Examination

All fresh bonded specimens underwent X-ray and Scanning Acoustic Microscope (SAM) imaging to examine the bond quality. The void percentage by area was measured by the image process software, ImageJ. The bond quality control was conducted according to IPC785. Then some samples were randomly selected, mounted into epoxy and cross sectioned to check the interior bonding surfaces of the specimen.

5.4.3 Test setup and Experimental Procedure

The three point bend fatigue tests were conducted at two temperatures (-150°C and -55°C) to study the effect of aging, loading frequency, intermetallics content and fatigue temperature on the fatigue life of samples. The fatigue failure sites and modes were identified and the relationship of fatigue life with temperature, strain amplitude, strain rate and intermetallics content documented. The experiment basically includes the following procedures:

Step 1: Selecting sample dimensions using sample testing limits.

The suggested sample dimensions were in the recommended range for sample geometry based on the limitations of the size of the test fixture. The tested sample is a rectangular bonded strip 45mm in length and 6mm in width.

Step 2: Sample Loading.

Figure 68 shows the fixture with the sample loaded. To load a sample, perform the following:

1. Slide the sample onto the lower fulcrums.
2. Adjust the stage position to bring the fulcrum to the sample. Generate a very small (10 g) normal force.
3. Zero the gap. This provides a zero reference point throughout the test.
4. Ensure that the bearing overload warning is not displayed.

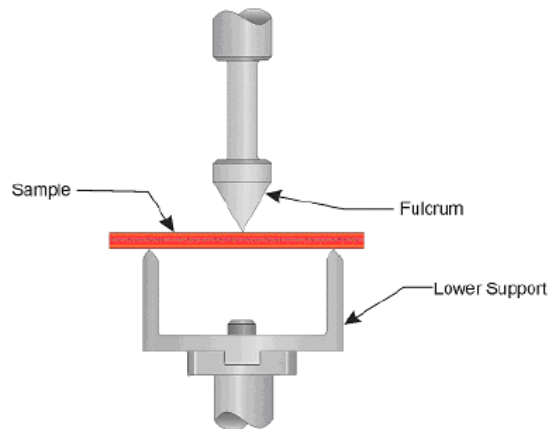


Figure 68 Three point bending tool with sample loaded referred to RSIII manual.

Step 3: Strain Controlled Transient Arbitrary Wave Test.

A series of cyclic bending tests, with the positive sine wave strain loading in Figure 69, were run at different initial stresses at two different ambient temperatures (-150 and -55°C). At -150°C, the specimens were tested under different strain amplitudes and loading frequencies. The occurrence and propagation of fatigue failure was recorded by taking optical microscope image every 100 cycles. The test was kept running until the specimen failed and the number of cycles of failure was recorded at the same time.

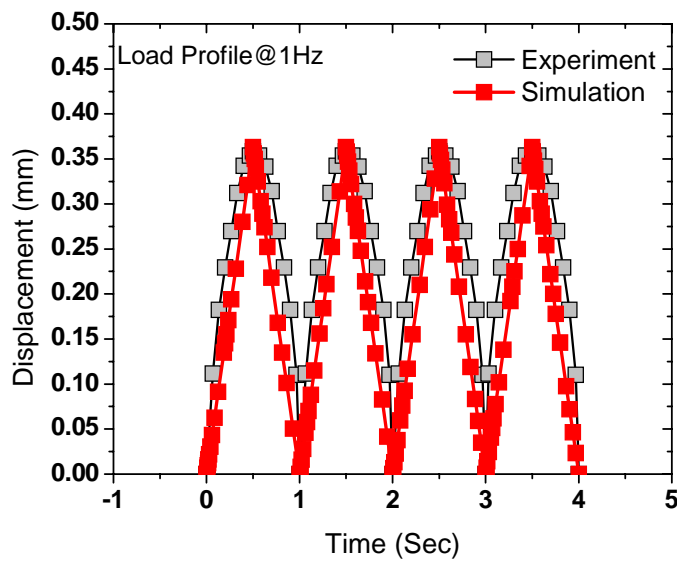


Figure 69 Schematic of positive sine wave of applied strain.

5.4.4 Experimental Results

5.4.4.1 Fatigue Crack Growth Measurement

For fatigue crack growth measurement, the bending fatigue test was conducted until the crack from one side reached the center line of the copper component strip. The modified dye-n-pry technique was used along with pretreating the side surface of the specimen to image the crack. The fatigue failure and crack growth in the specimen was recorded using

a metallographic microscope under 500X magnification. The colored paint was applied at the side edge of the component to help in the identification of the crack. It was reapplied every time the specimen was taken out for examination under the microscope.

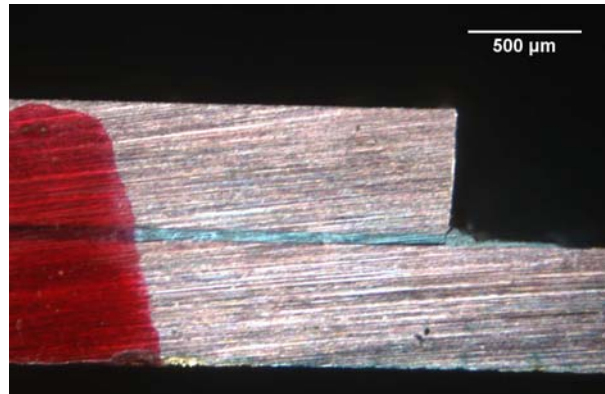


Figure 70 Fatigue crack at 1600 cycles in sample #20 with Au=3μm @ -150°C.

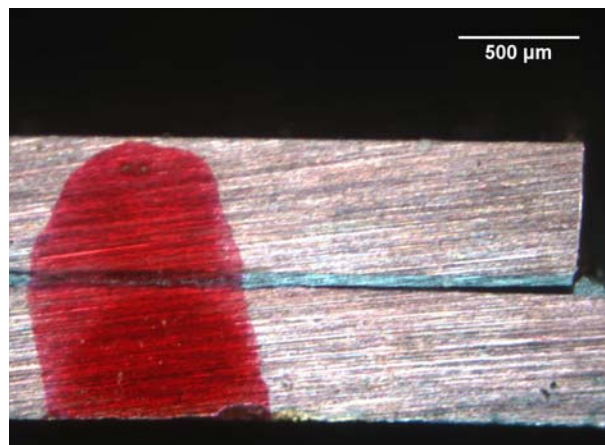


Figure 71 Fatigue crack at 2000 cycles in sample #20 with Au=3μm @ -150°C.

First, the fatigue crack growth per 100 cycles was measured using the image processing software, Image J, and the measurement was terminated when the crack reached the center line of the specimen. The measurement of crack growth in sample #20 with Au = 3μm fatigued at -150°C is shown as an example in Figure 70 and Figure 71. Representative crack growth data along with fatigue cycles is plotted in Figure 72. The

crack growth rate stays essentially constant during the fatigue test. It was observed that the crack growth rate is also constant during thermal fatigue cycling for eutectic PbSn solder [0].

The crack growth behavior was determined for each specimen by measuring the crack length and then curve fitting as shown for an example in Figure 72. It was shown that the crack growth obeys a linear relationship with R-square equal to 0.9937. Then the crack growth rate was determined by the slope of the fitted straight line as shown in Figure 72. The number of cycles to crack initiation can be determined by extrapolating the curve back to the x-axis (crack length = 0). It is seen that crack initiation accounts for about 25% of the fatigue life for these particular assemblies.

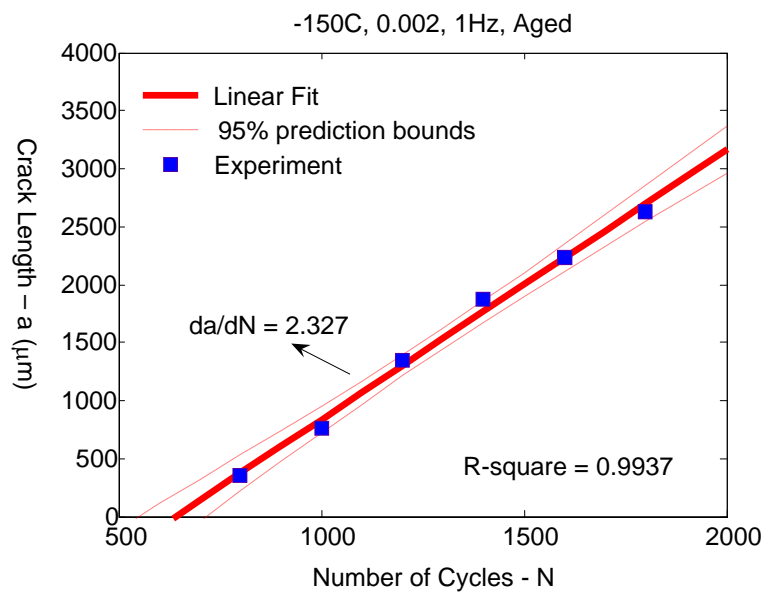


Figure 72 Typical crack growth measurement and determination.

Four replicates for each condition, for a total of 50 samples, have been tested and their crack growth measured. Mean value of crack initiation and crack growth rate from

replicates under each condition were used as the characteristic value. The crack growth rate of specimens with 0.5 μm initial Au coating under different loading temperature, strain amplitude, and loading frequency is listed in the following table.

Data Set	Temperature ($^{\circ}\text{C}$)	Load Frequency (Hz)	Strain Amplitude	Crack Growth ($\mu\text{m}/\text{cycle}$)
1	-150 (No aged)	0.3	0.002	2.088
2	-150	0.3	0.002	1.932
3	-150	1	0.002	1.755
4	-150	3	0.002	1.785
5	-150	0.3	0.004	5.42
6	-150	0.3	0.003	3.27
7	-55	0.3	0.002	0.665

Table. 14 Measured crack growth data under different loading conditions.

5.4.4.2 Fatigue Life Data

Fatigue life data were collected based on a definition that the sample is considered failed when the crack extends 50% of the total length of the component summed from both sides (Figure 73). In literature [0,0,0,0], failure was defined as a 20% to 50% drop in peak load and the cycle number at the load drop was regarded as the fatigue life time of the solder joint. It was shown that a 50% cracked area corresponds to a peak load drop of up to 25% in present work (Figure 74) by taking a specimen with 0.5 μm initial Au coating under a load frequency of 0.3Hz, and a strain amplitude of 0.002 at -150°C as an

example. This was proven by correlating the number of cycles to 50% cracked area to the load drop exhibited at that number of cycles.

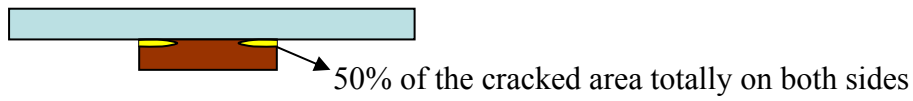


Figure 73 Schematic of failure criteria in specimen.

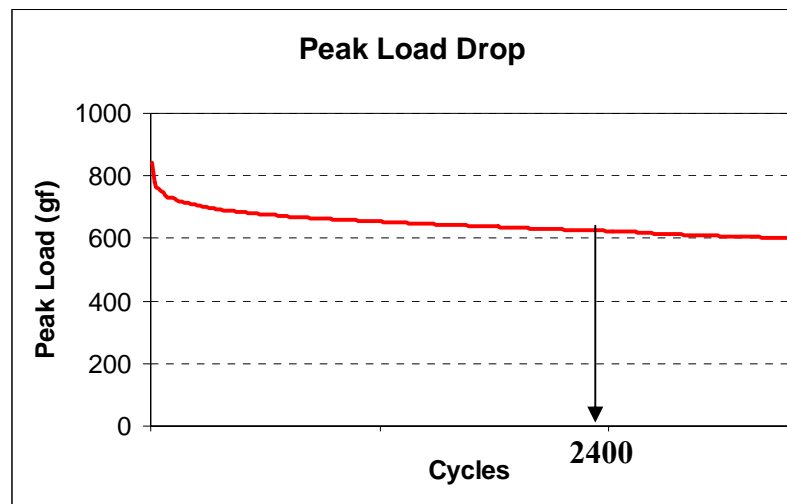


Figure 74 Corresponding peak load drop during fatigue test when crack area is 50%.

There were 4 replicates for each condition and over 50 specimens were tested in total. Then the fatigue data were input into the reliability software, Reliasoft ++6, to obtain the characteristic fatigue life of the samples at each condition. The collected fatigue data were considered left censored, and fitted to a 2P Weibull distribution to obtain the characteristic life. The following table shows the fatigue life for specimens with a 0.5 μ m thick Au coating under different test conditions, as an example.

Data Set	Temperature (°C)	Load Frequency (Hz)	Strain Amplitude	Crack Initiation (cycle)	Life (cycle)
----------	------------------	---------------------	------------------	--------------------------	--------------

1	-150 (Unaged)	0.3	0.002	1500	2416
2	-150	0.3	0.002	1900	2850
3	-150	1	0.002	1466	2934
4	-150	3	0.002	1300	3150
5	-150	0.3	0.004	150	600
6	-150	0.3	0.003	600	1000
7	-55	0.3	0.002	2900	6700

Table. 15 Measured fatigue life initiation and total life.

The standard parameters in 2P Weibull analysis are the Weibull Slope β , and the Characteristic Life η , which is the number of cycles required to cause failure of 63.2% of the samples from a particular test matrix. If the same bending fatigue failure mechanism happened in the specimens under different testing conditions, Weibull slopes should have the same values. However, Figure 75 and Table. 16 show various values of the Weibull slope which correspond to different failure modes. The Weibull slope for samples with 3 μm thick initial Au coating which failed in the purely interfacial brittle stage differs from that for samples with 0.5 or 1 μm thick initial Au coating that failed exhibiting mixed bulk-interfacial intermetallic modes in the strengthening stage. It has a higher slope, leading to quicker failure. These indications in the Weibull plot are consistent with what was observed from fatigue failure analysis and is able to be explained by the underlying dominant failure mechanism in these conditions. More discussion of these different

stages in fatigue life with respect to various thicknesses of intermetallics is provided in Section 5.5.2.

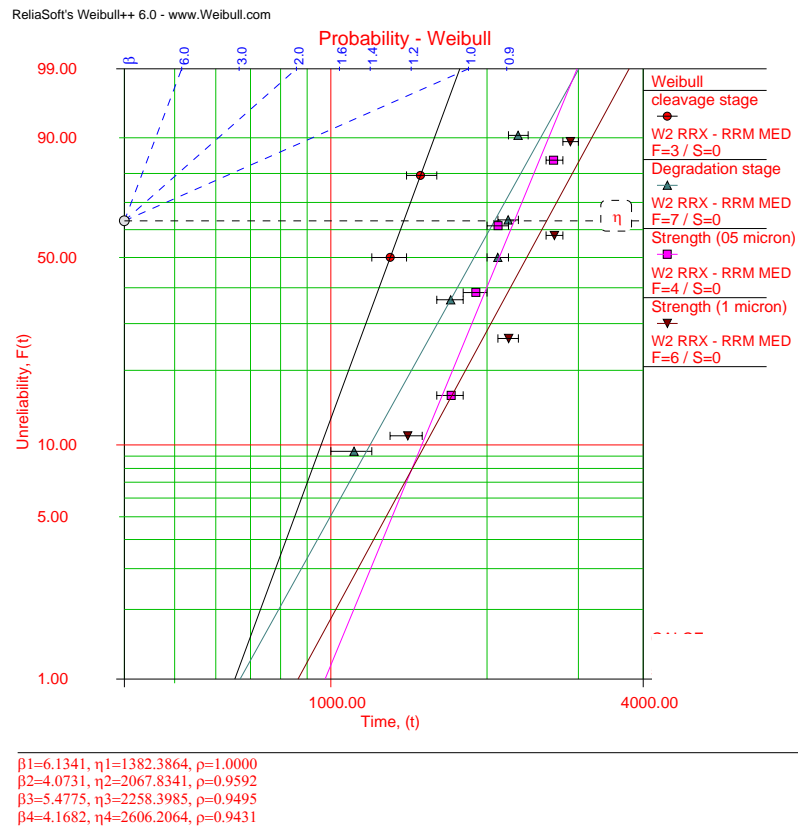


Figure 75 2P Weibull plot of fatigue data under bending fatigue with different failure modes.

	β (shape)	η (scale)
Interfacial brittle	6.13	1382
Transition	4.07	2067
Strengthening		
0.5 micron	5.47	2258
1 micron	4.16	2606

Table. 16 Values of Weibull parameters.

Last, the fracture morphology of the failed specimen and fatigue crack in specimens of each loading condition were examined using E-SEM. The failure site, mode and intermetallic phases were examined, as discussed in the next section.

5.4.4.3 Statistical Analysis – Two Sample T-Test

The statistical hypothesis test, two sample t-test, was performed on the collected fatigue life data to examine whether intermetallic layer thicknesses and/or aging had statistically significant effects on the fatigue life. The built in hypothesis test function in software, Origin 8 was used. The basic formula, procedure, and the meaning of the statistical parameters are discussed in this section. The results of the analysis of fatigue life data by t-test for intermetallic and/or aging effects will be incorporated into the later sections where those effects on fatigue life are discussed.

Hypothesis Test

In each problem considered, the question of interest is simplified into two competing claims / hypotheses between which we have a choice; the null hypothesis, denoted H_0 , and the alternative hypothesis, denoted H_1 .

We have two common situations:

1. The experiment has been carried out in an attempt to disprove or reject a particular hypothesis, usually the null hypothesis, thus we give that one priority so it cannot be rejected unless the evidence against it is sufficiently strong. This is the case for this study.

2. If one of the two hypotheses is 'simpler' we give it priority so that a more 'complicated' theory is not adopted unless there is sufficient evidence against the simpler one.

The hypotheses are often statements about population parameters like expected value and variance; for example H_0 might be that the expected value of the fatigue life of a sample with a 0.5 μm initial intermetallic layer is not different from the fatigue life of a sample with a 1 μm initial intermetallic layer. A hypothesis might also be a statement about the distributional form of a characteristic of interest, for example that the fatigue life for samples with a 0.5 μm initial intermetallic layer is normally distributed. The outcome of a hypothesis test is "Reject H_0 in favor of H_1 " or "Do not reject H_0 ".

Null Hypothesis

The null hypothesis, H_0 , represents a theory that has been put forward, either because it is believed to be true or because it is to be used as a basis for argument, but has not been proved. For example, in the present bending fatigue test, the null hypothesis might be that the fatigue life is the same for different interfacial intermetallic thickness. We would write

H_0 : there is no difference between the two fatigue lives for two different intermetallic thicknesses on average.

We give special consideration to the null hypothesis. This is due to the fact that the null hypothesis relates to the statement being tested, whereas the alternative hypothesis relates to the statement to be accepted if / when the null is rejected.

Alternative Hypothesis

The alternative hypothesis, H_1 , is a statement of what a statistical hypothesis test is set up to establish. For example, in present bending fatigue test, the alternative hypothesis might be that the fatigue life is different for different interfacial intermetallic thicknesses, on average. We would write

H_1 : the samples with different intermetallic thickness have different fatigue life, on average.

The final conclusion once the test has been carried out is always given in terms of the null hypothesis. If it is concluded "Do not reject H_0 ", this does not necessarily mean that the null hypothesis is true. It only suggests that there is not sufficient evidence against H_0 in favor of H_1 . Rejecting the null hypothesis then, suggests that the alternative hypothesis is true to some confidence level.

Two Sample T-Test

T-test makes the following assumptions and can be meaningfully applied only insofar as these assumptions are met:

- That the two samples are independently and randomly drawn from the source population(s).
- That the scale of measurement for both samples has the properties of an equal interval scale.
- That the source population(s) can be reasonably supposed to have a normal distribution.

The two-sample t-test is one of the most commonly used hypothesis tests. It is applied to compare whether the average difference between two groups is really significant or if it is due instead to random chance by assuming each from an underlying normal distribution:

$$N(\mu_i, \sigma_i^2), \text{ where } i=1, 2. \quad (16)$$

When carrying out a two sample t-test, it is usual to assume that the variances for the two populations are equal, i.e.

$$\sigma_1^2 = \sigma_2^2 = \sigma^2 \quad (17)$$

The null hypothesis for the two sample t-test is:

$$H_0: \mu_1 = \mu_2 = \mu_d \quad (18)$$

That is, the two samples have both been drawn from the same population. This null hypothesis is tested against one of the following alternative hypotheses, depending on the question posed.

$$H1: \mu_1 \text{ is not equal to } \mu_2$$

$$H1: \mu_1 > \mu_2$$

$$H1: \mu_1 < \mu_2$$

Algorithm

Consider two independent samples X_1 and X_2 , of size n_1 and n_2 drawn from two normal population with means μ_1 and μ_2 , and variances σ_1^2 and σ_2^2 respectively, we have:

$$\bar{x}_1 = \frac{1}{n_1} \sum_{i=1}^{n_1} x_{1i}; \bar{x}_2 = \frac{1}{n_2} \sum_{i=1}^{n_2} x_{2i}; s_1^2 = \frac{1}{n_1 - 1} \sum_{i=1}^{n_1} (x_{1i} - \bar{x}_1)^2; s_2^2 = \frac{1}{n_2 - 1} \sum_{i=1}^{n_2} (x_{2i} - \bar{x}_2)^2 \quad (19)$$

where \bar{x}_1 and \bar{x}_2 are sample means and s_1^2 and s_2^2 are sample variances. Then we can compute the t test statistic by:

1) For equal variance is assumed, that is $\sigma_1^2 = \sigma_2^2$. In this case the test statistic t :

$$t = \frac{(\bar{x}_1 - \bar{x}_2) - \mu_d}{s_p \sqrt{(1/n_1 + 1/n_2)}} \quad (20)$$

has a t -distribution with $(v = n_1 + n_2 - 2)$ degrees of freedom and

$$s_p = \sqrt{\frac{(n_1 - 1)s_1^2 + (n_2 - 1)s_2^2}{n_1 + n_2 - 2}} \quad (21)$$

is the pooled variance of the two samples.

2) For equal variance is not assumed:

In this case the usual two sample t -statistic no longer has a t -distribution and an approximate test statistic, t' is used:

$$t' = \frac{(\bar{x}_1 - \bar{x}_2) - \mu_d}{\sqrt{\left(\frac{s_1^2}{n_1} + \frac{s_2^2}{n_2}\right)}} \quad (22)$$

And a t -distribution with v degrees of freedom is used to approximate the distribution of t' where

$$v = \frac{\left(\frac{s_1^2}{n_1} + \frac{s_2^2}{n_2}\right)^2}{\frac{(s_1^2/n_1)^2}{n_1 - 1} + \frac{(s_2^2/n_2)^2}{n_2 - 1}} \quad (23)$$

Then compare the t value with the critical value and we will reject H_0 if:

Two tailed test: $|t| > t_{\alpha/2}$;

Upper tailed test: $t > t_{\alpha}$;

Lower tailed test: $t < -t_{\alpha}$;

Significance Level

The significance level of a statistical hypothesis test is a fixed probability of wrongly rejecting the null hypothesis H_0 , if it is in fact true.

It is set by the investigator in relation to the consequences of such an error. That is, we want to make the significance level as small as possible in order to protect the null hypothesis and to prevent, as far as possible, the investigator from inadvertently making false claims.

The significance level is usually denoted by α

$$\text{Significance Level} = P(\text{type I error}) = \alpha$$

Usually, the significance level is chosen to be 0.05 to 0.1 (or equivalently, 5% to 10%).

All hypothesis t-test was conducted in present work by setting α value equal to 0.1, which means the probability of wrongly confirm the statistically significant difference between two samples is 10%.

P-Value

The probability value (p-value) of a statistical hypothesis test is the probability of getting a value of the test statistic as extreme as or more extreme than that observed by chance alone, if the null hypothesis H_0 , is true. It is the probability of wrongly rejecting the null hypothesis if it is in fact true.

It is equal to the significance level of the test for which we would only just reject the null hypothesis. The p-value is compared with the actual significance level of our test and, if it is smaller, the result is significant. That is, if the null hypothesis were to be rejected at the 10% significance level, this would be reported as " $p < 0.1$ ". The formula involved in the computation of a p-Value for t-Test is detailed below. It is the integral of the Student t-distribution probability density function:

$$P = \frac{1}{\sqrt{\nu} B\left(\frac{1}{2}, \frac{\nu}{2}\right)} \int_t^{\infty} \left(1 + \frac{x^2}{\nu}\right)^{-\frac{\nu+1}{2}} dx \quad (24)$$

where ν is the degrees of freedom, and B is the Beta function.

Small p-values suggest that the null hypothesis is unlikely to be true. The smaller it is, the more convincing is the rejection of the null hypothesis. It indicates the strength of evidence for say, rejecting the null hypothesis H_0 , rather than simply concluding "Reject H_0 " or "Do not reject H_0 ".

In this study, the p -value will be compared with a user-defined significance level, α , for which 0.05 is commonly used. And the null hypothesis H_0 will be rejected if $p < \alpha$.

5.5 Fatigue Failure Analysis

Indium attach fracture at cold temperatures is differentiated from creep rupture since the stresses at the bonding interfaces are much higher, and failure often occurs through the intermetallic layer. In order to have a fundamental understanding of the root cause of the fatigue failure, failure analysis was conducted after the bending fatigue test. Failure sites and fracture modes of indium solder joints under cyclic bending stress are addressed and discussed in this section. First, a general observation of the failure sites is presented and discussed; secondly, the influence of different amounts of intermetallic, loading frequency, fatigue ambient temperature and thermal aging on crack initiation and growth are shown, discussed and compared to attach fatigue failure at elevated temperature.

5.5.1 Fatigue Failure Site

Tested specimens were subjected to failure analysis either by cross sectioning and SEM examination to determine crack location and joint morphology, or by fractography of the top surface of completely separated specimens to provide a view of the crack path. A typical damaged joint is shown in Figure 76.

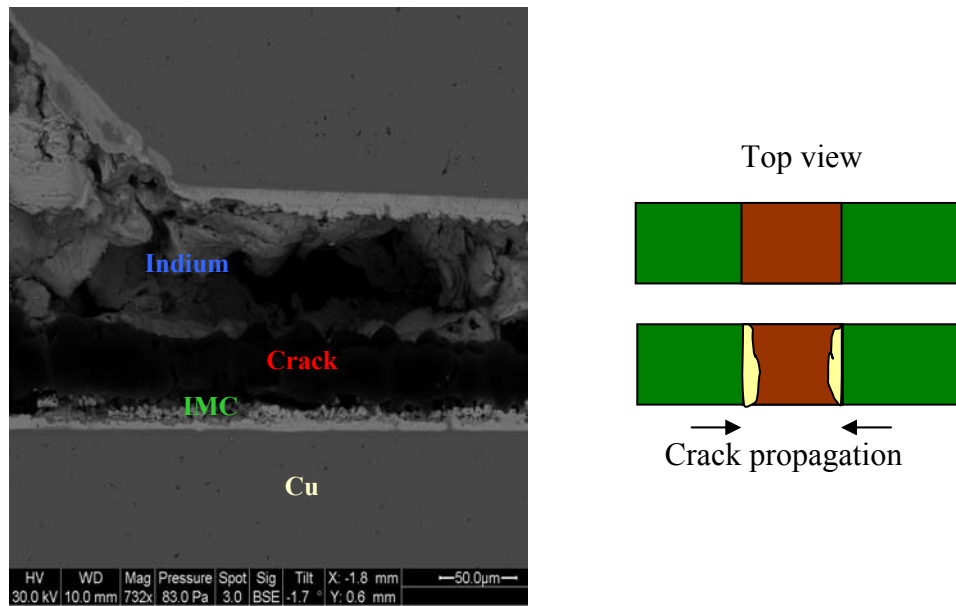


Figure 76 Fatigue crack in specimens under 3 point bending test (sample#9 @Au=1 μ m, 1 Hz).

Crack initiation occurred at the outside edges of the component copper strip at the interface between the substrate (i.e. the copper strip base) and the indium attach. Indium attach at the outermost edge will suffer the most applied deformation, while the center of the joint is in a minimum stress state. As a result, packages under repetitive 3 point bending will see crack initiation at the outermost edges.

Figure 77 provides a closer view of a fatigue crack propagating through the intermetallic layer in another sample under a different loading frequency (0.3 Hz) from the one shown in previous figure. However, cross sectioning of failed specimens is not sufficient to study the detailed fracture modes across the whole fracture surface. Therefore, the fracture modes were examined mainly based on the fracture morphology of failed specimens in next section.

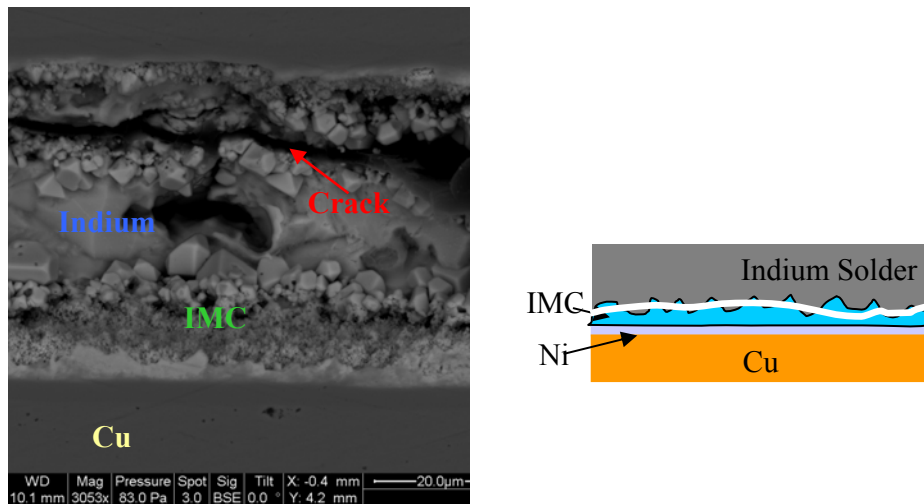


Figure 77 Fatigue crack through intermetallics layer in sample #9 with Au=1 μ m, 0.3 Hz.

5.5.2 Fracture Modes & Root Cause

Besides the difference in the failure initiation site for mechanical cyclic bending as opposed to temperature cycling failure, the fatigue failure mode is also different for isothermal cold temperature mechanical fatigue. In thermal cycling, the primary cause for indium attach failure is thermal fatigue, which was demonstrated in the present work and in previous work by other researchers [0,0,0]. In this failure mechanism, cracks in the indium attach usually initiate from the diagonal edge corner and propagate toward the center of the solder joint.

For mechanical cycling fatigue at cold temperatures, thermally induced processes, such as creep and stress relaxation, do not make any appreciable contribution to the mechanism of fatigue fracture. Under these conditions, Au-In intermetallics at the indium attach to Cu base substrate interface becomes the critical factor affecting the fatigue failure, especially when Au over Ni plating is used as a surface finish on the module substrate and component. Excessive intermetallics are brittle, porous, and provide

easier paths for cracks to initiate and propagate along the interface, especially at cryogenic temperatures.

In general, all specimens mechanically fatigued at -150°C and -55°C exhibited bulk-interfacial intermetallics brittle fracture, regardless of the Au metallization thickness, loading frequency or thermal aging effect. However, the thickness of the intermetallic layer and the extent of thermal aging did affect the fracture surface morphology and fracture locations inside the attach joint. These effects will be discussed separately in later sections.

Two modes of cracking were discovered within the sample at different locations. The initial fatigue crack observed at the outer edge of the component was flat and passed through the intermetallic layer because of the higher stress at the edges of the sample and the fact that maximum stress occurs within the intermetallic layer. However, as the crack moved toward the center line and the stress was reduced, the fracture morphology transformed into a dimple-like structure through the bulk indium at some locations, as shown in Figure 78 & Figure 79. Specifically, it can be seen that the bottom of the dimple is composed of broken pieces of AuIn_2 and their sides are formed of pure indium. Figure 80 illustrates the fracture process which results in the dimple morphology.

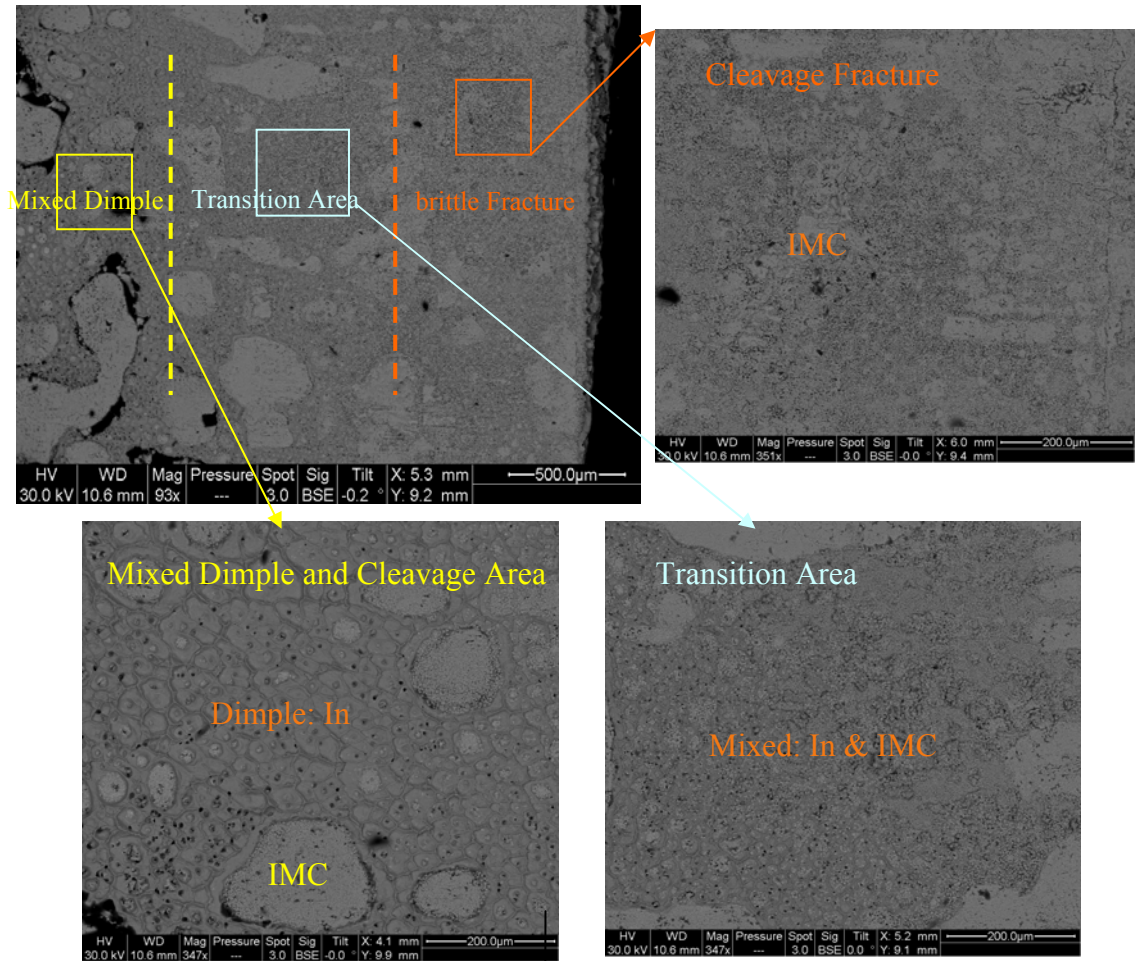


Figure 78 Brittle fracture through Intermetallic layer with different fracture modes from component side edge to center (sample#13 with Au=1 μm).

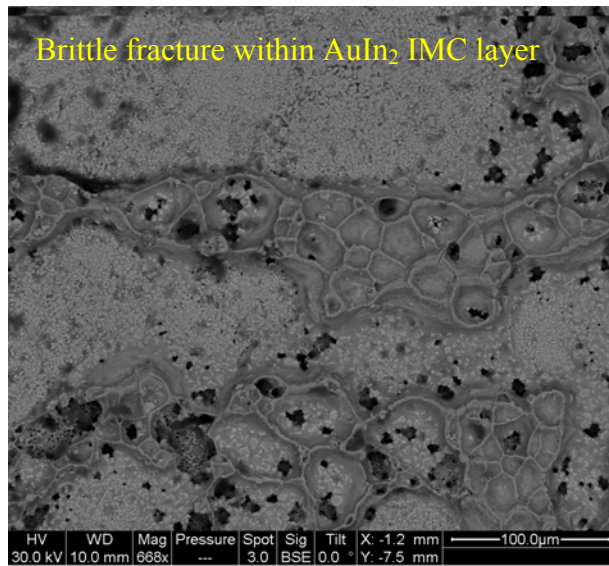


Figure 79 Fracture within IMC layer and dimple morphology of fracture surface subject to cyclic bending when the thickness of Intermetallic is between 5 and 12 μm (Sample#10 with Au=1 μm).

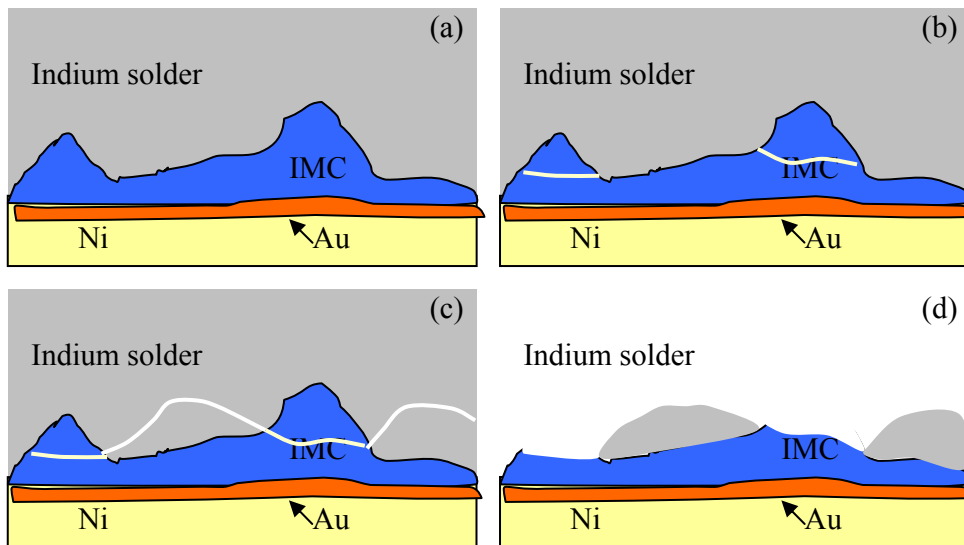


Figure 80 The evolution of dimple morphology.

5.5.3 Effect of Intermetallics

Recent years have seen the publication of several research studies concerning the effect of intermetallics on monotonic shear/tensile strength [0,0,0] at room temperature.

However, the relationships of mechanical fatigue life to the formation of intermetallics and the attendant fractographic morphology are seldom discussed for cold temperature applications. Therefore, the aim of current study is to investigate the interrelationship between mechanical fatigue life of solder joints, the interfacial intermetallics layers, and the corresponding fracture morphologies.

Several features of Au-In intermetallics which make them different from other common intermetallics, such as Cu_6Sn_5 and Ni_3Sn_4 must first be summarized, Seven intermediate phases have been observed in Au-In system: AuIn_2 , AuIn , Au_7In_3 , Au_3In and Au_4In [0]. AuIn_2 is the first compound to form and it makes up most of the reaction zone thickness. If enough gold exists, AuIn forms next. But AuIn_2 is the final phase in an indium rich environment due to the intermetallic reaction of Au and In. If the temperature is raised above the melting point of In (156°C), AuIn_2 will form within seconds, almost immediately upon bonding and remain stable. Furthermore, 14 year aging of Au-In alloys showed no decomposition of the intermetallic compounds originally formed [0,0,0]. No significant variation was observed in the grain size of AuIn_2 as a function of annealing time and temperature [0].

Given that there is only one dominant Au-In intermetallic phase, it enables us to study the effect of intermetallics only in terms of intermetallic thickness instead of needing to consider other factors, such as phase changes and distribution gradients. It should be mentioned here that the study in this section was conducted on freshly-made samples to eliminate the effect of thermal aging. The effect of thermal aging will be discussed in more detail in later section.

The thickness of the intermetallic plays a critical role in the determination of the fatigue life of the solder joint. Small, well distributed intermetallic precipitates in the bulk indium can strengthen and increase the fatigue life of solder joint, but excessively thick, highly voided, interfacial intermetallic layers will shorten the life. Two stages in fatigue life were observed in terms of intermetallic thickness as shown in Figure 81: the intermetallic strengthening stage and intermetallic degradation stage.

The fatigue life difference was examined by t-test to check whether it is statistically significant or not. It was shown that the fatigue life difference with respect to various thicknesses of intermetallics is statistically significant between specimens in strengthening stage, indicating higher strength for thicker intermetallic in that range, and those with intermetallic thickness of 11 μ m in strengthening stage with those in fully interfacial brittle stage, indicating a lower strength for thicker intermetallic in that range. However, the characteristic fatigue life of specimens with 5.8 μ m thick intermetallics is not significantly different from those in degradation stage. However, the microstructural analysis conducted to study the fracture modes showed that they have different microstructure characteristics and belonged to different stages. Therefore the effect of intermetallic thickness on fatigue life is nonmonotonic, with fatigue life increasing with intermetallic thickness in the strengthening phase and decreasing with intermetallic thickness in the degradation phase.

Stage	IMC thickness	Sample size	Mean lifetime	Significance level (α)	p	Difference
strengthening	5.8	4	2200	0.05	0.029	significant
	11	4	2850			

strengthening	5.8	4	2200	0.05	0.46	Not significant
degradation	24	4	2175			
strengthening	11	4	2850	0.05	0.01	significant
Interfacial brittle	28	4	1400			

Table. 17 Hypothesis t-test results in terms of different intermetallic thicknesses.

As mentioned in previous paragraph, the crack morphology in the specimens with different initial gold coating thicknesses were examined, and the thickness of the intermetallic layers and their interface roughness had an important influence on the fatigue life of the attach and the crack morphology. The difference in the roughness of the AuIn₂ intermetallic fracture surface and the amount of dimple-like surface are the reason for the fatigue life difference in 1 and 3 um Au coated specimens at the strengthening stage and degradation stage respectively.

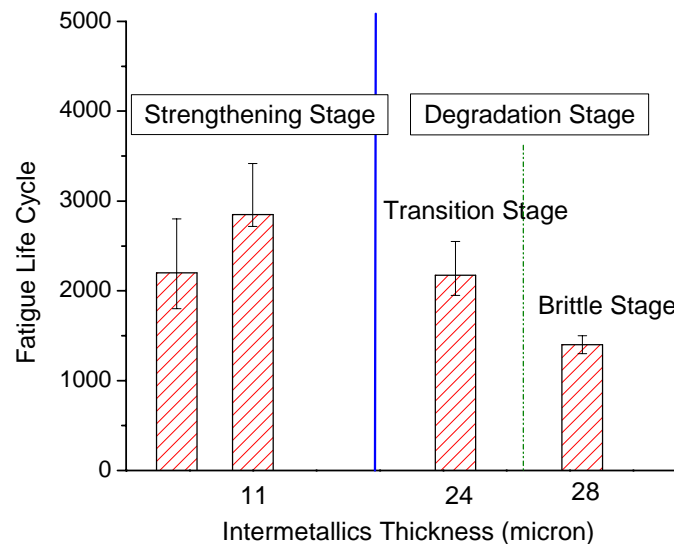


Figure 81 Relationships of fatigue life with intermetallics content of solder joint.

Cross-sectioning revealed that for the 0.5 μm Au coated samples, the intermetallic was relatively thin and smooth with a significant unreacted layer of pure In attach in the middle of the joint. 1 μm Au coated samples had a slightly thicker and wavier intermetallic layer, but still exhibited a sizeable unreacted layer. 3 μm Au coated samples had a much thicker and rougher intermetallic layer.

When fatigue tested, it was found that the crack initiated in the brittle Au-In intermetallic layer at the outer edge of the component strip at the attach to substrate interface. The crack then propagated by a mixed-mode mechanism as it moved through both intermetallic and bulk indium layers. It is supposed that cracks were sequentially initiated in the intermetallic and blunted in the indium, lengthening the time needed for crack propagation to failure.

The initial increase in intermetallic thickness and waviness going from 0.5 μm Au coated samples to 1 μm Au coated samples did not harm the integrity of the joint and may have slightly increased its fatigue resistance, as its waviness forced the crack to go through more initiation/blunting transitions. This is shown in the fractographs by a larger area of dimpled, ductile fracture through the indium. There is also a higher concentration of small, well-distributed Au-In intermetallic particles strengthening the bulk solder and making the propagation of the crack through the indium more difficult. This increase in time-to-failure is shown in the figure above, and so this is termed the strengthening stage.

However, the increase in thickness and roughness of the intermetallics when going from 1 μm Au coating to 3 μm Au coating had the opposite effect. In this case, the intermetallic thickness was significantly large and the grain sufficiently coarse to make

crack re-initiation quite easy while limiting the amount of crack area exhibiting the ductile, dimpled look of indium fracture. This reduced the time-to-failure as shown in the figure above, and is termed the transition – to – degradation region.

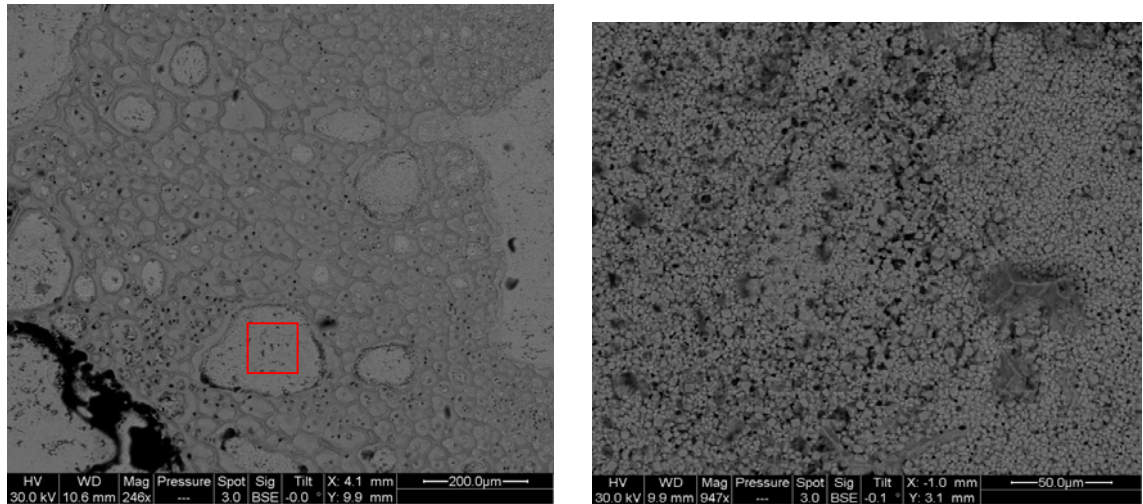


Figure 82 Fracture surface of samples with 1 μm Au coating and about 12 μm thick Intermetallic: (a) dimple-like surface mixed area; (b) enlarged Intermetallic delaminating area.

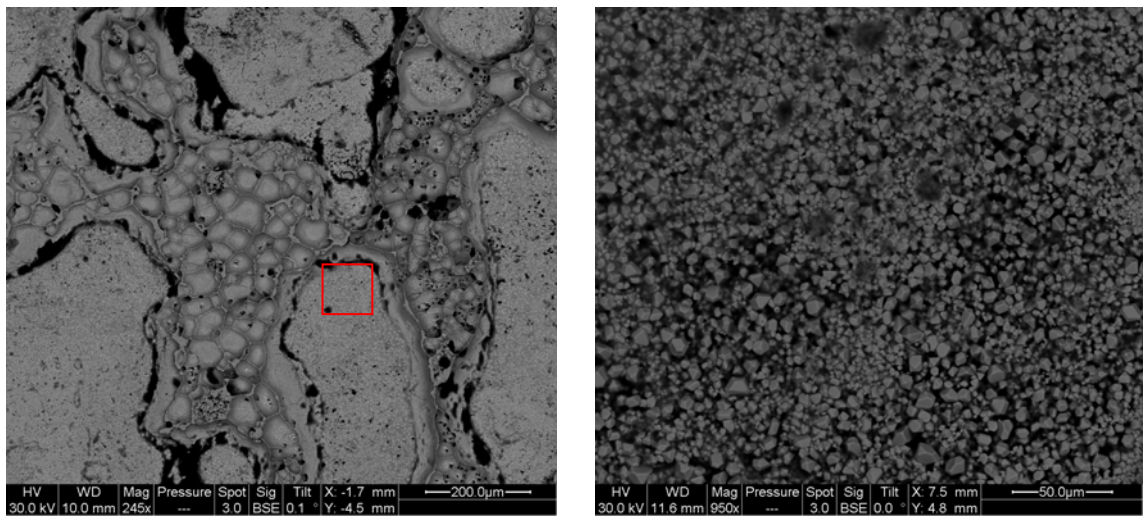


Figure 83 Fracture surface of samples with 1 μm Au coating and about 12 μm thick Intermetallic: (a) dimple-like surface mixed area; (b) enlarged Intermetallic delaminating area.

5.5.4 Effect of Thermal Aging

As discussed in section 5.5.2, all specimens failed by indium bulk-interfacial intermetallics fracture, regardless of aging condition. However, thermal aging contributes to intermetallic growth and as a result, it does affect the fatigue life and fracture surface morphology. In this section, the thermal aging effect will be discussed in terms of intermetallic growth, fatigue life, crack growth rate, and fracture morphology

In general, the effect of thermal aging can be divided into two categories based on the intrinsic features of intermetallics with respect to their strengthening or degradation effect on solder joint:

- Strengthening stage: fatigue life stays the same or increases to a small extent due to increased intermetallic strengthening and annealing. This is the case for the 0.5 μm and 1 μm Au coated samples before and after aging
- Degradation stage: fatigue life decreases significantly, as a result of the creation of thicker, rougher, and more porous intermetallics. This is the case for the 3 μm Au coated samples before and after aging.

The fatigue life increases or at least not decreased after thermal aging for specimens with intermetallic thicknesses less than about 15 μm (i.e. in strengthening stage). For those samples having excessive (i.e. more than 24 μm) intermetallic thickness, fatigue life is shorter after thermal aging because of the deleterious effect on the solder attach from increased porosity and roughness of intermetallic as shown in Figure 84. The optimal intermetallic thickness, where solder joint has maximum fatigue life is between 11 μm and 24 μm in this study for a joint made initially with 100 μm indium perform.

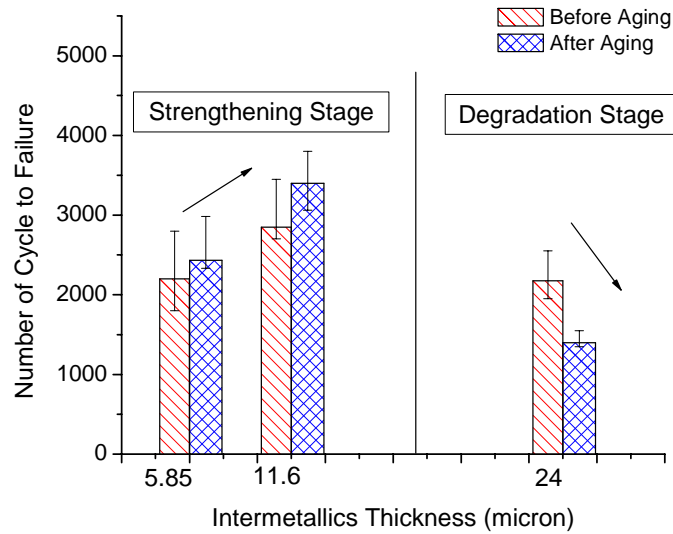


Figure 84 Fatigue life of solder joint with various Intermetallic thicknesses before and after aging.

It was examined and proven that fatigue life of specimens with different intermetallic thickness is significant. It was observed that this difference is more prominent after thermal aging. T-test was conducted in this section to verify whether thermal aging results in fatigue life change before and after thermal aging and whether it is statistically significant or not as listed in the following table.

Stage	Au Thickness	Sample size	Mean lifetime	Significance level (α)	p	Difference
strengthening	0.5	4	2200	0.05	0.07	Not significant
	0.5 (aged)	3	2800			
strengthening	1	4	2850	0.05	0.02	significant
	1 (aged)	3	3400			
degradation	3	4	2170	0.05	0.004	significant
	3 (aged)	3	1450			

Table. 18 Hypothesis t-test results before and after thermal aging.

For specimens with thinnest Au coating or intermetallics, it was observed that fatigue life increase before and after thermal aging is not significant. But solder joint fatigue degradation and premature failure was not observed. Moreover, as the thickness of Au coating or intermetallic layer increases, it was shown that effect of thermal aging was more significant but nonmonotonic. Thermal aging results in the increase of fatigue life as thickness of intermetallic layer thickness is increased initially (within strengthening stage). However, it was observed that fatigue life was shortened when excessive thick intermetallic layer was existed (degradation stage). Therefore, it can be concluded that thermal aging does not cause solder joint degradation, some cases it may even contribute to a longer fatigue life due to its strengthening effect, when the intermetallic layer thickness is within the strengthening stage.

In order to explain this phenomenon by the underlying fundamental physical features, this change in fatigue life with respect to various intermetallic thicknesses is also correlated to the intrinsic features of the intermetallics and fracture morphology as shown in the figure below. For those specimens with 0.5 and 1 μm thick Au coating, the observed fracture modes represent intermetallic cracking and dimple-like mixed fracture through the indium after thermal aging. The fracture morphology did not change significantly and fatigue life increased a little bit due to recrystallization and growth of intermetallics. The corresponding failure photographs of thermally aged joints i.e. samples of Au = 0.5 μm and Au = 1 μm , are illustrated in Figure 85, respectively.

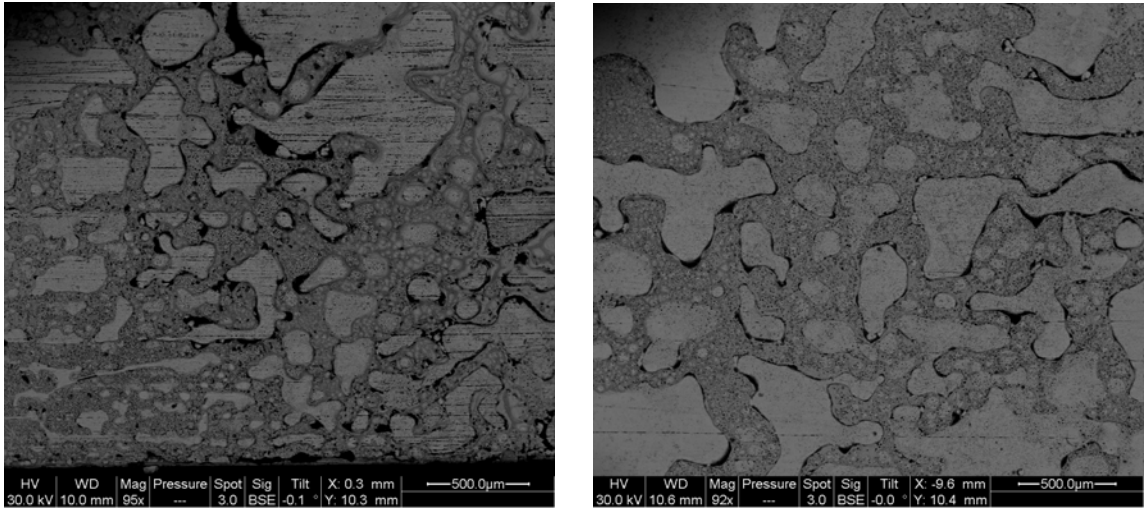


Figure 85 Fracture surface of samples with 1 μm thick Au metallization.

As the total thickness of the interfacial intermetallic layers grows beyond 25 μm (3 μm thick Au metallization) after thermal aging, the intermetallic interface becomes much rougher and consumes more of the joint volume, causing the fracture surface to move further into the interior of this layer. As a result, the fractography transforms to brittle fracture through the intermetallic without the dimpled region, as shown in Figure 86, and the fatigue life drops significantly (40%).

As the total interfacial intermetallic layer thickness continues to grow, there is no further change in the fracture mechanism, (i.e. all subsequent fractures also demonstrate a flat, brittle fractography through the intermetallic). Accordingly, increased intermetallic layer growth is accompanied by a gradual decrease in joint strength.

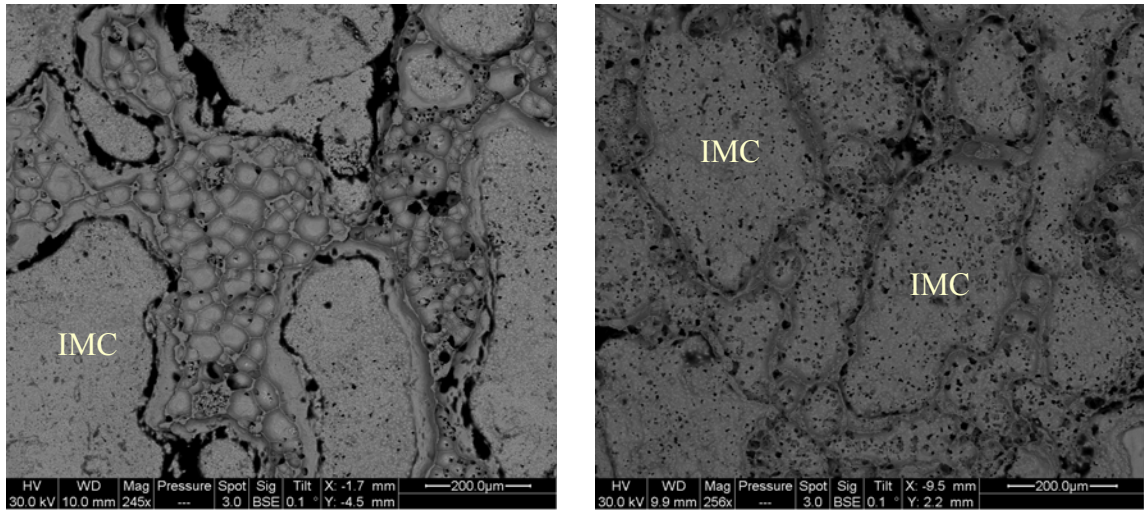


Figure 86 Fracture surface of samples with 3 μm thick Au metallization.

The fatigue crack growth is another indicator of fracture characteristics in the fatigue specimen. As shown in Figure 87, when placed under the same loading conditions before and after aging, the crack propagated much faster in those specimens with 3 μm Au coating after thermal aging, indicating aging-induced degradation of the joint as discussed above. In contrast, the crack growth rate in those specimens with 0.5 μm thick Au coating is relatively insensitive to thermal aging, but does drop some, which is consistent with the aging-induced improvement in fatigue resistance discussed above due to increased dimpled surface cracking.

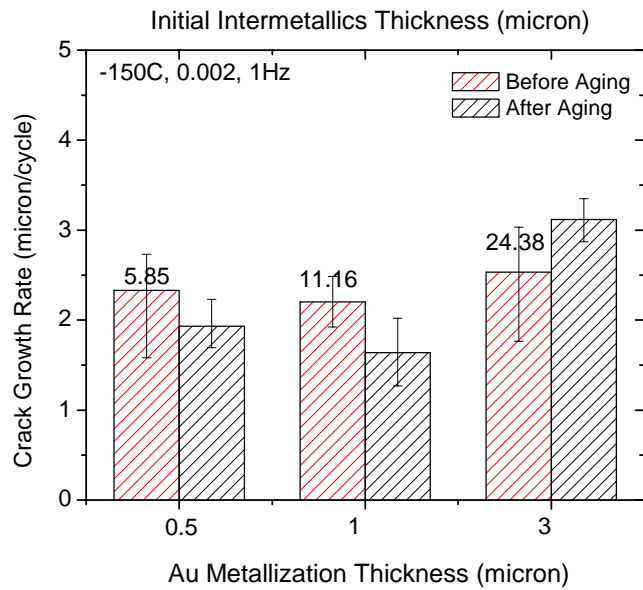


Figure 87 Thermal aging effect on crack growth rate according to different Au coating thickness.

5.5.5 Effect of Fatigue Temperature

At both -150°C and -55°C , fatigue failures were caused by fracture through brittle intermetallics at the solder to copper base strip interface as discussed in section 5.5.2. It was not observed that the fatigue temperature had any prominent effect on the fracture modes in indium solder joint within the range of temperature studied. In both cases, brittle fracture was observed at the component edge, where the crack was initiated, which then transformed to a mixed dimple-like morphology as the fatigue crack propagated toward the center line of the component.

Nevertheless, the fatigue life of the solder significantly improved at -55°C for all specimens with various Au coating thicknesses from 0.5 to 3 μm , as shown in Figure 88. It is resulted from the combined effect of higher strength and improved toughness of the

attach at the higher temperature (-55°C) due in part to additional time-temperature dependent, viscoplastic deformation behavior of indium solder joint.

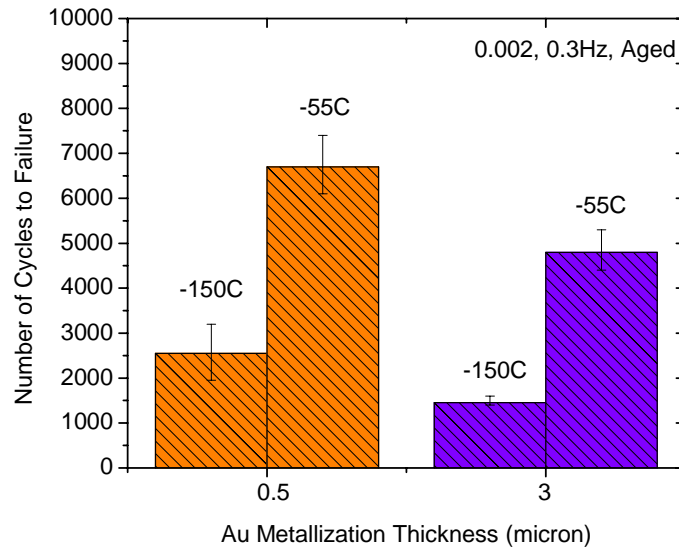


Figure 88 Temperature effect on fatigue life with different amount of Intermetallic.

At higher temperature, indium becomes less stiff and the stress in the solder is decreased for the same amount of deformation. Therefore, the strain energy density dissipated within each fatigue cycle will decrease, because of the lower stress level for the same strain range. This is confirmed by FEM simulation results, discussed in Section 5.7. In contrast to temperature cycling, however, damage from creep/stress relaxation of the attach during dwell is not a serious concern at -55°C since the temperature is just at 0.5 T_m of indium and the loading cycle has a short period not permitting significant creep and stress relaxation.

5.5.6 Effect of Loading Frequency

The effect of loading frequency is also studied at frequencies of 0.3, 1 and 3 Hz with 0.002 loading strain amplitude positive sine waveform (Figure 89). Specimens under 3

Hz loading frequency have only slightly improved characteristic fatigue life vs. those under 1 Hz loading, but a larger increase is observed going from 0.3 Hz to 1 Hz loading especially for specimens with 0.5 μm and 1 μm Au coating thicknesses, as shown in Figure 90.

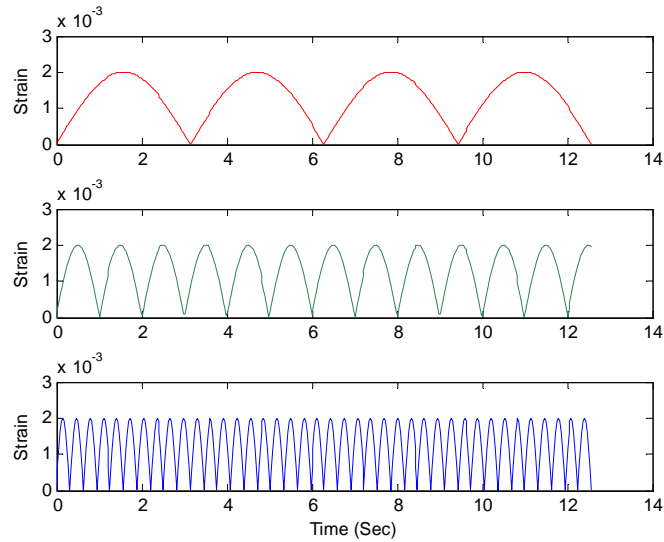


Figure 89 Loading profile in bending fatigue test with different frequencies.

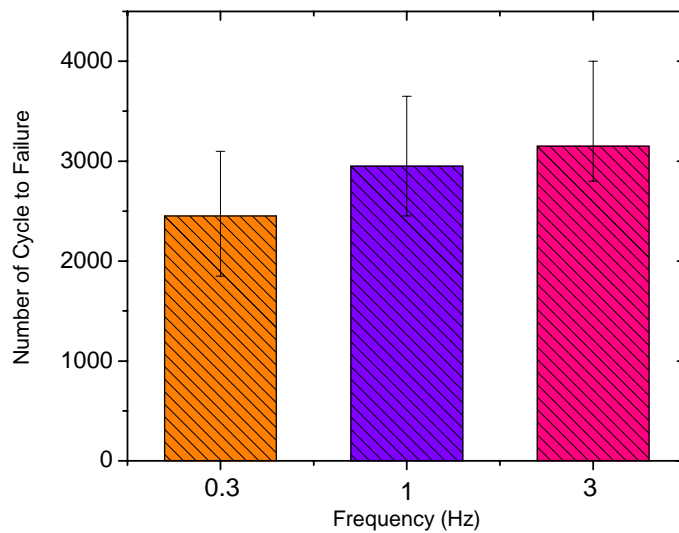


Figure 90 Effect of loading frequency on fatigue life of indium solder joint @ -150°C (Au=0.5 μm).

All viscoplastic materials, such as indium, will show an increase in fatigue life with faster strain rate because there is less time for time-dependent deformation mechanisms. As ductile fatigue of indium is a function of strain rate, but cracking through the brittle intermetallic is time-independent, it makes sense that the increases in fatigue life due to higher frequency are more prominent for samples whose fracture surfaces are predominantly through the indium (i.e. more dimpled surface), than those whose fracture surfaces are predominantly through the intermetallic. So specimens having 0.5 um Au coating, exhibit the biggest increase, 30% in fatigue life because they have the least intermetallic on the fracture surface. Second, are specimens with 1 um gold coating and last are those having 3 um thick Au coating, where only a 4.2% increase as listed in Table. 19.

It should be noted that specimens having 0.5 um thick Au coating don't have the longest fatigue life although they have the most dimpled fracture surface and therefore the most strain rate related increase in fatigue life. It is again demonstrated that the amount of indium solder joint and intermetallic therefore have an optimum combination ratio. The appropriate amount of intermetallic strengthens the solder joint, resulting in higher fatigue resistance and maximizing the fatigue life of the attach bond line.

Au Thickness	Fatigue Life Increase in Percentage	Fatigue Life @ 3Hz
0.5 um	30.5%	3150
1 um	28.9%	3600
3 um	4.2%	1925

Table. 19 Fatigue life increase as frequency rises from 0.3 Hz to 1Hz.

It should be noted that the difference in the strain-rate induced increase in fatigue life of specimens with 0.5 and 1um thick Au coating is not as great as that between either of them and the 4.2% for specimens with 3 um thick Au coating. This again confirms the similarity of the fracture morphology for the 0.5 um and 1 um samples and the difference between this and the almost full brittle cracking of the 3 um Au coating.

5.6 Discussion and Summary

Fatigue life and fracture modes of indium joints under cyclic bending at extended cold temperature have been investigated and reported. Among all factors being investigated, the amount of brittle intermetallics at the attach interface has the biggest degrading effect on solder joint integrity and fatigue life, with much smaller effects due to external loading conditions, such as fatigue temperature, loading amplitude and loading frequency. In particular, the following findings were made:

- (1) It is observed that the fatigue life of indium solder joints at extreme cold temperature is different and the fracture morphology significantly changed depending on the amount of intermetallic phases present. These Au-In intermetallic layers form during reflow, but also during aging, prolonged storage, and long term operation at high temperature condition.
- (2) It has been demonstrated that both the total thickness of the interfacial intermetallic layers and their interface roughness influence the fatigue life and the fractographic morphology, as summarized in Table. 20. Generally, the effect of intermetallics can be divided into two categories resulting in solder joint strengthening for thin layers

- (i.e. formed from 0.5 and 1 μm thick Au coating) and degradation for thick layers (i.e formed from 3 μm thick Au coating).
- (3) For those fatigue specimens, whose total interfacial layer thickness of intermetallic is less than 15 μm , the fractography transforms to a mixed dimple morphology from brittle fracture at the edge of component where it initiated. The bottom of the dimple is composed of broken AuIn_2 while its sides are made up of solder. Cracking occurs initially in the waist of the protruding AuIn_2 tips and then propagates into the solder at an angle of approximately 45° with respect to the solder/ AuIn_2 interface to form the observed dimple morphology. The size and depth of the dimple morphology is related to surface roughness and the size of intermetallic protrusions. The dimple size increased while the fraction of the fracture surface covered by dimples decreased as the thickness of the intermetallics increased, resulting in decreases in the fatigue life. As the total thickness of intermetallic keeps increasing to 28 μm , the fracture shifts to pure brittle fracture through the intermetallic.
- (4) For those specimens with 0.5 and 1 μm thick Au coating, their fractography has the same characteristics before and after thermal aging. The increase of intermetallic thickness after thermal aging leads to more strengthening in solder joint and longer fatigue life. It was observed that crack growth of these specimens is relatively insensitive to thermal aging and crack growth rates can decrease slightly.

However, for specimens having excessive intermetallic (formed from 3 μm thick Au coating), the solder/ AuIn_2 interface is much rougher and is accompanied by an accumulation of residual transformation-induced stress due to intermetallic growth. For these specimens, thermal aging has a deleterious effect on fatigue life, with the

position of the initial fracture moves towards the interior of the intermetallic layer and resulting in a lateral propagation of a crack through this layer. This is also a result of increase porosity in the intermetallic after aging.

It is summarized in the following table.

Temperature		-150°C		Fatigue Life Change Before and After Aging
Age Condition		Non Aged	Aged	
Au Metallization Thickness	0.5 um	dimple	dimple	No degradation
	1 um	dimple	dimple	No degradation
	3 um	dimple	flat	reduced

Table. 20 Fatigue failure sites and modes under different ambient temperature

Because much of the fatigue life of the 0.5 um and 1 um samples is being controlled by fracture through the ductile dimpled region, the macroscopic damage based fatigue model was validated and calibrated for these specimens with intermetallic less than 15um. In the following two sections, the FEM modeling of cyclic bending fatigue of specimens at various temperatures, loading amplitudes and frequencies was performed to calibrate a damage based energy density fatigue failure model.

5.7 Finite Element Modeling of Bending Fatigue

FEA modeling of bend fatigue tests was conducted to investigate the stress/strain behavior of the attach joint. A quarter of the specimen was modeled in 3D nonlinear structural analysis. The solder joint material was modeled as a viscoplastic solid and the rest of the materials as linear elastic solids. According to the test conditions, the model is

constrained at both symmetric planes and fixed in the out-of-plane direction at the middle in order to simulate the middle loading edge. At the end of the specimen, a displacement is applied to simulate the applied load.

The goal of the simulations was to calculate the inelastic work per unit volume (or viscoplastic strain energy density) accumulated per loading cycle, which is considered as a damage parameter later in fatigue model since it is a comprehensive factor to consider both stress and strain effects. The strain energy has the maximum at the outer side edges because of the free edge effect. Either nine or ten complete fatigue cycles were simulated in order to establish a stable stress-strain hysteresis loop. The plastic work accumulated during the last cycle was used for all crack growth correlations. A typical quarter symmetry model is shown in Figure 91.

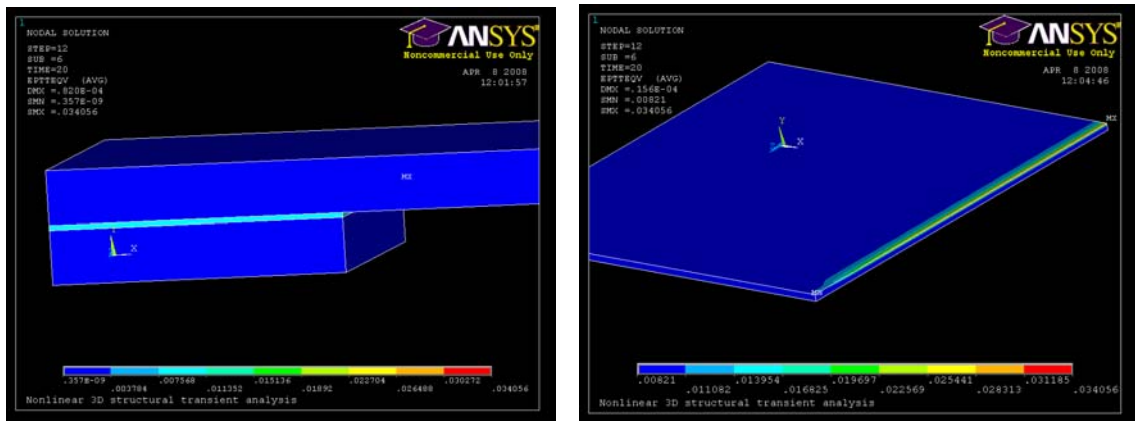


Figure 91 Quarter symmetry model for mechanical fatigue at -150°C (a) overview; (b) solder joint layer.

A volume averaging technique was used to reduce the sensitivity to meshing. The strain energy density of each element is normalized by the volume of the element.

$$\Delta W_{ave} = \frac{\sum \Delta W \cdot V}{\sum V}$$

where ΔW_{ave} is the average viscoplastic strain energy density accumulated per cycle for the interface elements, ΔW is the viscoplastic strain energy density accumulated per cycle of each element.

The simulation result shows that the accumulated strain energy density on bottom layer is much higher than that on top layer due to bending effect of base substrate. Therefore, the subsequent analysis will focus on bottom layer volume-averaged result as shown in Figure 92.

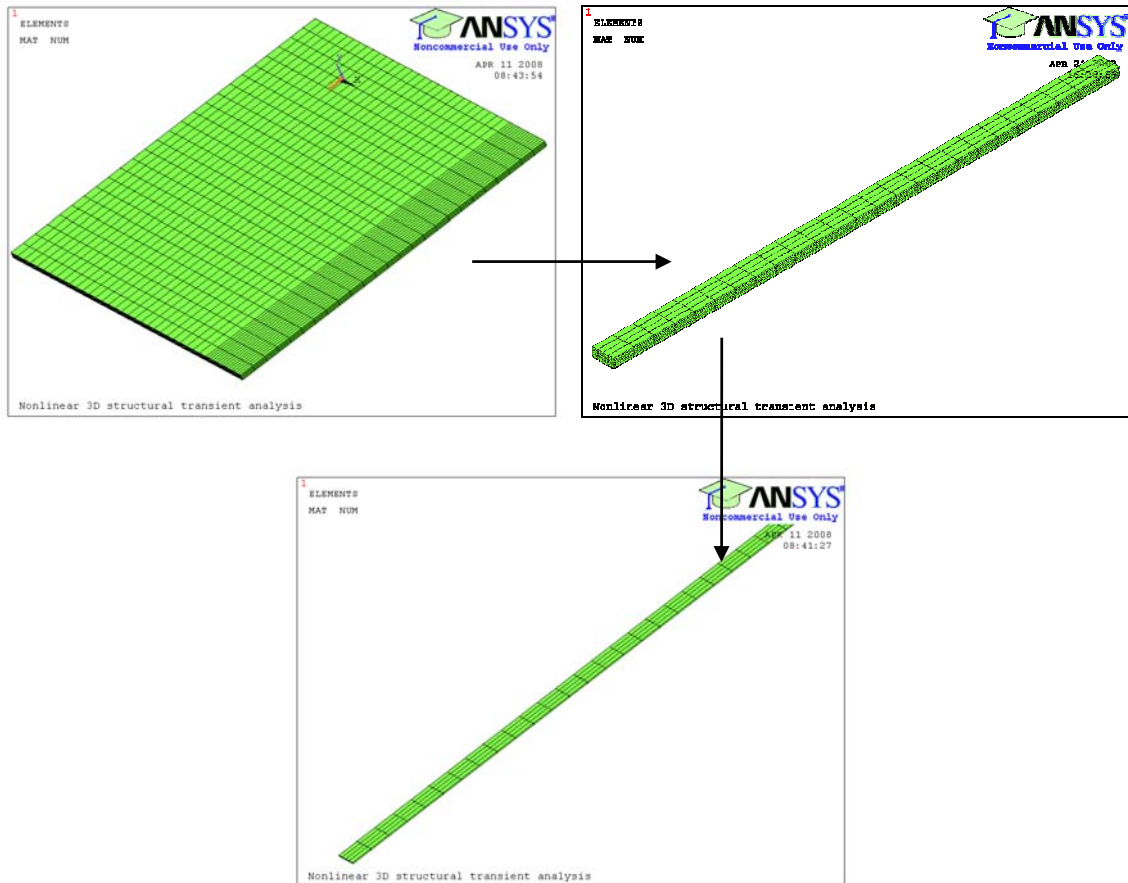


Figure 92 Volume averaged elements on the top layer.

Values for the total strain energy density increase per cycle are averaged over 5% volume near the worst stress/strain concentration at the critical outer edge of component as shown in Figure 92. An element layer of 10 μm thickness at the interfaces is being used as a standard criterion to average the strain energy density to be used in durability models. A typical hysteresis loop and averaged strain energy density are shown as following pictures for fatigued specimens under 0.3Hz and 0.002 at -150°C .

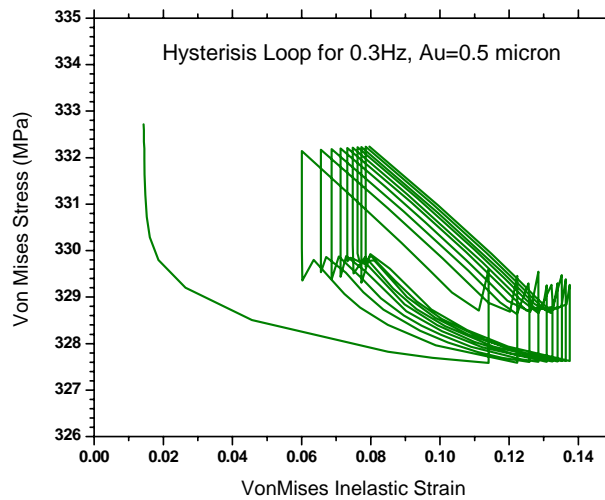


Figure 93 Hysteresis loop of indium solder joint after 10 loading cycle at the most outer edge of component ($\text{Au}=0.5\mu\text{m}$).

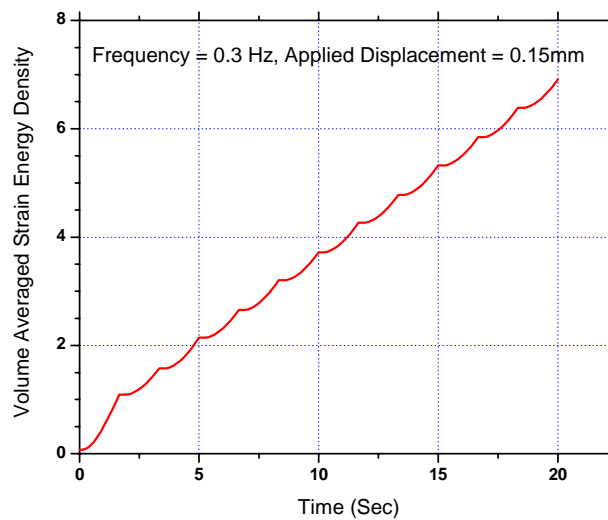


Figure 94 Averaged strain energy density at the critical site in solder joint ($\text{Au}=0.5\mu\text{m}$).

In general, mechanical loading is much faster than thermal loading with each cycle taking only a few seconds whereas in thermal cycling, each cycle takes at least several minutes, or even hours. Typically for thermo-mechanical loading it takes only a few simulation cycles to reach convergence [0]. For example, it took only 4 cycles to reach convergence for the indium solder joint under thermal shock test in chapter 4. However, it takes more simulation cycles to obtain the converged results for fast mechanical loading because the full viscoplastic behavior of the attach is not revealed during the short loading cycle period. For bending reliability test with 1 Hz loading, 10 cycles were simulated to achieve a 5% energy difference between two consecutive cycles, which is considered as an applicable convergence criteria [0].

The inelastic strain energy density results were obtained for different simulation conditions are listed in Table. 21, these results will be needed in fatigue life prediction.

Data Set	Temperature (°C)	Load Frequency (Hz)	Strain Amplitude	Energy Density (MPa)
1	-150	0.3	0.002	0.94316
2	-150	1	0.002	0.94789
3	-150	0.3	0.004	4.1784
4	-150	0.3	0.003	2.6077
5	-55	0.3	0.002	0.77245

Table. 21 Isothermal fatigue conditions for crack growth study.

5.8 Fatigue Life Prediction

In this section, the fatigue life of a component on a base substrate under extended low temperature mechanical fatigue was modeled by correlated the measured crack growth

data with the calculated inelastic strain energy density per cycle in the solder using the accumulated damage energy based model developed by Darveaux [0]. The crack growth data were fit to relations of the form:

$$\text{Cycles to crack initiation: } N_o = K_1 \Delta W_{ave}^{K_2}$$

$$\text{Crack propagation / cycle: } \frac{da}{dN} = K_3 \Delta W_{ave}^{K_4}$$

Shown in Figure 95 and Figure 96 is the crack initiation and crack growth rate correlations. The strain energy density values were averaged over the first element layer next to the Cu base substrate side as shown in previous section.

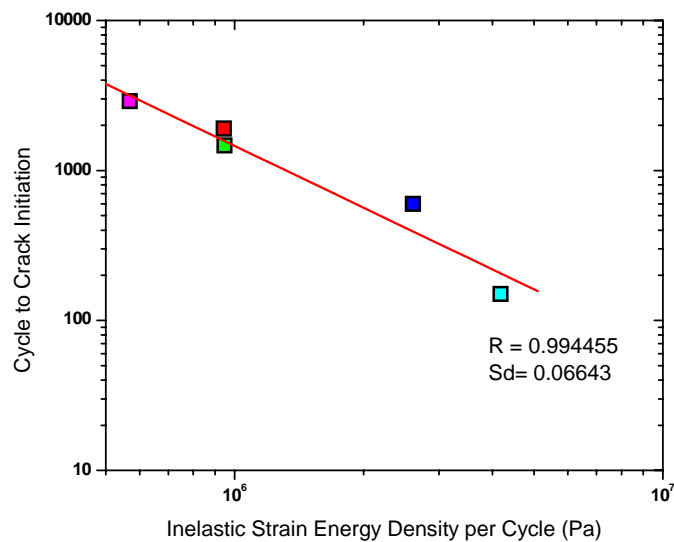


Figure 95 Crack initiation correlation.

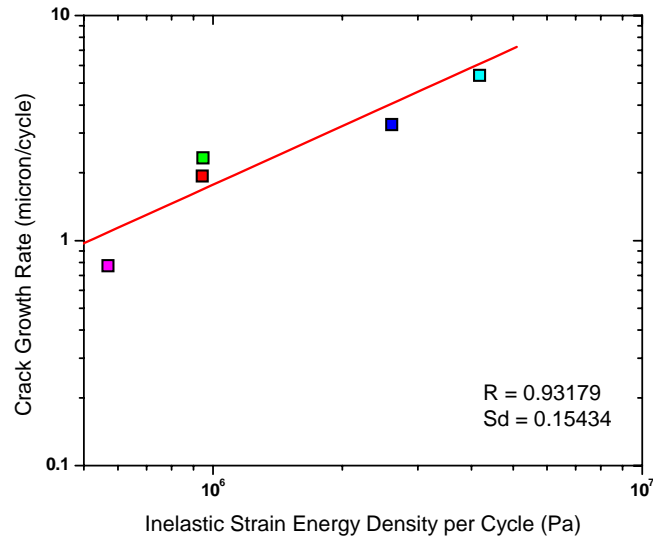


Figure 96 Crack growth rate correlation.

The crack growth rate was shown to be constant during fatigue cyclic loadings. The crack fatigue life can be calculated by adding the number of cycles for crack initiation plus the number of cycles for crack propagation across the joint interface. Here we define the equivalent fatigue crack length as half of the component length, which is 3mm. and the fatigue life can be predicted through the following equation and the material parameters were determined by nonlinear fit as listed in Table. 22:

$$N_f(63.2\%) = N_o + \frac{a}{\left(\frac{da}{dN}\right)}$$

$$= K_1(\Delta W)^{K_2} + \frac{a}{K_3(\Delta W)^{K_3}}$$

K ₁ (cycles/Pa ^{K₂})	K ₂	K ₃ (um/cycle/Pa ^{K₄})	K ₄
2.40E11	-1.37	1.15E-5	0.86

Table. 22 Crack growth correlation constants.

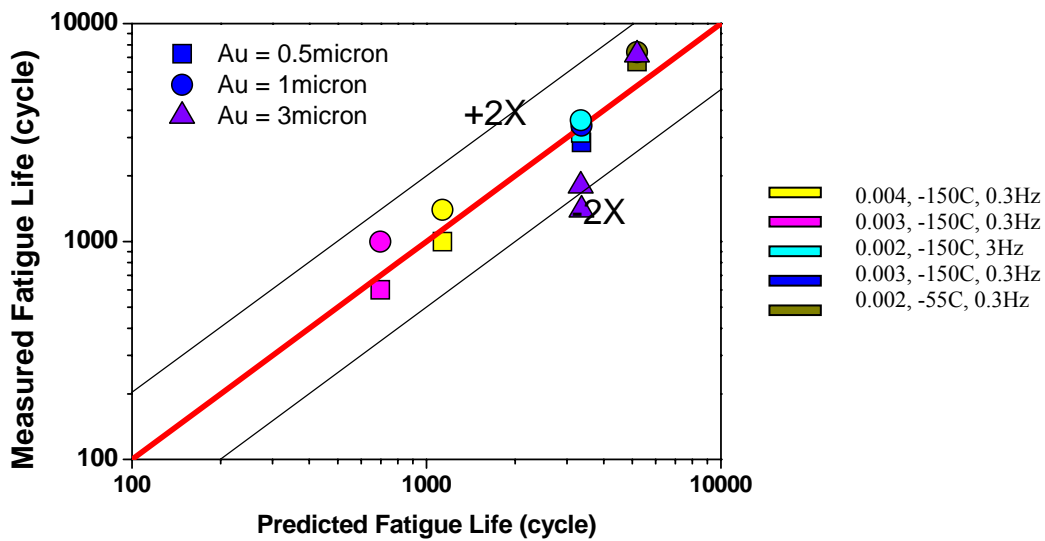


Figure 97 Fatigue life deviations with different Au-In intermetallic thicknesses.

As is shown in Figure 97, the life prediction for specimens with 1 μ m thick Au initial coating, using the model calibrated for the 0.5 μ m thick initial Au coated samples, is a somewhat conservative since there is a strengthening effect resulting from thicker intermetallics that is not addressed in this model. But they are still within the 2X prediction region that is considered sufficient for validation. Future work will focus on developing a fundamental-based correction factor for this effect.

The present SiGe electronic module is designed to operate reliably in cryogenic environment as well as normal environment during its mission on the moon. Besides the thermal fatigue resulted from daily temperature cycles as what we discussed in previous chapter, the electronic module is also subjected to the isothermal/mechanical fatigue. For example, the intelligent node made up of sensors and actuators, undergoes power cycling, mechanical cyclic loading and vibration loading when moving around on the surface of

the moon to acquire scientific data.

The previous studies showed that indium solder joint is one of the critical sites for fatigue failure occurrence [0,0]. In order to evaluate the fatigue performance of chip on board (first level) and substrate on package (second level) and improve the overall reliability of the whole system the isothermal fatigue data of indium solder joint is needed. The isothermal fatigue at extended cold temperature during moon night came to be more concerned other than that during moon daytime since some packaging materials come to be brittle, especially, intermetallics (IMCs) at joining interfaces played a critical role in cold temperature fatigue and accelerated the fatigue failure.

Intermetallics can strengthen solder joint bond but excessive intermetallics might cause brittle fracture at the bond line interfaces. The lower of the temperature, the more prone to fail of the intermetallics are. Moreover, the amount of intermetallics is not only depends on the initial metallization layers at the bonding interfaces but also affected by the operational temperatures. For example, the intermetallics at the interface of solder joint and die/substrate can grow gradually during the day time of the moon, which is because of the elevated temperature (125°C) for indium solder joint. Therefore, the growth of excessive intermetallics at daytime might accelerate and lead to the brittle failure at the solder joint interfaces when it's under the isothermal fatigued condition at moon night.

However, little data has been reported on fatigue properties of indium solder joint at cold temperatures and it has been studied in our work as the first time. Isothermal bending fatigue test was designed and conducted instead of thermal fatigue test to evaluate the

cold temperature fatigue performance of indium attach as well as identify the fatigue deformation mechanism at extended cold temperatures, which can exclude other deformation mechanisms such as creep at higher temperature above $0.5T_m$. The goal of this work is to establish

- 5) relationship of IMCs' growth with aging time upon various initial Au metallization thickness
- 6) relationship of IMCs thickness with solder joint reliability.
- 7) influence of subzero temperature, fatigue loading frequency on solder joint reliability at cold temperature upon different Au-In intermetallics.
- 8) develop fatigue life model based on the in depth understanding of the failure modes, mechanism and microstructures.

In this chapter, the thermal aging test was conducted at first to obtain the relationship of IMCs growth with aging time @ 125°C , which was used as the reference of IMCs thickness later in cold temperature fatigue test. Then the mechanical reliability was evaluated through low cyclic bending fatigue tests at -150°C and -55°C with respect to the effect of intermetallics amount and microstructure evolution under thermal aging. Amount of intermetallics in solder joint bond was controlled by (1) the intermetallics growth under different thermal aging time and (2) various initial Au metallization layer thickness (fixed indium thickness). And then we examine fracture surface of each specimen and discuss the effect of intermetallics on the low-temperature fatigue properties in indium in terms of how they correlate with the fatigue crack initiation sites, loading conditions and fatigue life.

Chapter 6 Summary, Contributions and Suggestions for Future Work

6.1 Summary

This dissertation presents a fundamental understanding of the underlying mechanisms that govern the degradation of indium attach used in SiGe electronic modules designed for operating on the surface of the Moon. An ordered, efficient and systematic methodology to evaluate the reliability of indium solder was established. It is basically divided into three categories.

Constitutive properties of indium do not only determine its deformation behavior but also form the basis of fatigue life evaluation, either under thermal fatigue or isothermal fatigue conditions. The cold temperature rate-temperature dependent (viscoplastic) constitutive properties of indium were investigated for the first time. The viscoplastic deformation properties of indium were measured by a series of compression load tests at four different ambient temperatures down to -150°C . Experimental data were implemented into the Anand constitutive model along with those high temperature data published by other researchers, and the Anand model was validated and calibrated for indium.

Thermal and mechanical fatigue behavior of indium attach was studied in a liquid nitrogen environment. Reliability assessment was conducted on the basis of accelerated thermal shock tests from -196°C to 125°C and isothermal fatigue tests at -150°C and -55°C . Thermal fatigue is believed to be the primary contributor to attach fatigue damage.

Accelerated thermal shock test with the same temperature extremes as those in real operational environment, was conducted to evaluate thermal fatigue life of indium attach. Meanwhile, simplified structures with different die sizes were also examined to achieve different strain levels and to construct thermal fatigue model. FEA modeling was performed to simulate the thermo-mechanical deformation behavior and to obtain the stress/strain distribution in the indium attach, which is most inclined to fatigue failure. Coffin-Manson empirical thermal fatigue model was calibrated for indium solder joint under thermal cycling related to operational conditions on the Moon's surface. Then the fatigue model was used as the guideline for future designs. FEA modeling of new designs was conducted to predict their fatigue life and the predicted life span also exceeded the design limits. Then the fatigue model was revalidated by the second and third generation of real package designs under thermal shock test. It was observed that fatigue crack propagated through indium attach and the dominant failure mechanism is attach fatigue failure.

Nevertheless, the growth of intermetallics at extreme high temperature during the lunar day can accelerate the interfacial brittle fracture in indium attach under mechanical fatigue at very cold temperature during the lunar night. Therefore, the reliability of the indium attach under low temperature isothermal fatigue condition becomes a concern. The dominant failure mechanisms was determined for this fatigue conditions, and a correlation were drawn between microstructure evolution and macroscopic attach fatigue behavior. Isothermal fatigue tests were conducted at various ambient temperatures, loading amplitudes, and frequencies to evaluate the low-temperature-isothermal-fatigue behavior of indium solder joints. The fatigue damage processes at cold temperatures,

namely, cyclic deformation, fatigue crack initiation, and fatigue crack growth were investigated. Dominant fatigue failure mechanisms in the attach at extended low temperatures, such as -150°C , were identified as the brittle fracture at interfacial intermetallics layer. The importance of the thickness of interfacial intermetallics and their evolution at bonding interfaces in determining overall fatigue life were determined. Their effect on macroscopic fatigue behavior of solder joints at cold temperatures was investigated and quantified. It was demonstrated that fatigue life is not monotonically dependent on intermetallics thickness, and a threshold region identified. The damage accumulation based strain energy fatigue model was validated, and extended to cryogenic temperatures based on in depth understandings of fatigue failure modes, and failure mechanisms by physics of failure (PoF) approach.

6.2 Major Contributions

This work provides the first comprehensive study of the reliability of indium solder joint under isothermal fatigue condition at extended cold temperatures, and thermal fatigue condition with extreme temperature cycles down to extreme cold temperature environment for space applications. The effect of cold temperature, material behavior, microstructure and intermetallics were studied in particular. The contributions of this work can be summarized as the following:

It is the first work to determine that interfacial brittle fracture at interfacial intermetallics layer is the dominant failure mode in indium attach under isothermal mechanical fatigue at extended cold temperatures (-150°C to -55°C). The crack path is through the interfacial layer instead of through pure indium layer in contrast to that under thermal fatigue

conditions. The influence of intermetallics under different cold temperatures, thermal aging conditions, strain amplitudes and loading frequencies on isothermal fatigue behavior at extended temperature was comprehensively studied.

This is the first study to examine the important effect of Au-In intermetallics on isothermal fatigue behavior of indium solder joint at extended cold temperature down to -150°C. Their effect on overall fatigue life was quantified for the first time. Insight into intrinsic strengthening, and degradation mechanisms was accomplished and correlated to the various initial amounts of intermetallics from reflow soldering process and their growth under thermal aging conditions. It proved that fatigue life is not monotonically dependent on intermetallics thickness. A threshold region was identified.

The current study also provides the first comprehensive investigation on the interrelationship of microstructure (intermetallics) evolution with macroscopic fatigue failure sites, failure modes, and corresponding fracture morphology in indium solder joints. Present work proposed that the intrinsic features of intermetallics can be represented by the interfacial fatigue crack propagation rate.

This thesis has further proved that indium deforms viscoplastically down to -150°C for the first time, which results in energy accumulation and stress/strain concentration at the attach/intermetallics interface, and is one of the critical contributors for crack propagation at cold temperature. Anand analytical constitutive model was validated for indium down to -150°C.

This thesis is the first study to extend thermal & mechanical fatigue model for indium attach to extreme cold temperatures (-150°C).

6.3 Suggestions for Future Work

- Correlation of mechanical fatigue experiments to actual shock and vibrational environment.
- A micro-mechanics based fatigue model that incorporates the effect of intermetallics.

Appendix A: ANSYS APDL Code of Thermomechanical Analysis

```

!
! Purpose:
! Nonlinear thermal and stress transient analysis of low temperature power module
! (Si/In/AlSi)
!
! Notation:
! 1. Temperature cycling: high & Low temperature dwell=60 sec; ramp up & down = 5 sec
! 2. Thermal cycling 398K ~ 78K
! 3. 2D model is utilized to reduce the computing time
!
! Records of revision:
!      Date              Programmer
!      =====          =====
!      04/18/06         Rui Wu
!
! #####

! ===== Build the Model =====

/PREP7
/TITLE, Nonlinear 2D thermal transient analysis of SiN-In-SiAl module
!

ET,1,PLANE55
ET,2,PLANE55

!----- Define material properties -----

MP,DENS,1,2330                ! Silicon: density 2330 Mg/m^3
MP,EX,1,179000*1E6           ! Young's Modulus 179 GPa
MP,KXX,1,148                 ! Thermal Conductivity 148 w/m.K
MP,CTEX,1,3.0*1E-6           ! CTE 3.0 ppm/c
MP,PRXY,1,0.22               ! Poisson's ratio

MPTEMP,1,75,140,205,270,335,400    ! Absolute temperature

! Indium: Young's Modulus
MPDATA,EX,2,1,19110*1E6,17000*1E6,14890*1E6,12780*1E6,10660*1E6,8550*1E6
! Thermal Conductivity
MPDATA,KXX,2,1,155.78,152.73,149.96,147.48,145.29,143.39
! CTE
MPDATA,CTEX,2,1,23.9*1E-6,26.9*1E-6,28.27*1E-6,30.46*1E-6,32.65*1E-6,34.83*1E-6
! Poisson's ratio
MPDATA,PRXY,2,1,0.3,0.3,0.3,0.3,0.3,0.3

TB,ANAN,2,,0
TBMODIF,1,1,100E6
TBMODIF,2,1,9369.74
TBMODIF,3,1,2.121E11
TBMODIF,4,1,48.31
TBMODIF,5,1,0.1135
TBMODIF,6,1,0
TBMODIF,7,1,100E6
TBMODIF,8,1,0
TBMODIF,9,1,1

! AlSi: Young's Modulus
MPDATA,EX,3,1,121400*1E6,121400*1E6,121400*1E6,121400*1E6,121400*1E6
! Thermal Conductivity
MPDATA,KXX,3,1,196.50,180.24,165.57,152.49,140.99,131.07
! CTE
MPDATA,CTEX,3,1,10.08*1E-6,8.03*1E-6,7.81*1E-6,8.67*1E-6,10.00*1E-6,11.35*1E-6
! Poisson's ratio
MPDATA,PRXY,3,1,0.25,0.25,0.25,0.25,0.25,0.25

!----- Define Parameters for model generation -----

```

```

*SET,nitride_width,1.524*1E-2          ! Dimensions of SiN layer
*SET,nitride_height,0.064*1E-2

*SET,In_height,100*1E-6                ! Dimensions of Indium layer
*SET,In_width,1.524*1E-2

*SET,alloy_width,2.54*1E-2             ! Dimensions of Si-Al alloy layer
*SET,alloy_height,0.10*1E-2

!----- Create the model -----

! Create Silicon Nitride layer
BLC4,0,0,nitride_width/1.414,(nitride_height+In_height+ALLOY_height),
! Define the fine mesh volume at the corner
BLC4,0,0,nitride_width/1.414*0.9,(nitride_height+In_height+ALLOY_height),
! Create In Layer
BLC4,0,0,In_width/1.414,(In_height+Alloy_height),
! Create Al-Si Alloy layer
BLC4,0,0,ALLOY_width/1.414,ALLOY_height,
! Define the fine mesh volume in SiAl layer at corner
BLC4,0,0,nitride_width/1.414*0.9,ALLOY_height,

AOVLAP,ALL                             ! Overlap the volume
AGLUE,ALL                               ! Glue all areas

NUMCMP,ALL                             ! Compress All
NUMMRG,ALL, , , ,LOW                   ! Merge All

!----- Assign the mesh properties -----

ASEL,S,LOC,Y,0,ALLOY_HEIGHT
AATT,3, ,1,0

ASEL,S,LOC,Y,ALLOY_HEIGHT,ALLOY_HEIGHT+IN_HEIGHT
AATT,2, ,2,0

ASEL,S,LOC,Y,ALLOY_HEIGHT+IN_HEIGHT,ALLOY_HEIGHT+IN_HEIGHT+NITRIDE_HEIGHT
AATT,1, ,1,0

ALLSEL,ALL

!----- meshing -----

LESIZE,ALL, , ,15, ,1, , ,1,          ! Overall element number per line

*SET,INDIUMNUM,5                        ! Set the element number along the thickness of indium layer
*SET,MESHNUM_INDIUM,25                  ! Set the element number along the width of indium layer

LESIZE,18, , ,INDIUMNUM, ,1, , ,1,    ! Specify the lines need refined meshing
LESIZE,19, , ,INDIUMNUM, ,1, , ,1,
LESIZE,20, , ,INDIUMNUM, ,1, , ,1,

LESIZE,5, , ,MESHNUM_INDIUM, ,1, , ,1, ! Specify the lines need refined meshing
LESIZE,8, , ,MESHNUM_INDIUM, ,1, , ,1,
LESIZE,17, , ,MESHNUM_INDIUM, ,1, , ,1,
LESIZE,15, , ,MESHNUM_INDIUM, ,1, , ,1,

AMESH,ALL                               ! Mesh all the areas
SAVE

! ===== Thermal Analysis =====

/SOLU
ANTYPE,TRANS                            ! Transient analysis type
TUNIF,398                                ! Starting temperature
TREF,398                                  ! Reference Temperature
TIMINT,OFF
TOFFST,0
NLGEOM,1

!-----Thermal Loads: -----

```

```

*SET,NCYCLE,4                ! Number of thermal cycling
*SET,T,130                   ! Period of temperature loading
*SET,DWELL,60
*SET,RAMPT,5
*SET,DELTAT,320/RAMPT

*DO,n,1,NCYCLE                ! Looping to write the LS file

TIME,(n-1)*T+DWELL           ! Low temperature 77K dwell 60 sec
AUTOTS,ON
KBC,1
NSUBST,100
D,ALL,TEMP,78
OUTRES,ALL,ALL
LSWRITE

TIME,(n-1)*T+DWELL+RAMPT     ! Ramp up to 398K in 5 sec
AUTOTS,ON
KBC,0
NSUBST,100
D,ALL,TEMP,398
OUTRES,ALL,ALL
LSWRITE

TIME,(n-1)*T+(DWELL+RAMPT+DWELL) ! Dwell at 398K for 60 sec
AUTOTS,ON
KBC,1
NSUBST,100
D,ALL,TEMP,398
OUTRES,ALL,ALL
LSWRITE

TIME,(n-1)*T+(DWELL+RAMPT+DWELL+RAMPT) ! Ramp down to 77K in 5 sec
AUTOTS,ON
KBC,0
NSUBST,100
D,ALL,TEMP,78
OUTRES,ALL,ALL
LSWRITE

*ENDDO

LSSOLVE,01,NCYCLE*4
SAVE
FINISH

! =====Structural Analysis for creep & elastic effects =====

/PREP7

ET,1,PLANE42
ET,2,VISCO108

/SOLU
ANTYPE,0                ! Static analysis
TREF,398                ! Reference temperature
TIMINT,OFF
TOFFST,0

LSEL,S,LOC,X,0          ! Select the symmetric areas x=0
DL,ALL,,SYMM           ! Applied displacement constraints DOF=0 to select areas
ALLSEL,ALL             ! Select all

*DO,n,1,NCYCLE

Time,(n-1)*T+DWELL      ! Read the temperature loading profile from thermal analysis
LDREAD,TEMP,(n-1)*4+1,,,,,'file','rth',' ' NLGEOM,ON        ! Large deflection
NSUBST,,100
DELTIM,3,1E-3,10,1     ! Time step
KBC,1
AUTOTS,ON              ! Auto stepping on
OUTRES,ALL,ALL
LSWRITE

```

```
TIME,(n-1)*T+DWELL+RAMPT           ! Ramp up to 398K in 5 sec
LDREAD,TEMP,(n-1)*4+2,,,, 'file','rth','
AUTOTS,ON
KBC,0
NSUBST,100
OUTRES,ALL,ALL
LSWRITE
```

```
TIME,(n-1)*T+(DWELL+RAMPT+DWELL)   ! Dwell at 398K for 60 sec
LDREAD,TEMP,(n-1)*4+3,,,, 'file','rth','
AUTOTS,ON
KBC,1
NSUBST,100
OUTRES,ALL,ALL
LSWRITE
```

```
TIME,(n-1)*T+(DWELL+RAMPT+DWELL+RAMPT) ! Ramp down to 77K in 5 sec
LDREAD,TEMP,(n-1)*4+4,,,, 'file','rth','
AUTOTS,ON
KBC,0
NSUBST,100
OUTRES,ALL,ALL
LSWRITE
```

```
*ENDDO
```

```
LSSOLVE,NCYCLE*4+1,NCYCLE*4+NCYCLE*4
```

```
SAVE
FINISH
```

Appendix B: ANSYS APDL Code of 3D Nonlinear Bending Fatigue – Global Modeling

```

!
! Purpose:
!   Nonlinear structural analysis of low temperature 3 Point cyclic bending fatigue of component on substrate
!
! Notation:
!   1. Nonlinear viscoplastic material properties of indium was included
!   2. Ambient temperature -150C
!   3. 3D model
!
! Records of revision:
!   Date                Programmer
!   =====            =====
!   03/10/08           Rui Wu Chang
!
! #####
! #####

! ===== Build the Model =====

/PREP7
/TITLE, Nonlinear 3D structural analysis 3 point bending
!

!----- Define material properties -----

MP,DENS,1,8933                ! Copper: density 8933 Mg/m^3
MP,EX,1,137500*1E6           ! Young's Modulus 137.5 GPa @=123K
MP,KXX,1,413                 ! Thermal Conductivity 413 w/m.K
MP,CTEX,1,12.04*1E-6         ! CTE 12.04 ppm/c
MP,PRXY,1,0.364              ! Poisson's ratio

MPTEMP,1,75,140,205,270,335,400      ! Absolute
temperature

MPDATA,EX,2,1,19110*1E6,17000*1E6,14890*1E6,12780*1E6,10660*1E6,8550*1E6      ! Indium: Young's
Modulus
MPDATA,KXX,2,1,155.78,152.73,149.96,147.48,145.29,143.39                       ! Thermal
Conductivity
MPDATA,CTEX,2,1,23.9*1E-6,26.9*1E-6,28.27*1E-6,30.46*1E-6,32.65*1E-6,34.83*1E-6   ! CTE
MPDATA,PRXY,2,1,0.3,0.3,0.3,0.3,0.3,0.3                                         ! Poisson's ratio

TB,ANAN,2,,0
TBMODIF,1,1,30E6
TBMODIF,2,1,9369.74
TBMODIF,3,1,1.65E8
TBMODIF,4,1,47.31
TBMODIF,5,1,0.2745
TBMODIF,6,1,0
TBMODIF,7,1,30E6
TBMODIF,8,1,0
TBMODIF,9,1,1

!----- Define parameters for model generation -----

*SET,coppersubstrate_width,4.5*1E-2      ! Dimensions of copper substrate strip
*SET,coppercompo_width,0.6*1E-2         ! Dimensions of copper component strip
*SET,copper_height,0.055*1E-2          ! Thickness of copper strips
*SET,copper_depth,0.6*1E-2             ! Width of copper strips

*SET,In_width,0.6*1E-2                 ! Dimensions of indium foil
*SET,In_height,100*1E-6                ! Thickness of indium foil
*SET,In_depth,0.6*1E-2                 ! Width of indium foil

!----- Create geometric model -----

! Create copper substrate layer
BLC4,0,In_height+copper_height,coppersubstrate_width/2,copper_height,copper_depth/2

```

```

BLC4,0,In_height+copper_height,coppersubstrate_width/2-0.005,copper_height,copper_depth/2

! Create In Layer
BLC4,0,copper_height,In_width/2,In_height+copper_height,In_depth/2

! Create copper component layer
BLC4,0,0,coppercompo_width/2,copper_height,copper_depth/2

! Define the fine mesh volume
BLC4,0,0,coppercompo_width/2*0.85,2*(copper_height)+In_height,copper_depth/2

VOVLAP,ALL ! Overlap the volumes
VGLUE,ALL ! Glue all volumes

NUMCMP,ALL ! Compress All
NUMMRG,ALL, , , ,LOW ! Merge All

!----- Assign the mesh properties -----

ET,1,SOLID45 ! Define elements
ET,2,VISCO107

VSEL,S,LOC,Y,0,COPPER_HEIGHT ! Assign copper properties
VATT,1, ,1,0

VSEL,S,LOC,Y,COPPER_HEIGHT,COPPER_HEIGHT+IN_HEIGHT
VATT,2, ,2,0

VSEL,S,LOC,Y,COPPER_HEIGHT+IN_HEIGHT,COPPER_HEIGHT+IN_HEIGHT+COPPER_HEIGHT
VATT,1, ,1,0

ALLSEL,ALL ! Select all

!----- meshing -----

*SET,IN_LAYER,5 ! Define mesh layers in indium solder
*SET,CU_LAYER,8 ! Assign mesh layers in copper component and substrate
*SET,CU_length,45 ! Assign mesh numbers in copper substrate

LSEL,S,LENGTH,,COPPERCOMPO_WIDTH/2*0.85,COPPERCOMPO_WIDTH/2*0.85
LESIZE,ALL, , ,40, ,1, , ,1,

LSEL,S,LENGTH,,COPPERCOMPO_WIDTH/2*0.15,COPPERCOMPO_WIDTH/2*0.15
LESIZE,ALL, , ,20, ,1, , ,1,

LSEL,S,LENGTH,,COPPERSUBSTRATE_WIDTH/2-COPPERCOMPO_WIDTH/2-0.005,COPPERSUBSTRATE_WIDTH/2-
COPPERCOMPO_WIDTH/2
LESIZE,ALL, , ,50, ,1, , ,1,

LSEL,S,LENGTH,,COPPER_HEIGHT,COPPER_HEIGHT
LESIZE,ALL, , ,6, ,1, , ,1,

LSEL,S,LENGTH,,IN_HEIGHT,IN_HEIGHT
LESIZE,ALL, , ,8, ,1, , ,1,

LSEL,S,LENGTH,,AU_HEIGHT,AU_HEIGHT
LESIZE,ALL, , ,1, ,1, , ,1,

VMESH,ALL ! Mesh all volumes
SAVE ! Save

! =====Structural Analysis =====

/SOLU
ANTYPE,0 ! Static analysis
TREF,398 ! Reference temperature
TUNIF,123 ! Assign test ambient temperature
TIMINT,OFF ! Turn off transient effect
TOFFST,0 ! Specifies the temperature offset from absolute zero to zero

ASEL,S,LOC,X,0 ! Select the symmetric areas x=0
DA,ALL,SYMM,, ! Applied displacement constraints DOF=0 to select areas
ASEL,S,LOC,Z,0 ! Select the symmetric areas x=0

```

```

DA,ALL,SYMM,,
ALLSEL,ALL

NSEL,S,LOC,X,0
NSEL,R,LOC,Y,COPPER_HEIGHT*2+IN_HEIGHT
D,ALL,UY,0
ALLSEL,ALL

*SET,DISPLACEMENT,0.00015
*SET,F,0.3
*SET,T,1/f
*SET,NCYCLE,10

*DO,n,1,NCYCLE

Time,(n-1)*T+T/2

NSEL,S,LOC,Y,copper_height+In_height
NSEL,R,LOC,X,coppersubstrate_width/2-0.005
D,ALL,UY,DISPLACEMENT
NSEL,ALL

SOLCONTROL,ON
NLGEOM,ON
AUTOTS,ON
NSUBST,,3000
DELTIM,0.01,0.1E-7,10,1
KBC,0
OUTRES,ALL,ALL
LSWRITE

TIME,(n-1)*T+T

NSEL,S,LOC,Y,copper_height+In_height
NSEL,R,LOC,X,coppersubstrate_width/2-0.005
D,ALL,UY,0
NSEL,ALL

SOLCONTROL,ON
NLGEOM,ON
AUTOTS,ON
NSUBST,3000
DELTIM,0.01,0.1E-7,10,1
KBC,0
OUTRES,ALL,ALL
LSWRITE

*ENDDO

```

! Applied displacement constraints DOF=0 to select areas
! Select all

! Select center line location in x axis
! Select center line fixed nodes on copper substrate
! Assign fixed boundary condition at center line
! Select all

! Define applied displacement at substrate edge
! Define loading frequency
! Calculate loading period
! Define cyclic loading cycle

! Cyclic load profile writing starts

! Select applied displacement position

! Apply displacement
! Select all

! Solution control on
! Large deflection
! Auto stepping on
! Define sub step
! Time step
! Ramp up
! Record all results
! Write LS file

References

1. Cressler, J.D., "On the Potential of SiGe HBTs for Extreme Environment Electronics", Proceedings of IEEE, Vol.93, NO.9, Sep. 2005.
2. Kirschman, R. K., Sokolowski, W.M. and Kolawa, E.A., "Die Attachment for -120C to +20C Thermal Cycling of Microelectronics for Future Mars Rovers – An Overview", J. of Electronic Packaging, ASME, Vol. 123, June, 2001.
3. Glazer, J. "Metallurgy of Low Temperature Pb – Free Solders for Electronic Assembly", Inter. Materials Reviews, Vol.40, No.2, 1995.
4. Hermida, E'lida B., Melo, Diego G., Julio C. Aguiar, Lo'pez, Daniel E., "Temperature Dependence of the Viscoelastic Response of In, Sn and In–Sn Alloys", J. of Alloys and Compounds Vol.310, pp 91–96, 2000.
5. Kim, S. and Ledbetter, H.M., "Low Temperature Elastic Coefficients of Polycrystalline Indium", Material science and Engineering A252, 1998, pp139-143.
6. Zinov'ev, Vladislav E., "Thermophysical properties of Metals at High Temperature", Nova Sci.Pub,Inc.
7. Swenson, C.A., "Properties of Indium and Titanium at Low Temperatures", Physical Review, Vol.100, No.6, December, 1955.
8. Weertman, J., "Creep of Indium, Lead, and Some of Their Alloys with Various Metals", Transactions of the metallurgical society of AIME, Vol.218, April, 1960.
9. Lucas, B.N. and Oliver, W.C., "Indentation Power Law Creep of High-Purity Indium", Metallurgical and materials Transactions A, Vol.30A, March, 1999, pp 601-610.
10. Reed, R.P., McCowan, C.N., and Walsh, R.P., "Tensile Strength and Ductility of Indium", Materials Sci. and Eng. A, Vol. 102, pp 227-236, 1988.
11. Plotner, M., Donat, B. and Benke, A., "Deformation Properties of Indium-based Solders at 294 and 77K", Cryogenics, Vol.31, March, 1991.
12. M.J. Hoffmann, G. Petzow, 'Tailored microstructures of silicon nitride ceramics', Pure & appl. Chem., Vol. 66, No.9, pp. 365-378, 1994.
13. Osprey Controlled Expansion Alloys, SANDVIK.
14. J.mater.Res, Vol.12, No.1, Jan1997, pp.59
15. Mechanics of Materials, 23(1996), pp.314
16. Yoo, M.H., Sass, S.L., Fu, C. L. and etc., "Deformation and Fracture of Intermetallics", Acta metal. Mater. Vol. 41, No. 4, pp. 987-1002, 1993.
17. Kassner, M.E. and Perez-Prado, M.T., "Fundamentals of Creep in Metals and Alloys", ELSEVIER, 2004.
18. Darveaux, R. and Turlik, I., "Shear Deformation of Indium Solder Joints", IEEE Trans. on Comp., Hybr., and Nano. Tech., Vol.13, NO.6, Dec. 1990.

19. Darveaux, R. and Turlik, I., "Cyclic Deformation and Mechanical Fatigue of Indium Solder Joints", Procee. of the 7th Electronic Materials and Processing Congress, Cambridge, Mass, USA, pp 24-27, Aug. 1992.
20. Shetty, S. and Reinikainen, T., "Three and Four-Point Bend Testing for Electronic Packages", J. of Electronic Packaging, Trans. of ASME, Vol. 125, Dec., 2003.
21. Shetty, S., Lehtinen, V., Dasgupta, A. and Halkola, V., etc, "Fatigue of Chip Scale Package Interconnects Due to Cyclic Bending", J. of Electronic Packaging, Trans. of ASME, Vol. 123, Sept., 2001.
22. Leicht, L. and Skipor, A., "Mechanical Cycling Fatigue of PBGA Package Interconnects", Microelectronics Reliability 40 (2000) 1129-1133.
23. Zhao, J., Mutoh, Y., Miyashita, Y. and Wang, L., "Fatigue Crack Growth Behavior of Sn-Pb and Sn-based lead-free Solders", Engineering Fracture Mechanics 70, 2003, 2187-2197.
24. Shang, J.K., Zheng, Q.L., Zhang, L. and Zhu, Q.S, "Mechanical Fatigue of Sn-rich and Pb-free Solder Alloys", J. Mater Sci: Mater Electron (2007) Vol 18: 211-227.
25. Pidaparti, R.M.V. and Song, X., "Fatigue Crack Propagation Life Analysis of Solder Joints under Thermal Cyclic Loading", Theoretical and Applied Fracture Mechanics 24 (1996) 157-164.
26. Tu, P.L., Chan, Y.C., Hung, K.C. and Lai, K.L., "Comparative Study of Micro-BGA Reliability Under Bending Stress", IEEE Trans. on Adv. Packaging, Vol.23, No.4, Nov. 2000.
27. Wu, J.D., Ho, S.H., Huang, C.Y., and Liao, C.C., etc., "Board Level Reliability of a Stacked CSP Subjected to Cyclic Bending", Microelectronics Reliability 42 (2002) 407-416.
28. Sheen, M.T., Chang, C.M., Teng, H.C. and Hsieh, K.C., etc., "The Influence of Thermal Aging on Joint Strength and Fracture surface of PB/Sn and Au/Sn Solders in Laser Diode Packages", J. of Electronic Materials, Vol.31, No.8, 2002.
29. Yoon, J.W. and Jung, S.B., "High Temperature Reliability and Interfacial Reaction of Eutectic Sn-0.7Cu/Ni Solder Joints during Isothermal Aging", Microelectronics Reliability 46 (2006) 905-914.
30. R. Chadwick, "The Influence of Surface Alloying on the Strength of Soft Soldered Joints," J. Inst. Metals 62 (1938) 277.
31. H. Swanger and A.R. Maupin, "Structural Changes in the Bonding Layer of Soft-Soldered Joints in Copper Pipe Line on Long-Continued Heating," Research Paper 1465, J.Res. National Bureau of Standards 28 (1942) 479.
32. Metals Handbook 9th Ed., Vol. 6: Welding, Brazing, and Soldering, publ. by Amer. Soc. for Metals, Metals Park, Ohio (1983).
33. Sauthoff, G., Intermetallics, VCH (1995).

34. P.E. Davis, M.E. Warwick, C. Chem, P.J. Kay, C. Eng, and S.J. Muckett, "Intermetallic Compound Growth and Solderability," *Plating and Surface Finishing* 70, (1983) 49.
35. M.E. Warwick and S.J. Muckett, "Observations on the Growth and Impact of Intermetallic Compounds on Tin-Coated Substrates," *Circuit World* 9 #4 (1983) 5.
36. J.O.G. Parent, D.D.L. Chung, and I.M. Bernstein, "Effects of Intermetallic Formation at the Interface between Copper and Lead-Tin Solder," *J. Mat. Sci* 23 (1988) 2564.
37. X. Deng et al., "Young's Modulus of (Cu, Ag)-Sn Intermetallics Measured by Nanoindentation", *Mater. Sci.Eng. A* 364, pp. 240-243, 2004.
38. Cheng, K. S., Wigbert, J. S., "Thermal expansion of AuIn₂", *Scripta Materialia* 53 (2005) 1153–1157.
39. Hiscocks, S.E.R. and Hume-Rothery, W., "The Equilibrium Diagram of the System Gold-Indium", *Proc. of Royal Sci. of London, Ser.A, Math. & Phy. Sci.*, Vol.282, No.1390, pp318-330.
40. Millared, M. and Pieraggi, B., "Reaction/diffusion in the Au-In System", *Solid State Ionics* Vol.63-65, pp575-580,1993, North-Holland.
41. Shieu, F.S., Chen, C.F., Sheen, J.G., and Chang, Z.C., "Intermetallic Phase Formation and Shear Strength of a Au-In Microjoint", *Thin Solid Films*, Vol.346, pp 125-129, 1999.
42. Lee, C.C., Wang, C.Y. and Matijasevic G., "Au-In Bonding Below the Eutectic Temperature", *IEEE Trans. on Comp, Hyb. and Manu. Tech*, Vol.16, No.3, May, 1993.
43. Chang, Z.C., Lu, F.H. and Shieu, F.S., "Characterization of the Microstructure and Phase Formation in the Au-In System Using Transmission Electron Microscopy", *Materials Chemistry and Physics* 70 (2001), pp 137-143.
44. Shin, K., Cho, W.G. and Kim, Y.H., "Interfacial Microstructure and Intermetallics Developed in the Interface between In Solders and Au/Ni/Ti Thin Films during Reflow Process", *J. of Electronic Materials*, Vol. 32, No.6, 2003.
45. Lee, H.T., Chen, M.H., Jao, H.M. and Liao, T.L., "Influence of Interfacial Intermetallic Compound on Fracture Behavior of Solder Joints", *Materials and Engineering* A358 (2003), 134-141.
46. Wei, T.C., and Daud, A.R., "Mechanical and Electrical Properties of Au-Al and Cu-Al Intermetallics Layer at Wire Bonding Interface", *J. of Electronic Packaging*, ASME, Vol.125. Dec. 2003.
47. J. H. Lau, *Solder Joint Reliability*. New York: Van Nostrand Reinhold, 1991, pp. 406–449.
48. D. Solomon, "Isothermal fatigue of LCC/PWB interconnections," *J. Electron. Packag.*, vol. 114, pp. 161–168, June 1992.

49. Y. C. Chan, D. J. Xie, J. K. L. Lai, and I. K. Hui, "Application of direct strain measurement to fatigue studies in surface solder joints," *IEEE Trans. Comp. Packag., Manufact. Technol.*, vol. 18, pp. 715–719, 1995.
50. Chan, Y.C., Tu. P.L., So, A.C.K. and Lai, J.K.L., "Effect of Intermetallic Compounds on the Shear Fatigue of Cu/63Sn-37Pb Solder Joints", *IEEE Trans. on Components, Packaging, and Manu. Tech. – Part B*, Vol. 20, No.4, Nov. 1997.
51. Liu, Y.M. and Chuang, T.H., "Interfacial Reactions between Liquid Indium and Au-Deposited Substrates", *J. of Electronic Materials*, Vol.29, No.4, 2000.
52. Saw, C.K. and Siekhaus, J.K, "Thermal expansion of AuIn₂", *Scripta Material A*, Vol. 53, Issue 10, November 2005, Pages 1153-1157.
53. Darveaux, R. and Murty, K.L., "Effect of Deformation Behavior on Solder Joint Reliability Prediction", *Microstructures and Mechanical Properties of Aging Material*, The Minerals, Metals & Material Society, 1993.
54. Langdon, T.G., "Deformation at High Temperatures", *Strength of Metals and Alloys: Proc. 6th Int. Conf.*, Aug. 1982, pp.1105-1120.
55. Darveaux, R. and Banerji, K., "Constitutive Relations for Tin-Based Solder Joints", *IEEE Trans. on Comp., Hybr., and Manu. Tech.*, Vol.15, NO.6, Dec. 1992.
56. Frenkel, R.E., Sherby, O.D. and Dorn, J.E., "Acta Metall.", Vol.3, 1955, pp470.
57. Frost and Ashby, "Deformation Mechanism Maps.", New York: Pergamon, 1982.
58. Anand, L. "Constitutive Equations for Hot-Working of Metals", *Inter. Jour. of Plasticity*, Vol.1, pp.213-231, 1985.
59. Brown, S.B., Kim, K.H., and Anand, L., "An internal Variable Constitutive Model for Hot Working of Metals", *Int. J. Plast.*, Vol.6, pp.95-130, 1989.
60. Cheng, Z.N., Wang, G.Z., Becker, K., "Applying Anand Model to Represent the Viscoplastic Deformation Behavior of Solder Alloys", *J. of Elect. Packaging*, ASME, Vol.123, Sep. 2001.
61. Wilde, J., Becker, K., Thoben, M. and Blum, W., "Rate Dependent Constitutive Relations Based on Anand Model for 92.5Pb5Sn2.5Ag Solder", *IEEE Trans. on Advanced Packaging*, Vol.23, No.3, Aug.2000.
62. ANSYS, Inc. Theory Reference 9.0
63. Chen, W.T. and Nelson, C.W., "Thermal Stress in Bonded Joints", *IBM J. RES. DEVELOP.* VOL. 23 NO. 2 MARCH 1979.
64. Suhir, E. "Analysis of interfacial thermal stresses in a trimaterial assembly", *J. of Applied Physics*, VOL. 89, NUM. 71, APRIL 2001.
65. Darveaux, R., Hwang, L.T., and Reisman, A., "Thermal/Stress Analysis of a Multichip Package Design", Vol. 55, pp 668-671, IEEE, 1989.
66. Aoki, S., Imanaka, Y., Yokouchi, K., and Kamehara, N., "Multilayer Ceramic Substrate for HEMT Packaging", *Int. J. Microcircuits Electron. Packag.*, 15, No.3, pp 160-170, 1992.

67. Reed, R.P., and Walsh, R.P., "Creep of Indium at Low Temperatures", *Advances in Cryogenic Engineering Materials*, 38A, pp117-126, 1992.
68. Lee, W.W., Nguyen, L.T. and Selvaduray, G.S., "Solder Joint Fatigue Models: Review and Applicability to Chip Scale Packages", *Microelectronics Reliability*, Vol.40, pp 231-244, 2000.
69. Massiot, G. and Munier, C., "A Review of Creep Fatigue Failure Models in Solder Material – Simplified Use of a Continuous Damage Mechanical Approach", 5th. Int. Conf. on Thermal and Mechanical Simulation and Experiments in Micro-electronics and Micro-Systems, EuroSim2004.
70. Coffin, L.F., "A Study of the Effect of Cyclic Thermal Stresses on a Ductile Metal", *Transactions of the ASME*, Vol. 76, pp. 931-950, 1954.
71. Manson, S. S., "Fatigue: A complex subject-Some. simple approximations", *Experimental Mechanics*, Vol. 5, No. 7, pp. 193-226, 1965.
72. Syed, A. "Accumulated creep strain and energy density based thermal fatigue life prediction models for SnAgCu solder joints". in 54th Electronic Components and Technology Conference. 2004. Las Vegas, NV, USA: IEEE.
73. Dasgupta, A., et al., "Solder creep-fatigue analysis by an energy-partitioning approach". *ASME Journal of Electronic Packaging*, 1992. 114(2): p. 152.
74. Darveaux, R., "Solder Joint Fatigue Life Model," in *Design and Reliability of Solders and Solder Interconnections*, The Minerals, Metals and Materials Society, pp 213-218, 1997.
75. Darveaux, R., "Effect of simulation methodology on solder joint crack growth correlation and fatigue life prediction". *ASME Journal of Electronic Packaging*, 2002. 124(3): p. 147
76. Darveaux, R., Banerji, K., Mawer, A. And Dody, G., "Reliability of Plastic Ball Grid Array Assembly", *Ball Grid Array Tech*, J. Lau Editor, McGraw-Hill, Inc., New York, 1995.
77. Uegai, Y., Kawazu, A., Wu, Q. and Matsushima, H., etc., "New Thermal Fatigue Life Prediction Method for BGA/FBGA Solder Joints with Basic Crack Propagation Study", ECTC, 2002, IEEE.
78. Sangalli, N. and Barker, D.B., "Solder Joint Crack Propagation in Plastic and Ceramic Packaged Diodes Mounted on Insulated Metal Substrate", ECTC, 2001, IEEE.
79. Vandavelde, B., et al. "Solder parameter sensitivity for CSP life-time prediction using simulation-based optimization method". 2001. Orlando, FL, USA: IEEE.
80. Rosenberg, G. "Effect of Grain Size on the Fatigue Crack Growth in Steels at Temperature 295 and 77K", *ISIJ international*, Vol.43, No.10, pp 1652-1652, 2003.
81. Reed, R.E., "Physical Metallurgy Principles", PWS Engineering, Boston, Massachusetts.
82. Ankem, Greene, C.A. and Aiyangar, A.K., "Advances in Twinning", TMS (1999).

83. Kalidindi, S.R., "On Deformation Twinning in Polycrystalline FCC Metals", Advances in Twinning, Proce. of Inter. symposium by the Minerals, Metals & Materials Society
84. Song, X.P., Sun, Q.Y. and Gu, H.C. "Low Cycle Fatigue Behavior of Commercial Purity Titanium at Cryogenic Temperature", Proce. of 8th Int. Conf. on Mechanical Behavior of Materials, ICM8, Victoria, B.C., Canada, 1999.
85. Kim, D.G., Kim, J.W. and Jung, S.B., "Evaluation of Solder Joint reliability in Flip Chip Package under Thermal Shock Test", Thin Solid Films, 504 (2006), pp426-430.
86. Pang, J.H.L. and Low, T.H., "Modeling Thermal Cycling and Thermal Shock Tests for PCOB", IEEE, Inter. Society Conference on Thermal Phenomena, 2002.
87. JagarKal, S.G., Hossain, M.M. and Agonafer, D., "Design Optimization and Reliability of PWB Level Electronic Package", IEEE, Inter. Society Conference on Thermal Phenomena, 2004.
88. User Manual of RSAIII, TA Instruments.
89. Snedecor, George W. and Cochran, William G. (1989), Statistical Methods, Eighth Edition, Iowa State University Press.
90. David F. Groebner, etc. (2001), Business Statistics, 4th ed. Prentice-Hall, Inc.